UNIVERSITY OF CALIFORNIA, MERCED

Development and Characterization of Liquid Crystal-Gold Nanoparticle Hybrid Materials for Optical Applications

A dissertation submitted in partial satisfaction of the
requirements for the degree of
Doctor of Philosophy

in

Physics

by

Makiko T. Quint

Committee in charge:

Professor Jay E. Sharping, Chair
Professor Jennifer Lu
Professor Linda S. Hirst
Professor Sayantani Ghosh

2017

The dissertation of Makiko T. Quint, titled Development and Characterization of Liquid Crystal-Gold Nanoparticle Hybrid Materials for Optical Applications, is approved, and it is acceptable in quality and form for publication on microfilm and electronically:

_____ Date _____

Professor Jennifer Lu

_____ Date _____

Professor Linda S. Hirst

_____ Date _____

Professor Sayantani Ghosh

_____ Date _____

Professor Jay E. Sharping, Chair

University of California, Merced

2017

This work is dedicated to:

- my beloved husband David A. Quint, who's unconditional love, encouragement, and support made it possible for me to go through all the difficulties I came across during my Ph.D. study.
- my parents, Hideo and Mariko Tsukamoto, whose good examples have taught me to work hard for the things that I aspire to achieve. All of their years of unconditional love, encouragements, patience, and sacrifice will remain my inspiration throughout my life.
- my sister and brother-in-law, Takako and Akira Sasaki, who always supported me in my efforts and dreams.
- my relatives, to the memory of my uncles and aunts, who were survivors and victims of one of the world's worst Tsunami and nuclear disasters in 2011. I value all of their support through their words and appreciate their confidence. Their infallible love has always been my strength.

Contents

List of Abbreviations

NPs	Nanoparticles
AuNPs	Gold nanoparticles
QDs	Quantum dots
CdSe	Cadmium selenide
ZnS	Zinc sulfide
LC	Liquid crystal
NLC	Nematic liquid crystal
5CB	4-cyano-4'-pentylbiphenyl
NAMs	Nano-assembled microcapsules (micro-shells)
ITO	Indium tin oxide
PVA	Polyvinyl alcohol
CTAB	Cetyltrimethylammonium bromide
EDTA	Ethylenediaminetetraacetic acid
DMEM	Dulbecco's Modified Eagle's Medium
LB media	Luria-Bertani media
GFP	Green fluorescent protein
DNA	Deoxyribonucleic acid
C2C12	An immortalized mouse myoblast cell line
E. coli	Escherichia coli
LSPR	Localized surface plasmon resonance
SPPs	Surface plasmon polaritons
SAXS	Small-angle X-ray scattering
NIR	Near-infrared
UV-Vis	Ultraviolet-visible
OD	Optical density
POM	Polarized optical microscopy
SEM	Scanning electron microscopy
FESEM	Field emission scanning electron microscopy
DSC	Differential scanning calorimetry
AFM	Atomic force microscopy
NMR	Nuclear magnetic resonance
ATR-FTIR	Attenuated total reflectance–Fourier transform infrared

ESI	Electrospray ionization
HRMS	High resolution mass spectrometry
CCD	Charge-coupled device
EMCCD	Electron multiplying charge-coupled device
ANSI	American national standards institute
DDA	Discrete dipole approximation
DDSCAT	Discrete dipole scattering
FDTD	Finite difference time domain
vol%	Volume percent
wt%	Weight percent
rpm	Revolutions per minute
mmol	Millimole
nmol	Nanomole
eV	Electronvolt
keV	Kiloelectronvolt
mg	Milligram
ml	Milliliter
m	Meter
nm	Nanometer
μm	Micrometer
Hz	Hertz
MHz	Megahertz
W	Watt
V	Volt
s	Second
$CDCl_3$	Deuterated chloroform
^{13}C	Carbon-13
^{1}H	Hydrogen-1
DCM	Dichloromethane
TEA	Triethylamine
DMAP	4-dimethylaminopyridine
EDCl	1-ethyl-3-(3-dimethyl-aminopropyl) carbodiimide
HCl	Hydrochloric acid
CO	Carbon monoxide
NO	Nitrogen monoxide
H_2SO_4	Sulphuric acid
K_2CO_3	Potassium carbonate
$C_8H_{17}Br$	1-Bromooctane
KI	Potassium iodide
NaOH	Sodium hydroxide
$SOCl_3$	Thionyl chloride
CH_3SO_2Cl	Methanesulfonyl chloride
MeOH	Methanol
PHMe	Toluene
KOt-Bu	Potassium tert-butoxide

List of Symbols

α	Polarizability
ζ	Shape factor
ε_0	Permittivity of free space
V_P	Volume of a gold nanoparticle
$\varepsilon(\lambda)$	Dielectric function of the gold nanoparticle
ε_m	Dielectric constant of the surrounding medium
κ	Light absorption coefficient
ω	Angular frequency of the electromagnetic radiation
$\varepsilon_1(\omega)$	Real part of the gold nanoparticle dielectric function
$\varepsilon_2(\omega)$	Imaginary part of the gold nanoparticle dielectric function
P	Induced dipole moment
E_0	Applied field
E_d	Electric field produced by the dipole inside a gold particle
σ_{ext}	Cross-sections for extinction
σ_{scat}	Cross-sections for scattering
σ_{abs}	Cross-sections for absorption
L	Multipole order
a_L	Mie-coefficient
b_L	Mie-coefficient
k	Wave vector of the incident electromagnetic wave
c	Speed of light in vacuum
n	Refractive index
$T(\overrightarrow{r}, t)$	Temperature at the particular point
$\overrightarrow{r}$	Coordinate at specific time
t	Time
$\rho(\overrightarrow{r})$	Density
$C_h(\overrightarrow{r})$	Heat capacity
$\kappa(\overrightarrow{r})$	Thermal conductivity of the surrounding material
$Q(\overrightarrow{r}, t)$	Heat source produced by the gold nanoparticle

Q	Heat with constant thermal energy
k_0	Thermal conductivity of the surrounding medium
r	Distance to the nanoparticle surface
I_0	Intensity of the incident electromagnetic wave
E_g	The lowest excited energy state
$E_{g,bulk}$	Bulk band gap
$\hbar$	Planck's constant
R_P	Particle radius
m_e^*	Effective mass of an electron
m_h^*	Effective mass of a hole
m_o	Free electron mass
e	Charge on an electron
k_{et}	Electron transfer rate constant
k_B	Boltzmann constant
T_a	Absolute temperature
$\triangle G^0$	Free energy change between the initial and the final state
M_{12}	Electronic coupling matrix element between initial and final states on resonance
$\triangle E$	Energy of the electron transfer
Λ	Total reorganization energy
Λ_i	Internal vibrations
Λ_o	Changes in the configuration of the dielectric matrix surrounding the nanocrystals
a_1	Radius of a nanocrystal
a_2	Radius of a nanocrystal
d	Distance of separation between two nanocrystals
ε_{OP}	Optical dielectric constants of the surrounding insulating matrix
ε_S	Optical and static dielectric constants of the surrounding insulating matrix
T	Temperature
T_K	Disordering temperature of the crystalline state
T_N	Nematic transition temperature
T_I	Isotropic transition temperature
S	Degree of orientational order
θ	Angle
$\mathbf{n}$	Nematic director
F_S	Free energies for splay deformation
F_T	Free energies for twist deformation

F_B	Free energies for bend deformation
$\hat{\mathbf{n}}$	A unit vector of nematic director
K	Frank elastic constants
K_1	Frank elastic constants relate to the splay deformation
K_2	Frank elastic constants relate to the twist deformation
K_3	Frank elastic constants relate to the bend deformation
ϕ	Polar angle
ϵ	Dielectric anisotropy of LC
$\epsilon_{\parallel}$	Dielectric permittivities in the parallel direction
$\epsilon_{\perp}$	Dielectric permittivities in the perpendicular direction
$\overrightarrow{E}$	Electric field
$\overrightarrow{P}$	Induced polarization
$\overrightarrow{\chi}_e$	Electric susceptibility
$\varepsilon_{\parallel}$	Dielectric constant in the parallel direction related to the susceptibilities
$\varepsilon_{\perp}$	Dielectric constant in the perpendicular direction related to the susceptibilities
$F_{electric}$	Electric energy of the LC per unit volume
E_{th}	Threshold field
$E_{S,th}$	Threshold field for LC reorientation for splay
$E_{T,th}$	Threshold field for LC reorientation for twist
$E_{B,th}$	Threshold field for LC reorientation for bend
d_T	LC layer of thickness
$n_{\parallel}$	Refractive indices along the optical axis, and perpendicular to it $n_{\perp}$
$n_{\parallel}$	Refractive indices located at perpendicular to the optical axis
n_o	Ordinary refractive indices
n_e	Extraordinary refractive indices
$\triangle n$	Optical birefringence
I	Light intensity
I_1	Light intensity after the first polarizer
δ	Angle between the analyzer and the optic axis
φ	Polarization phase shift of the light
I_{in}	Intensity of incident light measured before passing through the sample
I_{out}	Intensity of incident light measured after passing through the sample
λ	Wavelength of the electromagnetic radiation

d_n	Separation of lattice plane
$\overrightarrow{R}$	A position vector
$\overrightarrow{k_s}$	Wave vector
$\overrightarrow{k_o}$	Wave vector
$\overrightarrow{q}$	Scattering vector
q	Magnitude of the scattering vector
$\overrightarrow{E}_{dipole}$	Electric field of an individual dipole
$\overrightarrow{r}$	A position vector
$\overrightarrow{p}$	A vector associated with the induced dipole moment
$\overrightarrow{D}_i$	Induced dipole moment
α_i	Polarizability of the material associated with the dipole element
$\overrightarrow{E_S}$	Electric field at $\overrightarrow{r_i}$
$\overrightarrow{E}_{incident,i}$	Electric field associated with the incident
$\overrightarrow{E_j}$	Electric field comes from the other dipole
$\overrightarrow{r_{ij}}$	Positions of each element
$\overrightarrow{p_j}$	Induced dipole moments of each element
$\hat{p_j}$	Projection along the unit vector
Q_{sca}	Scattering efficiency
$\overrightarrow{E}_{scattered}$	Scattered electric field associated with the collection of dipoles
$\overrightarrow{E}$	Electric field
$\overrightarrow{H}$	Magnetic field,
$\overrightarrow{D}$	Electric flux densities
$\overrightarrow{B}$	Magnetic flux densities
$\varepsilon(\omega)$	Angular frequency of the incident radiation
$\varepsilon(\overrightarrow{r})$	A position dependent permittivity
$\mu(\overrightarrow{r})$	A position dependent permeability
$\varepsilon(\overrightarrow{\omega})$	A frequency dependent permittivity
M_{ij}	Interaction matrix
^{0}C	Celsius
τ	Rise time or disintegration time
Å	Ångström, 0.1 nanometer
R_{eq}	Equilibrium bubble radius
$T(r)$	Temperature as a function of radial distance
$T(\infty)$	Ambient temperature far from the NAM
κ_{LC}	Thermal permeability of the LC
ρ_V	LC density
C_p	Specific heat

β	β is equal to $\frac{\kappa_{LC}}{\rho_V C_p}$	Q_{in}	Heat generated by incident excitation
T_{NI}	Nematic-isotropic critical temperature	$\triangle T$	Changing temperature: $\equiv T(r) - T(\infty)$
$r(t)$	Bubble radius as a function of time	$\triangle T_{max}$	Maximum changing temperature
$\dot{Q_{in}}$	Heat flux created by incident excitation		

List of Figures

Acknowledgements

This dissertation would not have been possible without the help and support of so many people.

First and foremost, I would like to express my sincere gratitude to my Ph.D. thesis advisor, Professor Sayantani Ghosh, for giving me the opportunity to be involved in the field of plasmonics. I can never thank her enough for her unbelievable perseverance and the trust she bestowed on me. She created for me precious opportunities to be able to participate and to present our works in numerous conferences. She also supported me in difficult times, believed in me, and gave me a lot of suggestions when I was wandering at the crossroad, for which I really appreciate. Her support is why I was able to carry out my research to a successful conclusion. I could not have imagined having a better advisor and mentor for my Ph.D. study.

I would like to give a very special appreciation for my collaborator, Professor Kerwyn Casey Huang, who provided me the opportunity to collaborate with his team, and who gave access to the laboratory and research facilities at Stanford University. All his support during the past two years opened a window for me to see the top scientific research world and provided me the exceptionally good atmosphere that allowed me to achieve in collecting the great experimental data ever and in presenting these results in the best possible conditions. Without his support and that of his group members, it would not be possible to conduct this research. My special words of thanks should also go to my co-adviser Professor Linda Hirst for her support. She helped me to understand different aspects of liquid crystal physics. Similar, profound gratitude goes to Professor Ajay Gopinathan. He has derived mathematical models of photothermal heating in our system. I greatly appreciate the support and help received through his collaborative work.

Besides my advisor, co-advisor, and collaborators, I would like to thank the rest of my thesis committee chair, Professor Jay E. Sharping, and a committee member, Professor Jennifer Lu, for their insightful comments, encouragement and guidance. Their support pushed me to widen my research from various perspectives.

Additionally, I would like to thank all my friends and the present/former fellows of the Ghosh's group, in particular Dr. Andrea Rodate. Considerably, with her time and supportive comments in my first years of my Ph.D., teaching me the majority of what I

now know.

I am grateful for the funding sources that allowed me to pursue my graduate school studies: Center for Cellular and Biomolecular Machines Fellowship, Physics Graduate Dissertation Fellowship, Faculty Mentor Program Fellowship, UCMEXUS-CONACYT, National Science Foundation, the NSF nanoBIO node, A James S. McDonnell Foundation Award, and the NSF-CREST: Center for Cellular and Bio-molecular Machines (CCBM) at University of California, Merced.

I would like to acknowledge my co-authors, Silverio Delgado, John. H. Paredes, Zachary S. Nuno, Linda S. Hirst, and Sayantani Ghosh, who coauthored the study which comprises Chapter 4. This study was published in the journals, Proceedings of SPIE [1] and Optics Express [2]. The dissertation author is a first author on the publications and the published work is reproduced by permission from The Optical Society of America and the International Society for Optical Engineering. Special mention goes to Andrea L. Rodarte, Blessing H. Cao, Harmanpreet Panesar, Ronald J. Pandolfi, Lauren Edwards, Sayantani Ghosh, Jason E. Hein, and Linda S. Hirst, who first authored or co-authored the study which partially comprises Chapter 5. The dissertation author is a co-author on the publications and this work was previously published in journal, Soft Matter [3]. Similar, profound gratitude goes to Som Sarang, David A. Quint, Amir Keshavarz, Benjamin J. Stoke, Anand B. Subramaniam, Kerwyn Casey Huang, Ajay Gopinathan, Linda. S. Hirst, and Sayantani Ghosh, who are co-authors on the study which comprises Chapter 6 and which was published in journal, Scientific Reports [4].

As always it is impossible to mention everybody who had involved to this work, however there are those whose spiritual support is equally significant. I would also like to take this opportunity to thank my parents, who formed part of my vision and taught me the things that really matter in life. They also have been a constant well of encouragement, believing in me and supporting all my decisions, especially when I decided to start my education in the US. Thank you for understanding how important this decision was to me and for supporting me every step of the way.

My heart-felt regard goes to my sister, father in-law, mother in-law, and brother in law for their love, their great support, and understanding. Additionally, I am grateful to all my immediate and extended family members for their constant inspiration and encouragement.

And last but not least, I would like to say a special thank you to my husband, David, who understands and patiently assists me with achieving my goals in every situation I had for the last four years and three months. Thank you for having faith in me when I started to lose it in myself and for not letting me give up, even through a lot of frustrations. He also has been the necessary driving force to reach the end of this thesis. Without you, I could not have done this. You are an equal part in this accomplishment. I love you with all that I have.

Without all those people who provided me the significant influence on my career, this work would not exist. Words would never say how grateful I am to all of you.

Curriculum Vitae

Makiko T. Quint

Ph.D. Candidate, Physics
University of California, Merced
School of Natural Sciences
5200 N. Lake Rd. Merced, CA 95344

Advisor: Prof. Sayantani Ghosh
Co-advisor: Prof. Linda S. Hirst

Education

2013-2017: Doctor of Philosophy, Physics, University of California, Merced, California

- (GPA =3.85/4.0; 4.0 =A)

2005-2007: Bachelor of Science, Physics, Syracuse University, Syracuse, New York

- Honors: Cum Laude 2007 (GPA =3.77/4.0; 4.0 =A)

Fellowships and Awards

- 2017: Center for Cellular and Biomolecular Machines Fellowship
  - Awarding institution: University of California, Merced
- 2017: Physics Graduate Dissertation Fellowship
  - Awarding institution: University of California, Merced
- 2015-2016: Faculty Mentor Program Fellowship
  - Awarding institution: University of California, Merced

- 2015: Outstanding Performance in Research and Publication Awards
  - Awarding institution: University of California, Merced
- 2007: Outstanding Academic Achievement in Physics
  - Awarding institution: Syracuse University
- 2007: Syracuse University Academic Excellence
  - Awarding institution: Syracuse University
- 2005-2007: Phi Theta Kappa/ Phi Beta Delta Scholarship
  - Awarding institution: Syracuse University

Research Publicity

1. Clare Mahoney. "Conference Report on the MRS Meeting 2016." Liquid Crystal Today, 2017, VOL 26, NO.1, 14-16. https://doi.org/10.1080/1358314x.2017.1279447.

Publications

1. **Makiko T. Quint**, Som Sarang, David A. Quint, Amir Keshavarz, Benjamin J. Stokes, Anand B. Subramaniam, Kerwyn Casey Huang, Ajay Gopinathan, Linda S. Hirst, and Sayantani Ghosh. "Plasmon-actuated nano-assembled microshells." Scientific Reports, 7. 17788 (2017). DOI:10.1038/s41598-017-17691-6.

2. Jose Jussi Amaral, Edwin Betady, **Makiko T. Quint**, Denzal Martin, Sheida T Riahinasab, Linda S Hirst and Sayantani Ghosh. "Effect of mesogenic ligands on short and long-term spectral dynamics and stability of core–shell CdSe/ZnS quantum dots." Materials Research Express. 3(10). 105029. (2016). DOI:10.1088/20-53-1591/3/10/105029.

3. **M.T. Quint**, S. Delgado, Z.S. Nuno, L.S. Hirst, and S. Ghosh. "Optical switching of nematic liquid crystal film arising from induced electric field of localized surface plasmon resonance." Proc. SPIE 9547,Plasmonics:Metallic Nanostrcutures and Their Optical Properties XIII, 954729 (2015).

4. **M.T. Quint**, S. Delgado, Z.S. Nuno, L.S. Hirst, and S. Ghosh. "All-optical switching of nematic liquid crystal films driven by localized surface plasmons." Optics Express, 23. 16888-6895 (2015).

5. A. Rodarte, B. Cao, H. Panesar, R. J. Pandolfi, **M. Quint**, L. Edwards, S. Ghosh, J. Hein, L. S. Hirst. "Self-Assembled nanoparticle micro-shells templated by liquid crystal sorting." Soft Matter, 11. 1701-1707 (2015).

6. J. Amaral, J. Wan, A. Rodarte, **M. Quint**, R.J. Pandolfi, M. Scheibner, L.S. Hirst, S. Ghosh. "Magnetic field induced quantum dot brightening in liquid crystal synergized magnetic and semiconducting nanoparticle composite assemblies." Soft Matter, 11. 255-260 (2015).

7. Andrea L. Rodarte, Zachary S. Nuno, Blessing H. Cao, Ronald J. Pandolfi, **Makiko T. Quint**, Sayantani Ghosh, Jason E. Hein and Linda S. Hirst. "Tuning Quantum Dot organization in liquid crystal for Robust Photonics Applications." ChemPhysChem. 15, 7. 1225–1518 (2014).

Presentations

1. NSF Center for Cellular and Biomolecular Machines External Advisory Board Meeting (August, 2017)
2. American Physical Society March Meeting (March, 2017)
3. International Liquid Crystal Conference (August, 2016)
4. Plasmonics & Nanophotonics Gordon Research Conference (July, 2016)
5. Plasmonics & Nanophotonics Gordon Research Seminar (July, 2016)
6. Nano Bio Node Meeting (April, 2016)
7. Plasmonics and Its Applications Meeting (March, 2016)
8. Material Research Society Spring meeting (March, 2016)
9. American Physical Society Far West Meeting (October, 2015)
10. International Society for Optics and Photonics (August, 2015)
11. 2015 BioNanotechnology Summer Institute (July, 2015)
12. Nano Bio Node Meeting (April, 2015)
13. American Physical Society March Meeting (March, 2015)
14. American Physical Society Far West Meeting (October, 2014)
15. Nano Bio Node Meeting (April, 2014)
16. American Physical Society March Meeting (March, 2014)

Professional Affiliations

- Materials Research Society (MRS)
- International Society for Optics and Photonics (SPIE)
- American Physical Society (APS)

Abstract

Development and Characterization of Liquid Crystal-Gold Nanoparticle Hybrid Materials for Optical Applications

by

Makiko T. Quint

Doctor of Philosophy in Physics

University of California, Merced

Professor Jay E. Sharping, Chair

Hybrid material, mixtures of two or more materials with new properties, represents an exciting class of new materials for a variety of potential applications such as displays, optoelectronics, and sensors due to their unique physical and optical properties. The scope of this dissertation is to produce two new plasmonic applications by combining liquid crystals with gold nanoparticles. The first application is gold nanoparticle coated liquid crystal thin film. Most liquid crystal (LC) thin films require external voltage to reorient LC molecules. Recent advances in optical controlling technology of LC molecule behavior, resulting in the reduction of energy consumption, have stimulated research and development of new LC thin films. In order to re-orient LC molecules by just using light, the common approach is to include either a photo-responsive LC host, one that require high power light and severely narrows the range of usable materials, or add photo-active dye or polymer layer, photodegradation over time. Our work designing an all-optical method for LC re-orientation that overcomes all the limitations mentioned above. We have successfully both in- and out-of-plane spatial orientation of nematic liquid crystal (LC) molecules by leveraging the highly localized electric fields produced in the near-field regime of a gold nanoparticle (AuNP) layer. This re-orientation of LC molecules in thin LC-AuNP film is all-optical, driven by a small resonance excitation power with the localized surface plasmon absorption of the AuNPs at room temperature. The second application is LC mediated nano-assembled gold microcapsules. This application has a potential in controlled-release

cargo-style delivery system. Targeted delivery systems with controlled release mechanisms have been the subject of extensive research more than fifty years. One is to control the release process remotely by using optical excitation. Optical actuation of delivery capsules, which plasmonic nanoparticle such as gold, allows rapid release at specific locations and uses the photothermal effect to unload contents. Almost all gold-based delivery applications including Au coated nanocrystals or AuNPs with soft materials like gels and polymers are not suitable for control release applications in real life since these applications do not provide robust leakage-free containment lower than the American National Standards Institute (ANSI) maximum permissible light exposure limit. We have successfully managed the difficulties mentioned above and produced a new gold-based delivery application. The application is spherical capsules with a densely packed wall of AuNPs. The rigid capsule wall allows encapsulation of cargo that can be contained, virtually leakage-free, over several months. Further, by leveraging LSPR of AuNPs, we can rupture the microshells using optical excitation with ultralow power (< 2 mW), controllably and rapidly releasing the encapsulated contents in less than 5 seconds. Our results exhibiting the capture and optically regulated release of encapsulated substances are a novel platform that combines controlled-release cargo-style delivery and photothermal therapy in one versatile and multifunctional unit. Both our applications are overcoming current limitations and promising future research directions towards the next generation of LC-AuNPs hybrid material research and developments.

Chapter 1

Motivation and overview

The scope of this dissertation is to characterize in detail two different applications by combining gold nanoparticles and liquid crystals. My work has been focused on overcoming current limitations and introducing better approaches. Before I discuss these applications, I will first introduce basic concepts of physical and optical properties of liquid crystals and plasmonic/semiconductor nanoparticles, detailed in Chapter 2. Chapter 3 describes the experimental methods used in this dissertation. Below describes current limitations for the applications I studied, motivation of this dissertation, and a summary of my work that I will present in the Chapter 4 though 7.

My first study was focused on the coupling behaviors of gold nano-particle with a thin film of liquid crystal (LC). Most LC thin films require applying external electric field to re-orient LC molecules. Research and development of new LC thin films have been progressing at a fast pace in the field of nanoscience by applying optical controlling technology of LC molecule behavior. This may lead to the enormous reduction of energy consumption in the world. In order to re-orient LC molecules utilizing light, the current main approach is to include either a photo-responsive LC material, one that requires high power laser beam, causing permanent damage of the material itself, and severely narrows the range of usable materials. The other method is combining a photo-active dye or polymer layer with LC host material. Unfortunately, the material stability of photo-active dye or polymer layer does not last long due to photodegradation over time.

The first motivation for this dissertation is to design and implement an all-optical method for LC re-orientation that overcomes all the limitations mentioned above. Chapter 4 describes our achievement of the first motivation. We have produced both in- and out-of-plane spatial orientation of LC molecules by leveraging the highly localized electric fields produced in the near-field regime of a gold nanoparticle (AuNP) layer. This re-orientation of LC molecules in thin LC-AuNP film is all-optical, driven by a very small resonance excitation power with the localized surface plasmon absorption of the AuNPs at room temperature.

Our second all-optical LC-AuNP application was forming and studying "self-assembled" nano-gold microcapsules. This application has a high potential in controlled-release cargo-style delivery system. Targeted delivery systems with controlled release mechanisms have been the popular subject of extensive research more than half century. One technique is to control the intact material release process remotely by applying optical excitation. Optical actuation of delivery capsules, made of plasmonic nanoparticles such as gold, leads rapid release at targeted locations and uses the photothermal effect, plasmonic heat, to unload the contents. Most current gold-based delivery applications including gold-coated nanospheres or combining AuNPs with soft materials, like hydrogels or polymers, have been facing challenges and difficulties for control release applications in real life. This is because these applications do not satisfy robust leakage-free containment lower than the American National Standards Institute (ANSI) maximum permissible light exposure limit.

Our second motivation for this dissertation is that we develop and characterize a new type of leak-free and controlled-release cargo-style delivery system satisfied ANSI standards. For visible optical excitation at $\sim$ 500 nm, which we applied in our application, this limit is 2.5 mW for up to 10 min exposure [5]. We have successfully managed these difficulties mentioned above and produced a new gold-based delivery application. Chapter 5 explores the formation mechanism of our self-assembled nanoparticle microcapsules, their formation process, observation of liquid crystal defects around the microcapsules, and the particle packing characterizations. Chapter 6 discusses the successful results of our work produced spherical capsules with a densely packed wall of AuNPs. The rigid capsule wall allows virtually leakage-free encapsulation of cago over five-month periods. Moreover, by leveraging optical properties of AuNPs, we can disintegrate the microcapsules using excitation light with ultralow power, less than 2.5 mW, controllably and rapidly releasing the encapsulated contents in less than five seconds exposure.

Chapter 7 further explores important implications of nano-gold microcapsules. Our microcapsule application has the great potential to develop biological and biomedical applications. These capsules can be utilized to deliver live cells, such as stem cells or prokaryotes, and growth factors for cell differentiation as well could promote further chemical reagent transport and development. Our microcapsules captured live multicellular prokaryotes, E. coli. This chapter also considers future directions for the research, such that we are currently in the process of optimizing to use our microcapsule for biological and chemical engineering applications.

Chapter 2

A review of contemporary nanoparticles and liquid crystals: their properties and characteristics

In this chapter, I discuss the analytical expressions for the properties of gold nanoparticles, semiconductor quantum dot nanoparticles, and liquid crystals. I also describe an analytical model for the optical and electric properties of gold and colloidal semiconductor nanoparticles. The first section starts with general explanation of nanoparticles, then expresses optical, electric, and plasmonic heating properties of gold nanoparticles. Additionally, I discuss optical and electric properties of colloidal semiconductor nanoparticles, quantum dots, and strong electromagnetic forces exerted by a strongly focused. After that, I go through the formalism to understand a theoretical overview of the physical, electrical and optical properties of nematic liquid crystals. Nematic liquid crystal exhibits dielectric anisotropy and birefringence in the electronic and visible region of the electromagnetic spectrum. Finally, as each of these properties is related to the self-organization of the liquid crystal, they are all highly dependent on minimizing the elastic free energy.

2.1 Nanoparticles

Nanoparticles are the most fundamental component in the fabrication of a nanostructure, and is far smaller than the everyday objects we use. For example, roughly eight hundred 100 nm-sized nanoparticles are required to match the width of a human hair. The size of nanoparticles has the range between 1 and 100 nm, however nanoparticles used in the field of biotechnology range in particle size between 10 and 500 nm [6]. A number of artificial or engineered NPs have been developed. Some of these engineered NPs are already in use in consumer products such that titanium oxide nanoparticles are added to cosmetics

and zinc oxides are added to sunscreen products. The engineered nanomaterials, especially metallic and semiconductor nanoparticles, show promise in advancing the fields of medical and electronic future applications based on their unique optical characteristics.

Metallic nanoparticles have different physical and chemical properties from bulk metals. Compared with bulk metal, metallic nanoparticles have lower melting points, higher surface areas, specific optical properties, higher mechanical strengths, and better magnetizations properties. Thus, with wide range of applications available, nanoparticles have made a significant impact to society such as developing electronic storage systems [7], biotechnology [8], magnetic separation and targeted drug delivery [9, 10], and modifying vehicles for gene and drug delivery [7, 9, 10]. In particular, the optical property is one of the fundamental attractions and a characteristic of a nanoparticle. For instance, a 20-nm gold nanoparticle has a characteristic wine red color. A silver nanoparticle is yellowish gray color. Not surprisingly, the unique optical characteristics of nanoparticles have been used even before the 4th century AD. The most famous example is the Lycurgus cup (Figure 2.1). The cup is made of very special type of glass, known as dichroic glass, that changes color when light is applied on the surface of the cup. The green color turns to a red when light is passed through it internally. Based on the analysis of the glass, it was revealed that the glass contains a very small quantity of metallic nanocrystals of silver and gold. The approximate molar ratio of silver and gold is $14 : 1$ [11], which create these unique optical properties.

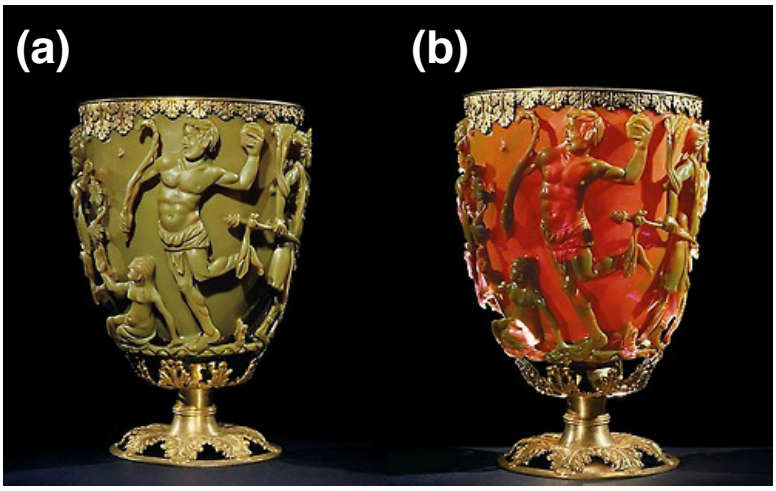

Figure 2.1: The Lycurgus Cup in reflected (a) and transmitted (b) light. (Image courtesy of © the Trustees of the British Museum.)

Semiconductor nanocrystals are also small crystalline particles. The particles show size-dependent optical and electronic properties [12–14]. Early studies on semiconduc-

tor nanocrystals made use of particles embedded in glass matrices, similar to centuries-old stained glass containing semiconductor crystallite pigments [15–17]. Today, these nanocrystals are commonly fabricated as colloids suspended in solution or as epitaxial structures grown on solid crystalline substrates. Epitaxial nanocrystals can be reproducibly prepared with a wide range of shapes and sizes in regular patterns and directly incorporated into optoelectronic devices [18]. The optical properties of semiconductor nanoparticles are favorable for in vitro and in vivo labeling, tracking, and sensing applications. This is because semiconductor nanoparticles have narrow emission and broad absorption profiles with a high quantum yield [19, 20]. Additionally, semiconductor nanoparticles have been reported they have significant resistance to photobleaching as compared to organic fluorescence dyes [21, 22].

Nanomaterials and devices are still in the research stage, but they are promising for applications in many fields, such as solar cells, nanoscale electronic devices, light-emitting diodes, laser technology, biosensors, and catalysts. Further development of nanomaterial research will certainly lead to significant future breakthroughs in the field of nanotechnology.

2.2 Gold nanoparticles

Colloidal gold, also known as a gold nanoparticle, is a nanometer-sized particle of gold. In 1857, Michael Faraday for the first time produced "colloidal gold" in solution and observed their unique optical properties [23]. The actual scientific study on gold nanoparticles started in 1908 when Gustav Mie described a mathematical explanation by using Maxwell equations that described the extinction spectra of spherical and ellipsoidal nano-objects that demonstrated the optical properties of metallic colloids [24].

The dominating optical feature of AuNPs with size of 2 to 100 nm is the localized surface plasmon resonance. Localized surface plasmon resonance (LSPR) is an optical phenomena induced by light when the light interacts with nanoparticles that are smaller than the incident wavelength [25]. Compared to any other chromophores, smaller gold nanoparticles, sizes between 2 to 20 nm have higher absorbance with a possibility of reaching high light-to-heat conversion efficiency [26]. In contrast, particle sizes above 20 nm, have larger extinction cross-sections, high photostability, and the ability to amplify the electromagnetic field near the metal surface [26].

The optical properties of spherical gold nanoparticles are highly dependent on the nanoparticle diameter. Figure 2.2 shows a strong extinction, the sum of scattering and absorption, maximum between 510-580 nm in aqueous solution due to their LSPR. Smaller gold nanoparticles absorb light and have peaks near 520 nm, while larger spheres exhibit increased scattering and have peaks that broaden significantly and shift towards longer wavelengths. Larger gold nanoparticles scatter more light both because they have larger optical

cross sections, and increase a ratio of scattering to total extinction [26]. With the development of nanoscience, the optical properties of gold nanoparticles have shown tremendous interest in plasmon-based technologies. Localized surface plasmons can be excited by optical excitation, leading to the device development of small-scaled optical antenna with enhanced electric fields [27]. Since optical properties of gold nanoparticle have brought new insights in our modern society, understanding the fundamental mechanism of the optical phenomena is important. In the following sections, we present the fundamental concepts of the relation between localized surface plasmon resonance and optical properties of gold nanoparticles.

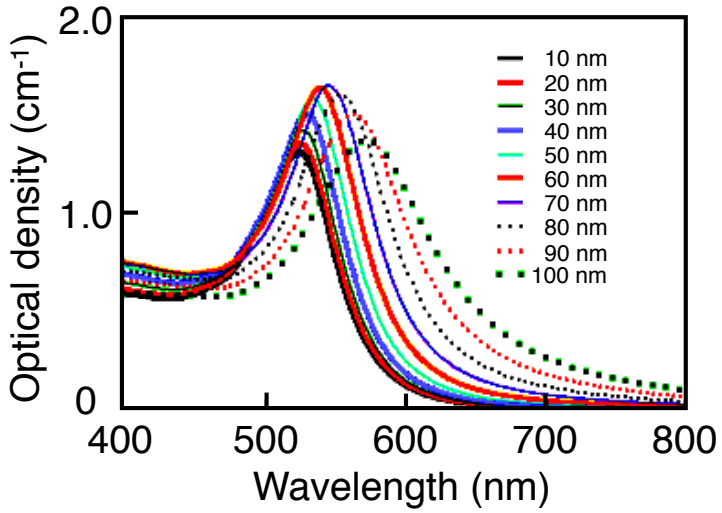

Figure 2.2: Extinction spectra of gold nanoparticles with diameters ranging from 10 to 100 nm at mass concentrations of 0.05 (mg/mL). (Image courtesy of © 2017 the nanoComposix, Inc.)

2.3 Localized surface plasmon resonance

When gold nanoparticles are illuminated by resonance light, a part of the incident light is absorbed in moving the conduction band electrons towards the nanoparticle surface [28]. This leads to move a negative charge on one side, and an equal positive charge at the other side of the nanoparticles, therefore creating a dipole. The dipole creates an electric field inside of the nanoparticle and gives rise to a linear restoring force. The restoring force on the electrons forces them to return to the equilibrium position. As a result, a dipolar oscillation of electrons is produced, which is known as plasmon resonance frequency [29]. The

collective oscillations of the conduction band electrons in gold nanoparticles are known as plasmons (Figure 2.3) [28]. As a consequence of these dipole oscillations, light is radiated

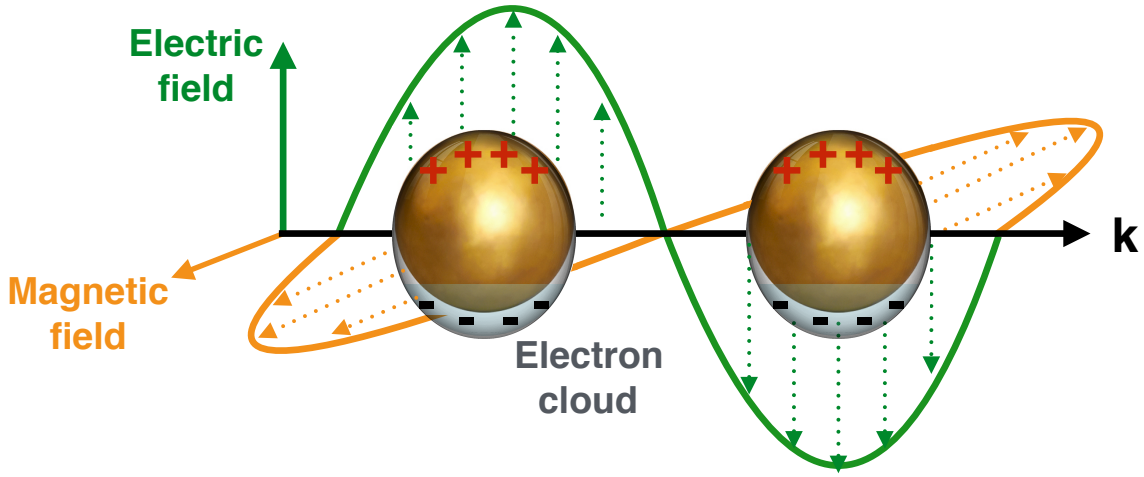

Figure 2.3: Extinction of particles plasmons through the polarization of metallic nanoparticles. At the resonance frequency the plasmons are oscillating with 90^o phase difference. The k-axis represents the light wave direction.

from the nanoparticles in the form of scattering [30]. Additionally, the dipolar oscillations are produced on the surface of gold nanoparticles, thus this circumstance is called as Localized Surface Plasmon Resonance (LSPR) [28]. There are several theories describing the plasmons in gold nanoparticles. We describe the most well-known theory here.

The electrostatic approach, quasi static approximation, explains a qualitative descriptions such as the amount of light a gold nanoparticle can absorb or scatter. The collective oscillation of free electrons in gold nanoparticles is described by the polarizability α:

$$\alpha(\lambda) = \frac{1}{\zeta}\varepsilon_0 V \frac{\varepsilon(\lambda) - \varepsilon_m}{\varepsilon(\lambda) + \kappa\varepsilon_m} \tag{2.1}$$

where ε_0 is the permittivity of free space, V_P is the volume of a gold nanoparticle, ε_m is the dielectric constant of the surrounding medium, κ is the light absorption coefficient, ζ is the shape factor, $\zeta = \frac{1}{3}$ for spherical particles, that includes the dependence of the polarizability on the geometry of the surface, $\varepsilon(\lambda)$ is the dielectric function of the gold nanoparticle, and λ is the wavelength for an electromagnetic radiation.

The dielectric function of the gold nanoparticle $\varepsilon(\lambda)$, is frequency dependent and has real and imaginary parts such as

$$\varepsilon(\lambda) = \varepsilon_1(\omega) + \varepsilon_2(\omega) \tag{2.2}$$

where ω is the frequency of the electromagnetic radiation.

Using the polarizability, we can express the induced dipole moment, P, that results from electronic polarization is described by

$$P = \varepsilon_m \alpha E_0 \tag{2.3}$$

where E_0 is the applied field.

The electric field, E_d, produced by the dipole inside a gold particle is expressed by the equation:

$$E_d = E_0 \frac{3\varepsilon_m}{\varepsilon(\lambda) + 2\varepsilon_m} \tag{2.4}$$

Localized surface plasmon resonance occurs for polarizability and dipole electric field when the denominator of the equation 2.4 becomes minimum:

$$\big[\varepsilon_1(\omega) + 2\varepsilon_m\big]^2 + \big[\varepsilon_2(\omega)\big]^2 = minimal \tag{2.5}$$

The equation 2.5 is satisfied when $\varepsilon_1(\omega) = 2\varepsilon_m$, which is known as Fröhlich condition, and $\varepsilon_2(\omega) << 1$. Gold nanoparticles are unique because the Fröhlich condition is satisfied in the visible region, which indicates the gold nanoparticles are a valuable material for devices that allows optical signals to be controlled at sub-wavelength scale. Generally, the real part $\varepsilon_1(\omega)$ of the gold nanoparticle dielectric function represents the frequency position of the plasmon resonance, while the imaginary part $\varepsilon_2(\omega)$ indicates the width and height of the localized surface plasmon resonance.

If we investigate the response of a gold nanoparticle to an external electromagnetic field, then solving Maxwell's equations is required. The solution of Maxwell's equations already exists and is known as "Mie Theory." The theory is valid for all gold nanoparticle sizes and all optical wavelengths. Mie reported the interaction between a plane wave and uncharged homogeneous particles. This interaction allowed the precise calculation of the electromagnetic fields such as understanding multipole expansion of the fields based on the spherical geometry. As a result, the calculation of the extinction (σ_{ext}), scattering (σ_{scat}), and absorption cross-sections (σ_{abs}) of the gold nanoparticles were determined.

$$\sigma_{ext} = \frac{2\pi}{|k^2|} Re \sum_{L=1}^{\infty} \big(2L+1\big)\big(a_L + b_L\big) \tag{2.6}$$

$$\sigma_{scat} = \frac{2\pi}{|k^2|} \sum_{L=1}^{\infty} \big(2L+1\big)\big(|a_L|^2 + |b_L|^2\big) \tag{2.7}$$

$$\sigma_{abs} = \sigma_{ext} - \sigma_{scat} \tag{2.8}$$

where a_L and b_L represent Mie-coefficients from the multipole expansion, L illustrates the multipole order, $L = 1$ for dipole mode, and k is the wave vector of the incident electromagnetic wave.

For a spherical gold nanoparticle that is much smaller than the wavelength of the incident light, such as the diameter size from 2 to 200 nm, the equation 2.6 can be simplified to:

$$\sigma_{ext} = 9 \cdot \frac{\omega}{c} \cdot (\varepsilon_m)^{\frac{3}{2}} \cdot V \frac{\varepsilon_2(\omega)}{\left[\varepsilon_1(\omega) + 2\varepsilon_m\right]^2 + \left[\varepsilon_2(\omega)\right]^2} \tag{2.9}$$

Absorption and scattering properties of gold nanoparticles are heavily dependent on localized surface plasmon resonance and can be influenced by nanoparticle size, shape and surrounding medium. Difference particle sizes and shapes can change electron density or volume of gold nanoparticles, hence leading to create new resonance condition. Similarly, external dielectric medium also affect the condition of localized surface plasmon resonance. During the excitation of localized surface plasmons, the dipole of opposite charges produced on the surface of the nanoparticles generates an electric field in the surroundings of the nanoparticles. This field induces the polarization of the dielectric medium. The polarization accumulates the charges in the medium and interfaces with the surface of the gold nanoparticles [31]. As a result, both the dielectric medium and the gold nanoparticles polarize each other. This polarization tends to compensate the charge accumulation by cause of the movement of conduction electrons in the nanoparticles [31]. Therefore, the net charge at the nanoparticle surface gets reduced. The adjustment of the charge density is due to the dielectric function of the surrounding medium, ε_m. That is, the larger the ε_m, the polarization of the medium turns into larger and the effect of the charge compensation effect becomes more. Reduction of the net charge at the nanoparticle surface causes diminishing restoring force. The Lowering the restoring force leads to smaller resonance frequency. Additionally, the dielectric function of the medium ε_m is related to its refractive index, n, expressed as $n^2 = \varepsilon_m$. Therefore, the surface plasmon band gets red-shifted to larger wavelengths when the refractive index value of the surrounding medium becomes higher.

2.4 Plasmon coupling of gold nanoparticles

As we discussed in the previous sections, surface plasmon resonance interacts strongly with gold nanoparticles and induces a collective electron oscillation when a resonance light excites the electrons in the nanoparticles. The oscillations introduce localized non-radiating electric field, called near-field, that contain large wave vector values (high spatial frequency) [32]. Some of these created wave vectors can couple to surface plasmon modes on the surface of the gold nanoparticles. This is because the absorption depends on the interparticle distance and the incident light polarization since the particles are coupled through near-field interaction. Due to the localized capacitive coupling at the nano gap surrounded by nanoparticles, emission between particles is strongly enhanced compared to a single particle (Figure 2.4). The enhancement originates from the charge induction

between nanoparticles, which becomes stronger as they get closer to each other [33]. This relation between the field enhancement factor of the nanoparticle dimer and gap distance is evidently described in Figure 2.4.

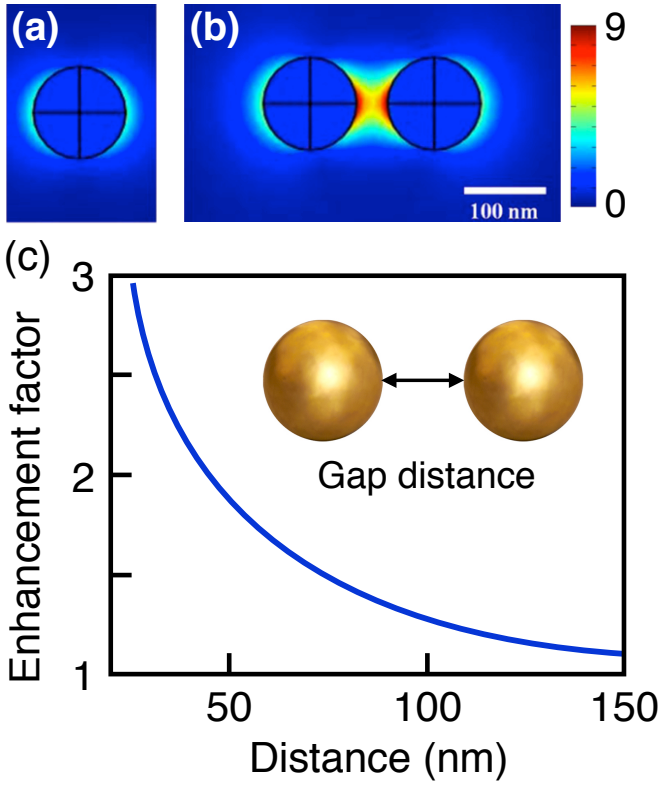

Figure 2.4: Electromagnetic field distribution around (a) 100 nm-sized single gold nanoparticle and (b) gold nanoparticle dimer. The incident wavelength of light is 633 nm and the magnitude of incident electric field is 1 (V/m). (c) Enhancement factor of each sphere in the gold sphere dimer as a function of inter-particle gap. (Reproduced from reference [33] with permission from the MDPI.)

Figure 2.5 shows the electric field amplitude distribution around 100 nm-sized gold nanoparticles at six different excitation wavelengths from 550 to 800 nm. Based on the map, the peak resonance wavelength of the gold nanoparticles was between 550 and 600 nm (first row of Figure 2.5), which agreed with the Mie calculation of 580 nm [34]. A dimer structure with a 20 nm particle-particle gap, which is shown in second row of the Figure 2.5, has the strongest coupling enhancement. The resonance peak of the strongest interparticle coupling is red-shifted to between 650 and 700 nm. The increasing the particle numbers, such as 3, 7, and 12, produces various degrees of enhanced electric fields within the gold

nanoparticles at wavelengths longer than 700 nm (3rd-5th row of Figure 2.5). These experimental results state that signal enhancement increases in shortening the interparticle distance, and the resonance peak is red-shifted when the number of the gold nanoparticles increases. That is, coupling enhancement behaviors can be verified investigating on the resonant spectrum of metallic nanoparticle array. The number and position of nanoparticle array is arbitrarily varied in attempt to identify the optical resonant response.

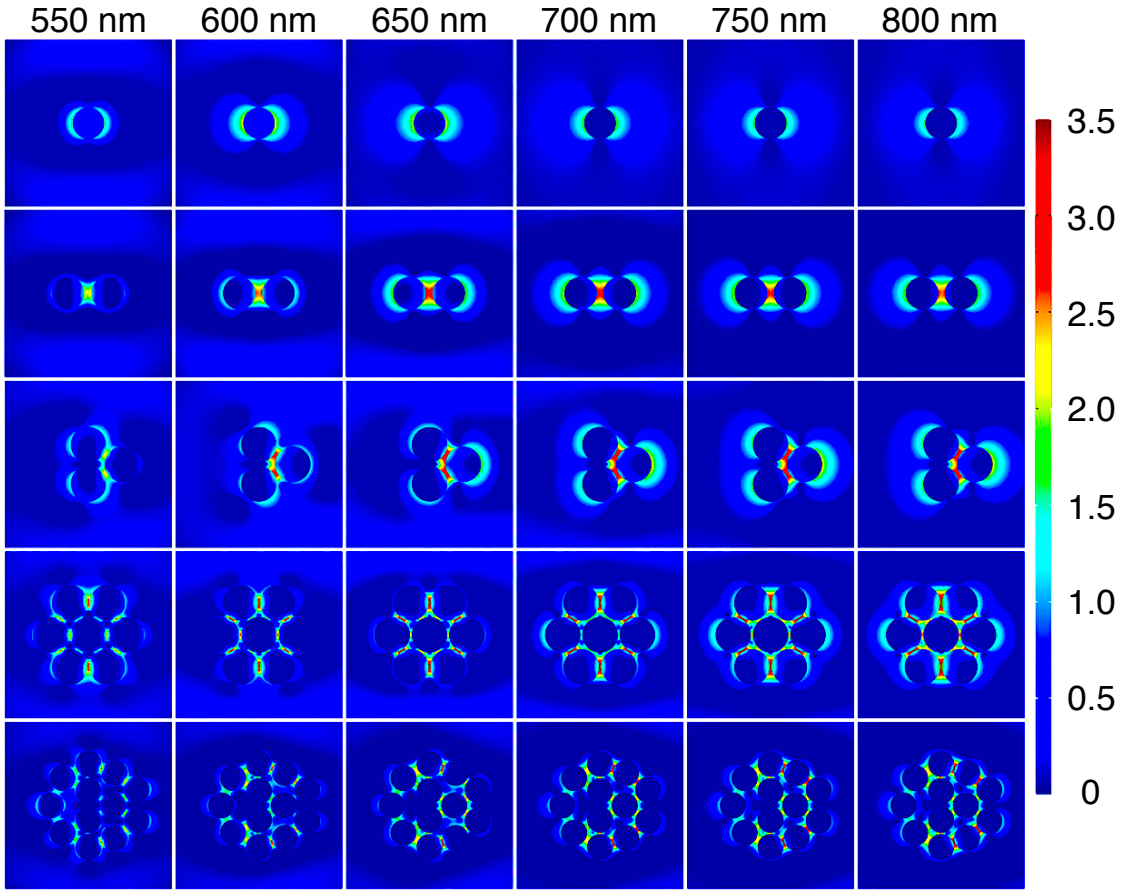

Figure 2.5: Electromagnetic simulations demonstrating the complex spectral properties of large nanoparticle clusters with excitation wavelengths from 550 to 800 nm. Normalized electric field plot in log scale. In the middle plane of clusters are composed of 1, 2, 3, 7, and 12 spherical 100 nm-sized gold nanoparticles. The distance between adjacent gold nanoparticles is between 5 and 20 nm. The surrounding medium is water and polarization of the excitation is in the horizontal direction. (Reproduced from reference [34] with permission from the Royal Society of Chemistry.)

2.5 Plasmonic heat

Heat generation from gold nanoparticles induced by light absorption have been regarded as side effects that needed to be minimized. However, it has been realized recently that the heat creation is effective and local. The potential applications by using this heat become popular quickly in the field of nanotechnology such as photothermal cancer therapy.

As discussed in the previous section, gold nanoparticles show strong scattering and absorption of light at specific wavelength owing to their LSPR. The heating effect is proportional to the increasing effective absorption cross section in the region of the LSPR [35]. The energy of the excited plasmon decays two possible ways. One is a radiative decay, which corresponds to the elastic scattering of light, and the other is a non-radiative decay, which results into the temperature increase of the gold nanoparticle (Figure 2.6).

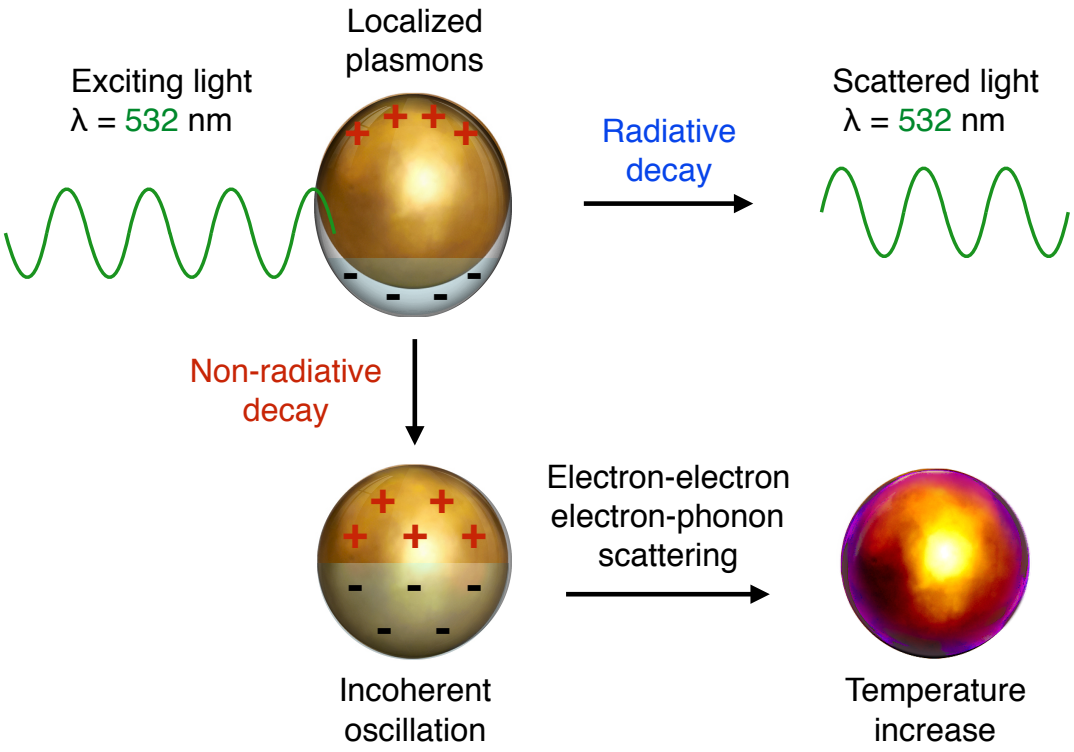

Figure 2.6: Decays of the localized surface plasmon. The radiative decay results in elastically scattered light of the same wavelength as the incident light. The nonradiative decay is connected to the loss of phase of oscillating electrons. Electron-electron and electron-phonon interactions lead to an increase of the temperature of the gold nanoparticles.

Specifically, the non-radiative decay is linked to incoherently oscillating electrons and transfers the energy from LSPR to phonons due to electron-electron and electron-phonon interaction [36]. The result of this process leads to the raised the temperature of the gold nanoparticle. The generated heat, then, diffuses away from the surface of the hot gold nanoparticle. This heat diffusion leads to the increase of the temperature around the gold nanoparticle. The diffusion of heat can be expressed by the following equation [35]:

$$\rho\big(\overrightarrow{r}\big)C_h\big(\overrightarrow{r}\big)\frac{\partial T\big(\overrightarrow{r},t\big)}{\partial t} = \bigtriangledown\kappa\big(\overrightarrow{r}\big) \bigtriangledown T\big(\overrightarrow{r},t\big) + Q\big(\overrightarrow{r},t\big) \tag{2.10}$$

where $T\big(\overrightarrow{r},t\big)$ is the temperature at the point with the coordinate $\overrightarrow{r}$ at time t, $\rho\big(\overrightarrow{r}\big)$ represents the density, $C_h\big(\overrightarrow{r}\big)$ is the heat capacity and $\kappa\big(\overrightarrow{r}\big)$ describes the thermal conductivity of the surrounding material. $Q\big(\overrightarrow{r},t\big)$ illustrates the heat source produced by the gold nanoparticle, which absorbs a fraction of the incident laser irradiation.

The gold nanoparticle can produce a constant amount of thermal energy when we irradiate the particle by a continuous wave laser. Simultaneously, the amount of the heat diffused to the surroundings determines by the temperature gradient of the gold nanoparticle. That is, the thermally stable state is created since the temperature distribution inside the system is constant in time. We can find the temperature increase around a spherical gold nanoparticle by using the equation [35] :

$$\triangle T\big(r\big) = \frac{QV_P}{4\pi k_0 r} \tag{2.11}$$

where V_P is the volume of gold nanoparticle, Q is the heat with constant thermal energy, k_0 the thermal conductivity of the surrounding medium, and r is the distance to the nanoparticle surface. The amount of the absorbed heat Q is calculated by using the previously introduced absorption cross-section of the gold nanoparticle such that

$$Q = \frac{\sigma_{abs} I_0}{V_P} \tag{2.12}$$

where I_0 is the intensity of the incident electromagnetic wave.

These equations contain important fundamental concepts necessary for heat generation with gold nanoparticles and excitation light. The optical properties, σ_{abs}, of a gold nanoparticle need to be obtained since the absorption cross-section is an effective area that absorbs the light energy. Especially, optical property influenced by the nanoparticle size or shape need to investigate either experimentally or theoretically. Additionally, the intensity of incident light needs to be known in order to estimate the heat generation and thermal response. Finally, the number and distribution of gold nanoparticles needs to be known to estimate the heat.

2.6 Colloidal quantum dot nanoparticles

Semiconductor nanocrystals, also known as colloidal quantum dots (QDs), are generally solution-processed semiconductors. Colloidal QDs have unique optical properties due to the quantum confinement effect. They can be chemically synthesized and be manufactured the various sizes less than 50 nm. Additionally, they possess a high quantum yield, narrow emission spectrum, and strong optical absorption. These characteristics has made them useful in a wide range of optoelectric applications [37–39]. QDs have unique optical and electrical properties due to its quantum effect and size effect. These aspects bring a very broad application prospect in biological fluorescent probes and functional materials. Therefore, QDs have been widely used in the field of life sciences as fluorescent markers [40, 41]. Herein, we briefly review the basic properties of QDs in the next few sections.

2.7 Optical properties of colloidal quantum dots

The optical properties of colloidal QDs change with size (Figure 2.7). On the other hand, for a confined particle, the uncertainty in position decreases whereas momentum uncertainty increases. These aspects allow us to understand the energy condition of a particle as a superposition of bulk momentum states. This phenomenon can be explained by using the uncertainty relationship between position and momentum for free and confined particles. For a free particle, momentum can be defined when the uncertainty in position increases. Similarly, the effect on optical properties due to the change in bandgap energy with change in size can be further understood of the characteristics of quantum dots (Figure 2.7). Semiconducting properties of nanoparticle arise from the periodic arrangement of atoms in a crystalline lattice [42]. The spatial over-lapping of the atomic orbitals leads to the formation of bands of the allowed electron and hole states separated by a forbidden gap called the band gap [12]. An electron excited from the valence band by the absorption of a quantum of light moves to the conduction band, leaving a positive charge (a hole) [42]. Brus introduced the approximate relationship between the energy bandgap and particle size [12].

The lowest excited energy state, E_g, can be approximated by

$$E_g = E_{g,bulk} + \frac{\hbar^2\pi^2}{2R_P^2}\Big(\frac{1}{m_e^* m_o} + \frac{1}{m_h^* m_o}\Big) - \frac{1.8e^2}{4\pi\varepsilon\varepsilon_o R_P} - \frac{0.124e^2}{\hbar^2(4\pi\varepsilon\varepsilon_o)^2}\Big(\frac{1}{m_e^* m_o} + \frac{1}{m_h^* m_o}\Big)^{-1} \tag{2.13}$$

where $E_{g,bulk}$ is the bulk band gap, $\hbar$ is Planck's constant, R_P is the particle radius, m_e^* is the effective mass of the electron, m_h^*, is the effective mass of a hole, m_o is the free electron mass, e is the charge on an electron, ε_o is the permittivity of free space, and ε is the relative permittivity.

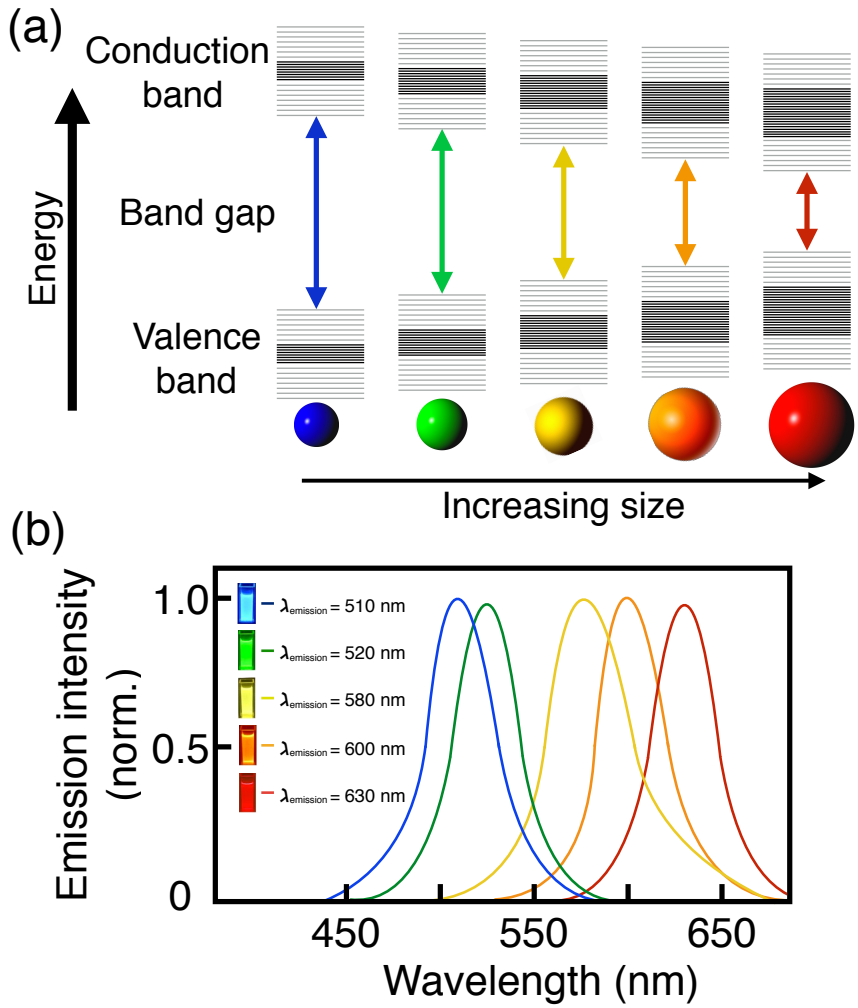

Figure 2.7: (a) Splitting of energy levels in quantum dots due to the quantum confinement effect, semiconductor band gap increases with decrease in size of the nanoparticles. (b) Emission spectra of CdSe/ZnS QDs.

In the equation 2.13, the first term defines the bandgap of the bulk material, the second term is quantum energy due to localization, the third term is the Coulomb attraction between the electron and the hole, and the last part represents the polarization terms. The equation clearly shows the dependence of the bandgap on the inverse square of the radius of the quantum dot. Thus, as the decrease in the quantum dot size, the energy of the particle increases. This cause the QDs to absorb light at shorter wavelengths as shown in Figure 2.8. The figure shows absorption spectra of CdSe, which has the size range from size 1.7 nm to

15 nm along with sharp interband transitions.The graph illustrates the bandgap increases as represented by the blue shift of the absorption curve when the decrease in size of quantum dots. Precisely, the size variation of CdSe quantum dots can tune the bandgap from 3.1 eV to 1.8 eV which corresponds to a shift in wavelength from 400 nm to 700 nm. Therefore, tuning size-dependent bandgap of QDs brings the benefits of fluorescence emission tunability. The general emission tuning range is known from the near ultraviolet into the near-infrared. This optical property of colloidal QDs makes them unique and attractive for a variety of photonic applications.

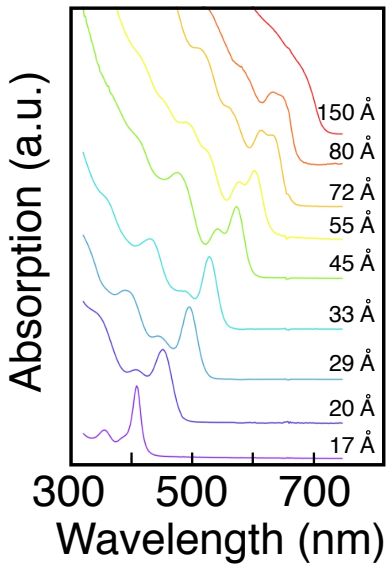

Figure 2.8: Emission spectra of CdSe/ZnS quantum dots (QDs). The QDs were excited at 350 nm. (Reprinted with permission from the reference [43] with permission from the American Association for the Advancement of Science.)

2.8 Electrical properties of colloidal quantum dots

This section discusses the electrical transport and transfer of charges. Because of strong confinement in nanocrystals, electron transport has limitation of interparticle transfer within a single particle [44]. This charge transport mechanism is different compared with traditional semiconductor transport. The transport mechanism of the colloidal QDs is the charge transport in molecular systems where transport occurs between nanocrystals resulting in hopping between localized states. Electron transfer between localized states from Marcus theory [45] can be used for understanding the charge transfer between two nanocrystals.

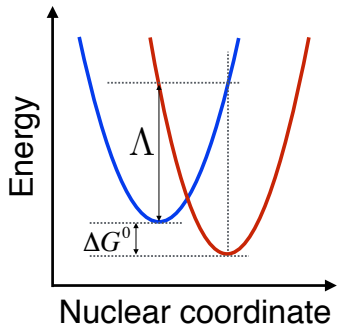

Figure 2.9: Energy as a function of nuclear coordinate for initial and final states.

The two parabolas in Figure 2.9 demonstrate the initial and the final states, which have different nuclear coordinates. This difference caused by variation in the charge of the atoms involved during an electron transfer. The electron transfer happens at the intersection of the parabolas. This is because the nuclear coordinates are not able to change during the electron transfer process from initial to final state [44]. The electron transfer rate constant, k_{et} as derived by Marcus et al. [46] is shown as

$$k_{et} = \left(\frac{2\pi}{\hbar}\right)|M_{12}|^2\left(4\pi^2\Lambda k_B T\right)^{-\frac{1}{2}} e^{-\frac{\triangle E}{k_B T}} \tag{2.14}$$

where

$$\triangle E = \frac{\left(\triangle G^0 - \Lambda\right)^2}{4\Lambda} \tag{2.15}$$

$\triangle G^0$ is the free energy change between the initial and the final state, M_{12} is the electronic coupling matrix element between initial and final states on resonance, $\triangle E$ is the energy of the electron transfer, Λ is the total reorganization energy, k_B is the Boltzmann constant, and T_a is the absolute temperature. The total reorganization energy, Λ is the amount of energy required to force the final state to have the same nuclear configuration as the initial state without letting the electron transfer. In this case, Λ is the sum of the energies due to internal vibrations Λ_i and changes in the configuration of the dielectric matrix surrounding the nanocrystals Λ_o, such as $\Lambda = \Lambda_i + \Lambda_o$.

Additionally, the dielectric contribution, Λ_o, can be approximate by using a dielectric continuum model while the transfer between two nanocrystal spheres:

$$\Lambda_o = \frac{e^2}{4\pi\varepsilon_0}\left(\frac{1}{2a_1} + \frac{1}{2a_2} - \frac{1}{d}\right)\left(\frac{1}{\varepsilon_{OP}} - \frac{1}{\varepsilon_S}\right) \tag{2.16}$$

where a_1 and a_2 are the radius of the two nanocrystals, d is the distance of separation between two nanocrystals measured from the center, and ε_{OP} and ε_S are the optical and

static dielectric constants of the surrounding insulating matrix respectively. Analysis of electron transfer dynamics and measurement of the luminescence spectrum are used the dynamics of electron transport and transfer in nanocrystals. Thus, the understanding of the dynamics is fundamentally essential for designing nanocrystal-related optoelectronic devices.

2.9 Fluorescence intensity of colloidal quantum dots

Compared with the most of the organic dyes, QDs show generally larger differences between the excitation and emission peak. In general, the fluorescence emission spectra of QDs are relatively narrow and can show different colors by varying the sizes. Thus, the spectroscopy detection can monitor the emission intensity signals at specific wavelength, which makes the fluorescence recognition easier [47]. According to the study [48], the fluorescence intensity of QDs is 20 times and stability of QDs is above 100 times higher than the well-known organic fluorescent dye, Rhodamine 6G. Simultaneously, QDs have high capacity to resist photobleaching [48]. The photobleaching is a phenomenon that decreases the fluorescence intensity due to optical excitation, which I will discuss more details about this effect in the Chapter 3. Generally, the photobleaching rate of organic fluorescent dyes is very fast, resulting in a loss of fluorescence. On the other hand, the photobleaching rate of QDs is extremely lower. For example, the fluorescence intensity produced by CdSe/ZnS colloidal QDs hardly diminished at 500 mW with a 488 nm excitation beam for 14 hours [49]. Hence, colloidal QDs have used for labeling cells and organs and have observed the emission for a long time since the QDs obtains the high photochemical stability [50, 51]. This proves that colloidal QDs are a powerful tool for imaging of test specimens with long-term light exposure condition.

2.10 Thermotropic liquid crystal

Liquid crystal (LC) are materials showing properties that are intermediate between crystal and liquids [52]. LC molecules tend to align along a common axis, called the nematic director. LC materials are characterized by their nematic-isotropic phase transition or below the transition temperature, which we can observe a liquid crystalline phase [53]. Below the isotropic temperature, the LC material has several distinct liquid crystalline phases. These intermediate phases are produced by temperature changes and such LC is known as thermotropic LC [54].

The vast majority of thermotropic LC is composed of rod-like molecules (Figure 2.10). Due to the molecular arrangement and ordering of LC molecules, thermotropic LC at temperature below isotropic and above crystalline phase is classified as nematic, smectic or

cholesteric [55, 56]. Figure 2.11 demonstrates the molecular arrangement of LC for the different phases and the sequence of phase changes with increasing temperature.

Figure 2.10: Anisotropic (rod-like) shape of a typical liquid crystal molecule. The molecule shown here is 4-cyano -4'- Pentylcyanobiphenyl, commonly known as 5CB, which exists in the nematic phase at room temperature.

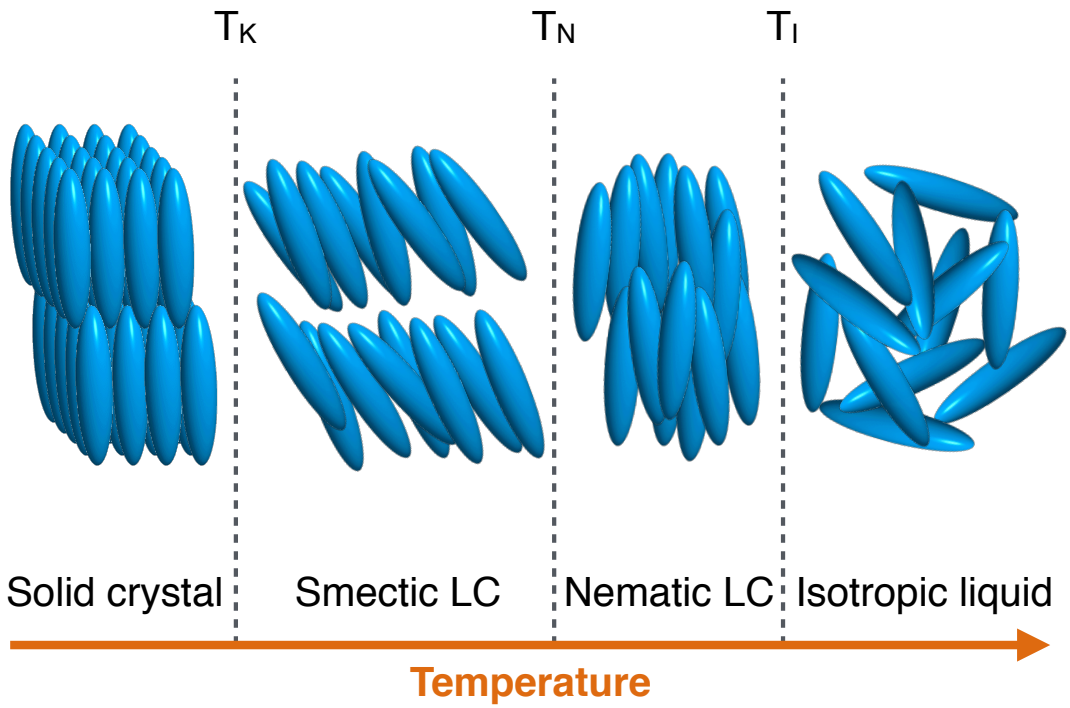

Figure 2.11: Phase sequence of LC materials with increasing temperature. T_K represents disordering temperature of the crystalline state, T_N is the nematic transition temperature and T_I is the isotropic transition temperature.

Smectic LC have an additional degree of translation order, which does not present in nematic phase. Besides existing extra orientation order, smectic LC molecules tend to arrange themselves in planes or layers.

The cholestric LC, which is known as chiral nematic phase, is composed of optically active molecules [57, 58]. Result in the structure, cholestric LC has a twist along its helical axis. When we focus on viewing along the layer direction, the structure show a very thin nematic-like layers with the nematic director of each layer twisted with respect to above and below LC layers. Figure 2.12 illustrates the layers with the arrangement and ordering of molecules in cholestric LC.

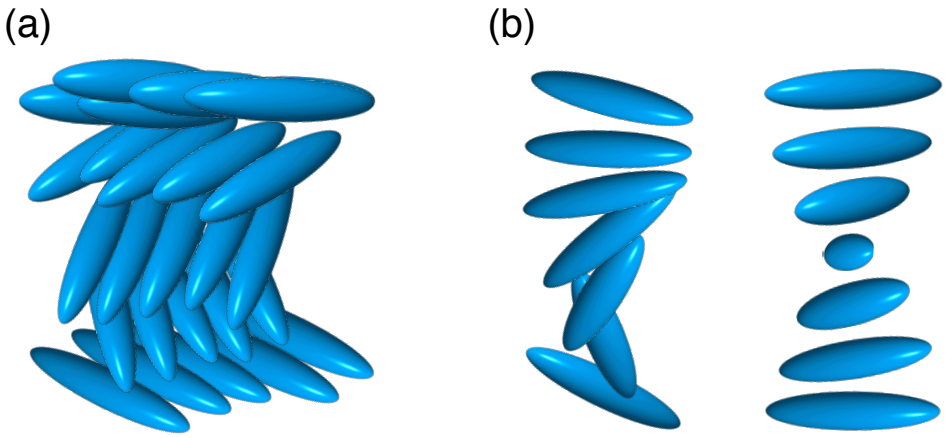

Figure 2.12: (a) The structure of cholesteric liquid crystal. The twisting nematic director from layer to layer can be perceived. (b) Typical molecular arrangement of the cholesteric LC observed by two different angles. The different angle observation show the molecular arrangement of cholesteric LC is chiral.

A nematic LC has a high degree of long range orientational order of the molecules, but no long-range translation (positional) order. Hence, the LC molecules are spontaneously oriented with their long axes approximately parallel to each other. The preferred direction, the nematic director, is usually different from region to region in the medium, but they are tend to align the same direction and are strongly birefringent. The nematic director demonstrates the direction of the preferred orientation of LC molecules (Figure 2.13). The orientation order can be expressed as a parameter S, which indicates the degree of orientational order of LCs [59]. The order parameter S of the LC phase is given by:

$$S = \frac{1}{2}\left\langle 3cos^2\theta - 1 \right\rangle \tag{2.17}$$

where θ is the angle between the long axis of an individual LC molecules and the nematic director, **n**, and the angular brackets represents an average. For a perfectly parallel alignment, the order parameter show the value $S = 1$, white for totally random orientation, $S = 0$. In nematic LC phase, the value of the order parameter, S, for most LC are generally in the range between 0.4 and 0.65 at low temperature [60].

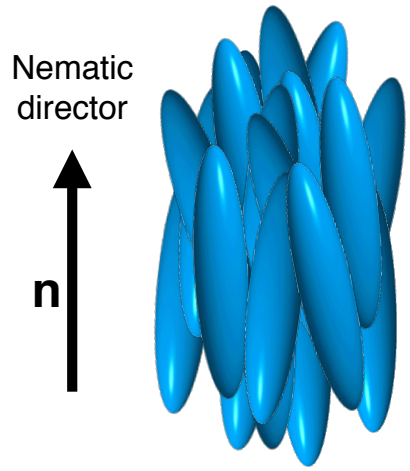

Figure 2.13: Schematic showing the arbitrary orientation of an LC molecule with respect to the average molecular orientation (nematic director, **n**).

2.11 Physical property of liquid crystals

The configuration of the nematic director is determined by minimizing the total free energy. The two most important terms in the total free energy are the elastic energy. This is because the anchoring condition between the surface and the LC molecules is very strong. The elastic energy is closely related to three specific deformations which exist in all liquid crystals, known as the splay, twist, and bend deformations. Schematic of these deformations is shown in Figure 2.14 and each deformation have an associated elastic constant and free energy contribution.

The free energies for splay (F_S), twist (F_T), and bend (F_B) deformations are corresponding to the unit vector of nematic director, $\hat{\mathbf{n}}$ [61]:

$$F_S = \frac{K_1\big(\bigtriangledown \cdot \hat{\mathbf{n}}\big)^2}{2} \tag{2.18}$$

$$F_T = \frac{K_2\big(\hat{\mathbf{n}} \cdot \bigtriangledown \times \hat{\mathbf{n}}\big)^2}{2} \tag{2.19}$$

$$F_B = \frac{K_3|\hat{\mathbf{n}} \times \bigtriangledown \times \hat{\mathbf{n}}|^2}{2} \tag{2.20}$$

where K_1, K_2 and K_3 are the Frank elastic constants which relate to the splay, twist and bend deformations respectively.

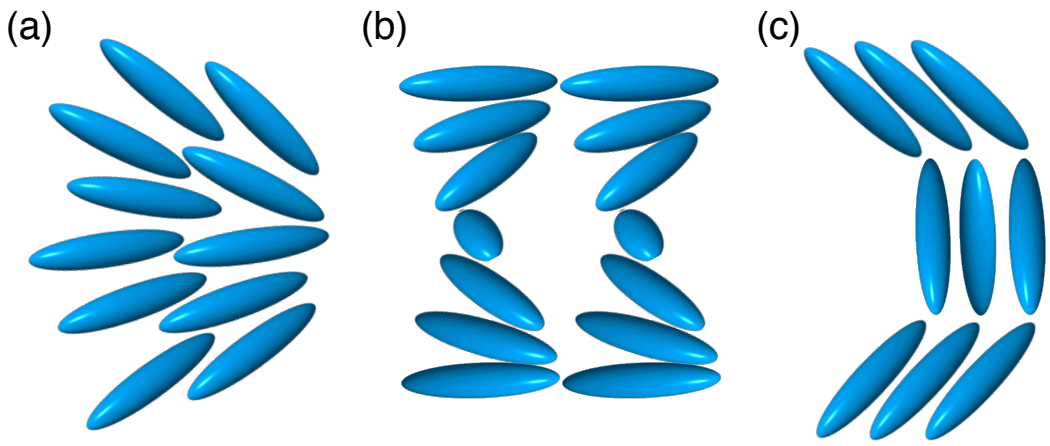

Figure 2.14: Elastic deformations in nematic liquid crystal: (a) splay, (b) twist, and (c) bend.

The nematic director is a unit vector collinear to the average direction and is related the azimuthal θ and polar angles ϕ such as

$$\hat{\mathbf{n}} = \begin{pmatrix} cos\theta cos\phi \\ cos\theta sin\phi \\ sin\theta \end{pmatrix} \tag{2.21}$$

The elastic energy density in the Frank-Oseen form of the system [61] is given by the sum of equation 2.18-2.20.

$$F = F_S + F_T + F_B = \frac{K_1\big(\bigtriangledown \cdot \hat{\mathbf{n}}\big)^2}{2} + \frac{K_2\big(\hat{\mathbf{n}} \cdot \bigtriangledown \times \hat{\mathbf{n}}\big)^2}{2} + \frac{K_3|\hat{\mathbf{n}} \times \bigtriangledown \times \hat{\mathbf{n}}|^2}{2} \tag{2.22}$$

This expression allows the nematic director orientation within a sample to be found by finding the values of θ and ϕ that minimize F. For most nematic liquid crystal $K_3 > K_1 > K_2$, while nematic 4-cyano-4'-pentylbiphenyl (5CB) has different relationship, such as K_1 = K_2 = K_3 = $K \approx 6 \times 10^{-12}$ N [62]. Under the one constant approximation, the Frank-Oseen free energy expression (equation 2.22) reduces to:

$$F = \frac{K}{2}\left[\big(\bigtriangledown \cdot \hat{\mathbf{n}}\big)^2 + \big(\bigtriangledown \times \hat{\mathbf{n}}\big)^2\right] \tag{2.23}$$

In our case, liquid crystals are usually put between two parallel glass slides, called as liquid crystal cell. To have uniform director field, a defect free liquid crystal cell, the nematic director orientation has to be controlled by alignment layers at the surfaces. If the

nematic director is set to be the same on both boundaries, the uniform configuration, then the corresponding elastic free energy (equation 2.22) becomes the lowest. There are two main types of surface alignments: homeotropic and planar, in which cases the director is uniformly perpendicular and parallel to the surface respectively. The interaction between the alignment layer and the liquid crystal can be characterized by the anchoring strength. In most cases the planar alignment is considered to be strong anchoring condition.

2.12 Electric response of liquid crystals

LC has anisotropy of their electrical, magnetic, thermal and optical properties [63]. The anisotropy of LC can be tuned by electrical parameters. In this dissertation, the electrical tunability of LCs is employed for our optical application in Chapter 4.

The dielectric anisotropy of an LC is determined by two factors; the anisotropy of polarizability for the LC molecules and the dipole orientation effect [64]. The dielectric anisotropy of LC can be written as:

$$\triangle\epsilon = \epsilon_{\parallel} - \epsilon_{\perp} \tag{2.24}$$

where $\epsilon_{\parallel}$ and $\epsilon_{\perp}$ are the dielectric permittivities in the directions parallel and perpendicular to the director of the LC respectively.

The value of dielectric anisotropy can be positive or negative. The net permanent dipole moment of the molecule has only a small angle with its long axis if the sign of the value is positive, and the angle becomes large if the sign is negative. To achieve electrical tunability with LC, understanding the behaviour of the LC under the influence of an externally applied electric field becomes necessity. When an electric field, $\overrightarrow{E}$ to LC, the LC produces a dipole moment per unit volume, refereed as the polarization $\overrightarrow{P}$.

Generally, the polarization depends linearly on the electric field at low field intensities, however the vectors, $\overrightarrow{E}$ and $\overrightarrow{P}$, can have different directions. This is because $\overrightarrow{E}$ and $\overrightarrow{P}$ are related by a tensor, $\overrightarrow{\chi}_e$, called the electric susceptibility.

$$\overrightarrow{P} = \varepsilon_0 \overrightarrow{\chi}_e \overrightarrow{E} \tag{2.25}$$

where ε_0 is the permittivity of free space. The induced polarization depends on the orientation of the LC nematic director with respect to the applied electric field direction. For an arbitrary angle of the director orientation, the applied field can be broken down into two components, parallel and perpendicular, to the director (Figure 2.15).

The induced polarization can be described as:

$$\overrightarrow{P} = \varepsilon_0\chi_{\parallel}\Big(\overrightarrow{E}\cdot\overrightarrow{\mathbf{n}}\Big)\overrightarrow{\mathbf{n}} + \varepsilon_0\chi_{\perp}\left[\overrightarrow{E} - \Big(\overrightarrow{E}\cdot\overrightarrow{\mathbf{n}}\Big)\overrightarrow{\mathbf{n}}\right] = \varepsilon_0\left[\chi_{\parallel}\overrightarrow{E} + \triangle\chi\Big(\overrightarrow{E}\cdot\overrightarrow{\mathbf{n}}\Big)\overrightarrow{\mathbf{n}}\right] \tag{2.26}$$

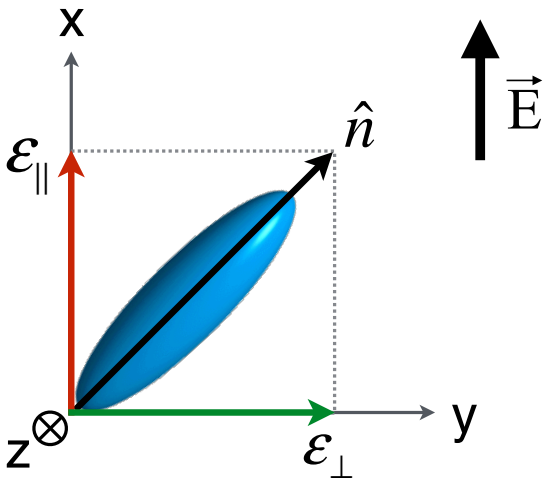

Figure 2.15: Parallel and perpendicular components of dielectric constant of the LC, with respect to an applied electric field direction.

In this case, the dielectric constants, $\varepsilon_{\parallel}$ and $\varepsilon_{\perp}$, are related to the susceptibilities, such as $\varepsilon_{\parallel} = 1 + \chi_{\parallel}$ and $\varepsilon_{\perp} = 1 + \chi_{\perp}$. Therefore, $\triangle\chi = \chi_{\parallel} - \chi_{\perp} = \varepsilon_{\parallel} - \varepsilon_{\perp} = \triangle\varepsilon$.

The approximate electric energy of the LC per unit volume can be written as:

$$\begin{aligned} F_{electric} = -\frac{1}{2}\vec{E}\cdot\vec{P} &= -\frac{1}{2}\varepsilon_0\left[\chi_{\perp}\vec{E} + \triangle\chi\left(\vec{E}\cdot\vec{\mathbf{n}}\right)\vec{\mathbf{n}}\right] \\ &= -\frac{1}{2}\varepsilon_0\chi_{\perp}E^2 - \frac{1}{2}\varepsilon_0\triangle\varepsilon\left(\vec{E}\cdot\vec{\mathbf{n}}\right)^2 \end{aligned} \tag{2.27}$$

If the LC has a positive dielectric anisotropy ($\triangle > \varepsilon_0$), the electrical energy is minimized when the LC nematic director is parallel to the applied field. Conversely, if the dielectric anisotropy is negative ($\triangle < \varepsilon_0$), then the electric energy is low when the LC molecules align orthogonal to the applied electric field.

Rotational viscosity is one of the important parameters for reorientation of LC molecules. The dynamic response of LC caused by the external applied electric field strongly depends on the rotational viscosity. For example, the elastic constants of the LC material determine the restoring torque perturbed from its equilibrium state. When an electric field is applied to reorient LC molecules, the balance between the electric and elastic torque causes the static deformation of the LC director. The deformation modes of the LC director, splay, twist and bend, was discussed in the previous session. Additionally, the LC response induced by external electric fields is relied on the interactions between the LC molecules and the forces at the surface boundaries. Reorientation of the LC molecules does not inevitably

happen as the applied field becomes more than zero. Most importantly, reorientation of LC molecules only occurs above a critical or threshold field, E_{th}. The dielectric anisotropy and the elastic constant are the parameters that find the threshold electric field for the LC.

The threshold field for LC reorientation for splay ($E_{S,th}$), twist ($E_{T,th}$), and bend ($E_{B,th}$) is given as [65, 66]:

$$E_{S,th} \approx \left(\frac{\pi}{d_T}\right)\sqrt{\frac{K_1}{\varepsilon_0 \triangle \varepsilon}} \tag{2.28}$$

$$E_{T,th} \approx \left(\frac{\pi}{d_T}\right)\sqrt{\frac{K_2}{\varepsilon_0 \triangle \varepsilon}} \tag{2.29}$$

$$E_{B,th} \approx \left(\frac{\pi}{d_T}\right)\sqrt{\frac{K_3}{\varepsilon_0 \triangle \varepsilon}} \tag{2.30}$$

where d_T is an LC layer of thickness, K_1, K_2 and K_3 are the Frank elastic constants which relate to the splay, twist and bend deformations respectively. This reorientation of the nematic director under the influence of an electric field is known as the Freedericksz transition, and these threshold fields are required for the reorientation of LC molecules. The Freedericksz transition threshold of 4-cyano-4'pentylbiphenyl, our experimental material, in nematic phase is 83 (mW/mm^2) [67].

2.13 Optical anisotropy

The optical anisotropy in nematic LC is expressed by the distinct values of the refractive indices along the optical axis, $n_\parallel$, and perpendicular to it $n_\perp$. In general, most of the nematic phases are optically positive, $n_\parallel > n_\perp$. Optical anisotropy can be represented as the indicatrix. The indicatrix is a ellipsoid geometric figure whose major and minor axes correspond to $n_\parallel$ and $n_\perp$ respectively. Materials becomes optically negative when $n_\parallel < n_\perp$ as shown in Figure 2.16. Moreover, most uniaxial nematic LC are characterized by one principal optical axis, making them optically uniaxial [68]. Equivalently, biaxial material have two principal axes and optically biaxial. When a light beam is transmitted at an angle ϕ relative to the optic axis, the light is split into two components: the ordinary ray (having index of refraction, n_o) and the extraordinary ray (having index of refraction, n_e), which is shown in Figure 2.16 (b). The refractive index corresponding to the ordinary and extraordinary components are related to $n_\parallel$ and $n_\perp$ through the relative angle ϕ such that:

$$n_e = \frac{n_\parallel n_\perp}{\sqrt{n_\parallel^2 cos^2\phi + n_\perp^2 sin^2\phi}} \tag{2.31}$$

$$n_o = n_\perp \tag{2.32}$$

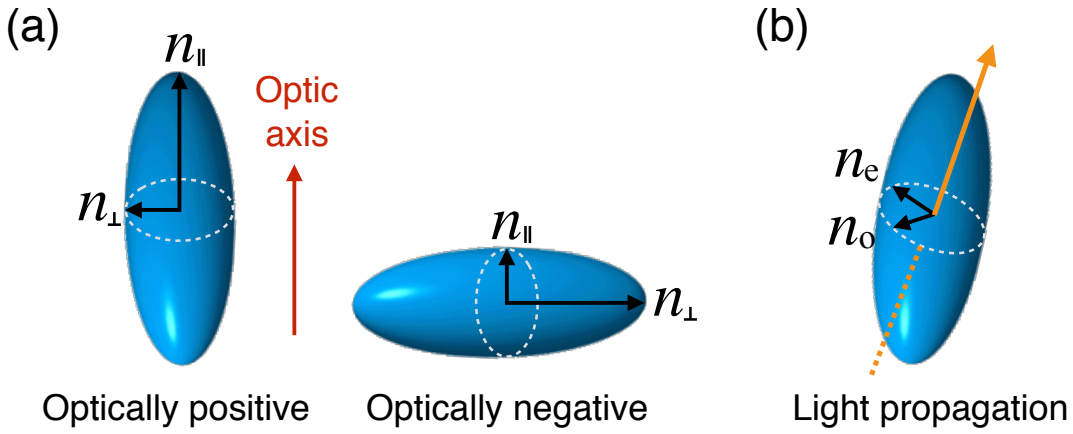

Figure 2.16: Optical anisotropy. (a) Schematic illustrating optically positive (left) and optically negative (right) samples. (b) Transmission of light (an orange allow) through an optically anisotropic medium yields an ordinary n_o and an extraordinary n_e components.

The ordinary and extraordinary rays propagate through the materials at different velocity, resulting in a phase difference, δ, within a material of optical distance d:

$$\delta = \frac{2\pi}{\lambda}(n_e - n_o)d \tag{2.33}$$

whrere λ is the vacuum wavelength of the propagating light. The parameter of the difference between the ordinary and extraordinary refractive indices is known as the optical birefringence:

$$\triangle n = n_e - n_o \tag{2.34}$$

When a linearly polarized light is passed, the linearly polarized light is converted into elliptically polarized light. Now, the elliptically polarized light can pass through a crossed polarizer, also referred as the analyzer [69]. The intensity, I, of the light comes through the analyzer is written by

$$I = I_1 sin^2(2\varphi) sin^2\left(\frac{\delta}{2}\right) \tag{2.35}$$

where I_1 is the light intensity after the first polarizer, and δ is the angle between the analyzer and the optic axis projection on the plane, φ is the polarization phase shift of the light emerging from the LC. The first term in the equation 2.35 indicates the intensity of the light transmitted through the crossed polarizers on rotating the sample, the second term represents responsible for the birefringent colors in thin nematic LC films.

Chapter 3

Experimental techniques

This chapter is devoted to explaining the basic principles of the techniques we used. In particular, I discusses the equipment, experimental procedures, and material properties used to collect the data presented within this dissertation. The descriptions of these techniques presented here are considered the normative. Any deviations from these procedures are discussed on a case-by-case basis within the relevant chapter.

3.1 Polarized light microscopy

A polarized light microscopy uses plane-polarized light and is designed to observe specimen's optically birefringent material that has two different indexes of refraction at right angles to one another. The microscopy is equipped with a polarizer placed in the light pathway before the specimen and an analyzer (a second polarizer) positioned after the objective. These two polarizers are designed to be located at right angles to each other, which is called as cross polar. A common polarized light microscopy is illustrated in Figure 3.1. The polarization direction of the first polarizer is vertical to the incident light, thus only the vertical component of the light is able to go through it. The passed light is eventually blocked by the second polarizer (analyzer) since the second polarizer is located horizontally to the passed light. The left side image in Figure 3.1 shows a birefringent (anisotropic) material placed between these two polarizers. Linearly polarized light, illustrated by a red wave, is created when non-polarized light from the illuminator passes through the bottom polarizer. The polarized light then enters a birefringent material mounted on the stage of polarized light microscopy, and the light is reflected and split into two directions, which are ordinary (blue) and extra-ordinary (red) rays. Both lights go though the second polarizer that allows only the light wave that is parallel to the second polarizer‘s transmission path way.

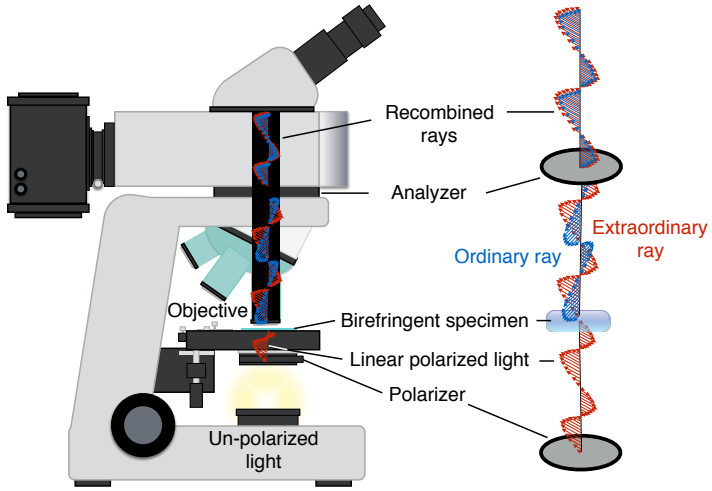

Figure 3.1: Polarized light microscopy.

3.2 Rotation effect of the polarizers for nematic liquid crystal cells

The effect of the angle between horizontal direction and polarizer transmission axis on the appearance of liquid crystal phase can be analyzed. Non-aligned nematic LC (NLC) cells made of two glass slides do not show long-range orientational order, denoted by the nematic director. Changing the nematic director makes bright or dark areas, depending on the orientation of the director compared to the crossed polarizers. To control the nematic director, alignment layer is often used. Alignment layer controls a specific pretilt angle of LC molecule, which is the angle between the alignment layer and the nematic director of LC. The role of this special pretilt angle becomes significant in liquid crystal display (LCD) such as response time, color performance, and power supply requirement for a device. In Figure 3.2 shows schematics and images of planar and homeotropic alignment LC sample under a cross-polarized mode. When the LC sample with planar alignment rotates from 0, 45, and 90 degrees, there are large variations on bright domains due to the change of wave vibrating directions (Figure 3.2 (b-d)). That is, the domain of brightness indicated as a director of the NLC (Figure 3.2 (a)). For instance, the darkest areas represent to the areas where the director is parallel with either of the polarizer (Figure 3.2 (b,d)) and the brightest areas are observed where the director is located at a 45 degree angle to both polarizers (Figure 3.2 (c)). On the other hand, homeotropically aligned LC sample (Figure 3.2 (d)) becomes non-birefringent sample since LC molecules appear to be isotropic with respect to the light traveling direction. As a result, the sample is observed as dark images in all angles under the cross-polarized microscopy (Figure 3.2 (e)).

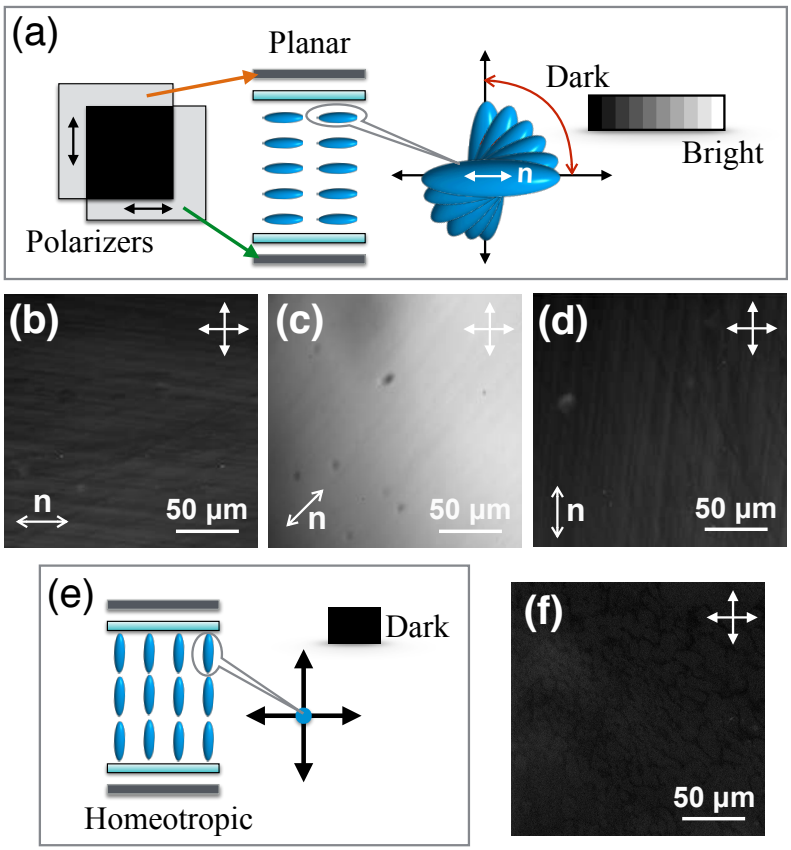

Figure 3.2: (a) Schematic presentation of a planar alignment LC cell. Wide viewing angle and high contrast ratio characteristics based on the molecular orientation of LC (top view) (right). Transmitted bright field images under crossed polarizers as the rotating stage holding planar aligned sample makes an (b) 0 degree (c) 45 degree (d) 90 degree angle with one of the polarizers. The polarizers are crossed as indicated by the white arrows on the top right hand corner. The arrow, n, demonstrates rubbing direction of the planar cell. (e) Schematic representation of nematic LC alignment in cells with homogeneous and homeotropic boundary conditions. Top view of the molecular orientation of LC (right). (f) The dark image arises from the homeotropic alignment cell and crossed polarizers.

3.3 Liquid crystal cell alignment

In general, LC applications have a certain control or a feasible technique to apply surface alignment layers for controlling a pretilt of LC molecules without applying external electric field. The main aspect in the surface alignment is the interactions between the surface and LC molecules.

3.3.1 Rubbing technique for planar alignment

Mechanical rubbing of the surface coating is the simplest method for creating physical properties of anisotropy surface. This anisotropy surface creates certain alignment for LC molecules via contact. According to the rubbing method, the surface of the glass slides is simply rubbed uni-directionally by special type of cloth. A glass slide needs to be slid on a rubbing cloth at a constant speed. Applying constant rubbing force is also an important factor for producing better LC planar alignment. Commonly, the glass slide is coated by alignment material such as polyvinyl alcohol (PVA) before carrying out the rubbing process. The LC molecules on the glass slides prefer to be oriented parallel to the rubbing direction, which is modified as planar aligned LC sample, in order to minimize the surface free energy.

3.3.2 Chemical technique for homeotropic alignment

LC alignment can be created by depositing surface coupling agents on top of the glass slide or by mixing the agents with liquid crystal material. The main mechanisms of this method are dealing with steric forces and polar interactions. The main components of surface coupling agents have two parts, where one is hydrophilic and the other is hydrophobic. Surface coupling agent gives either homeotropic or planar alignment depending on their specific properties. For example, cetyltrimethylammonium bromide (CTAB), which has some polyimides with alkyl chains, is often used for producing homeotropic alignment.

3.4 Forming nanoparticle microcapsules

Mesogen functionalized semiconductor nanoparticles, 620 nm CdSe/ZnS quantum dots (NN Lab) and 5 nm diameter gold nanoparticles (Nanopartz) were added to a nematic liquid crystal (NLC) 4-cyano-4'-pentylbiphenyl (5CB, Sigma Aldrich). The mixture was then sonicated in a 40 ^{0}C bath for several hours in an Eppendorf tube. This is allowing the NLC to remain in the isotropic phase while the solvent, chloroform or toluene, in which the nanoparticles (NPs) were suspended during functionalization and gradually evaporated from the NLC. Solvent removal was verified by measuring the nematic-to-isotropic phase-transition point using a differential scanning calorimetry (DSC). We placed a microscope LC-NP mixture slide on a 40 ^{0}C maintained hot-stage and verify the sample slide condition that has a great initial dispersion by using a microscope equipped with a CCD camera. After achieving a homogeneous dispersion, the mixture was deposited onto a microscope slide mounted on a temperature-controlled hot-stage and sandwiched with a cover slip. All slide and cover clip surfaces were pre-treated with cetyltrimetylammonium bromide (CTAB) or polyvinyl alcohol (PVA) to encourage homeotropic or planar alignment of the

NLC molecules. NP microcapsules were formed by cooling the NLC-NP mixture into the nematic phase.

3.5 Topological defects of a nematic liquid crystal around spherical objects

When particles exist in NLC media, NLC mediate elastic force between the particles [70]. LC molecules align along the particles and at the same time these molecules need to be homogeneously oriented with the LC molecules directed by their alignment layer. This conflict condition causes frustration for the LC molecules around the particles. LC molecules around the particles face their inabilities to fill the space with a uniform alignment. As a result, it causes a strong elastic distortion of the nematic LC around the particle. This distortion can be observed under a polarizing microscopy.

For example, we are often viewed two different symmetries of the surrounding NLC for normal (homeotropic) surface-anchoring conditions on the spherical shaped objects. The first one is the dipole (Figure 3.3 (a-c)) and the second is the quadrupole topological defects (Figure 3.3 (d-f)).

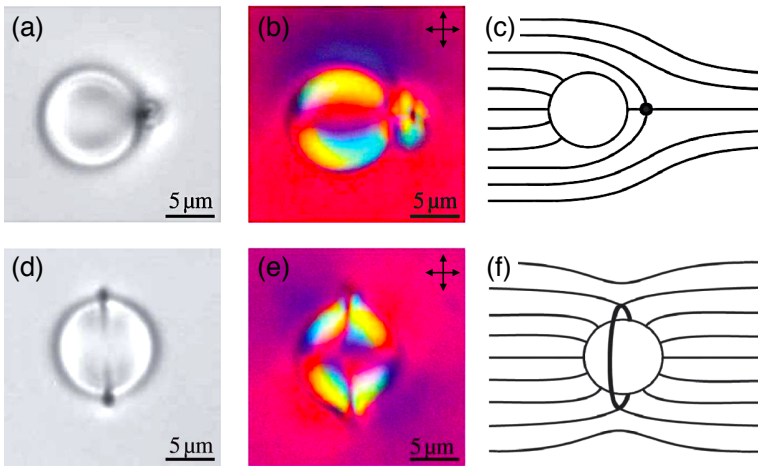

Figure 3.3: A silica microsphere image, treated so as to align the LC molecules perpendicular to its surface, appears in the form of either a dipole (a) or a quadrupole (d) without any polarizers. The small dot in (a) is the hedgehog topological defect. The ring, visible in (d), is the Saturn ring. The images in (b) and (e) are taken using crossed polarizers and the red (lambda) plate. (c,f) A schematic of the director-field distribution. (Reproduced from reference [71] with permission from the Royal Society.)

Similarly, the bipolar (Figure 3.4 (a-c)) and radial (Figure 3.4 (d-f)) configuration is observed most frequently and results from a planar (parallel) surface anchoring condition. These four different topological defects are produced around the spherical objects in NLC media based on the combination of alignment layer types, surface anchoring conditions, and LC elastic forces. Each colloidal particle is covered with elastically distorted NLC molecules. Changing the separation between the colloidal particles induces the changing the magnitude of elastic distortion since the elastic free energy of a pair colloidal particle relies on their separation.

Additionally, the changing the magnitude of elastic distortion is influenced by temperature since the force is on thermodynamic systems. Moreover, the large elastic force values between colloidal particles in NLC were reported. For instance, 2 to 4 μm colloidal particles' potential elastic energy was 2 000 k_BT per particle [73]. Compared with the van dar Waals pair interaction in water for 2 μm particle, 1 k_BT [74], the elastic energy had 2000 times more energy. Hence, each LC molecule around spherical objects helps minimizing elastic free energy by changing their molecular orientation, which we can observe as different topological defect patterns.

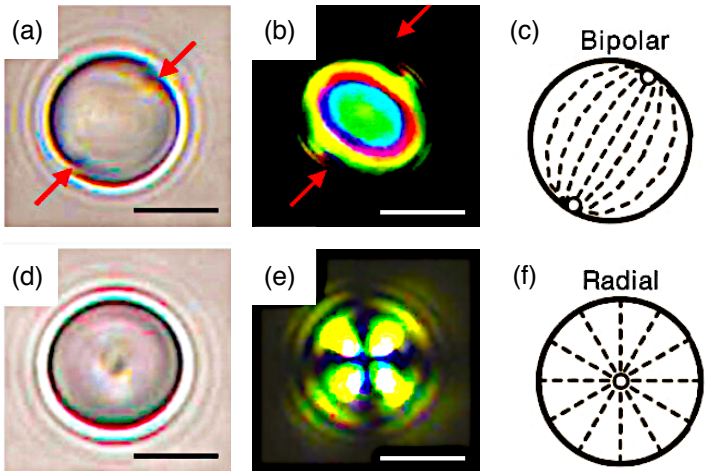

Figure 3.4: Bright-field (a,d) and cross-polarized (b,e) images of an LC droplet in water. The red arrows indicate boojums at the surface of the droplet. (c) Schematic illustration of the bipolar configuration of the LC droplet corresponding to (a) and (b). (f) Schematic demonstration of the radial configuration of the LC droplet corresponding to (d) and (e). (Reproduced from reference [72] with permission from the American Association for the Advancement of Science.)

3.6 Fluorescence microscopy

Fluorescent microscopy is often used to visualize specific characteristics of small specimens such as micron-sized crystals and microbes. These specimens need to fluoresce, absorbing incident beam and re-radiating light, when we image of them. Special dyes called fluorophores, which contain a fluorescent chemical compound, can label tissue components like bacteria, microtubules, antibody and even DNA. When these fluorescently labeled specimens are excited by specific wavelengths of light, they emit light at a longer wavelength. Fluorescence microscopy has used in many different fields, such as biology, physics, material sciences, engineering, and medical sciences, since information provided by a fluorescence microscopy is not able to be produced by traditional optical microscopy. Fluorescence has helped to identify specific cells, micron-sized cellular components, even a single molecule with a high accuracy [75]. The basic principle of a fluorescence microscopy is illustrated in Figure 3.5. The incident excitation light with specific wavelength reflects from the surface of a dichroic mirror through the microscope objective, and then reaches the specimen. The specimen absorbs the incident light, and the fluorescence emission from the specimen passes back through the dichroic mirror, and incident light or white light is filtered this time by an emission filter, which blocks unwanted wavelengths, before reaching the detector.

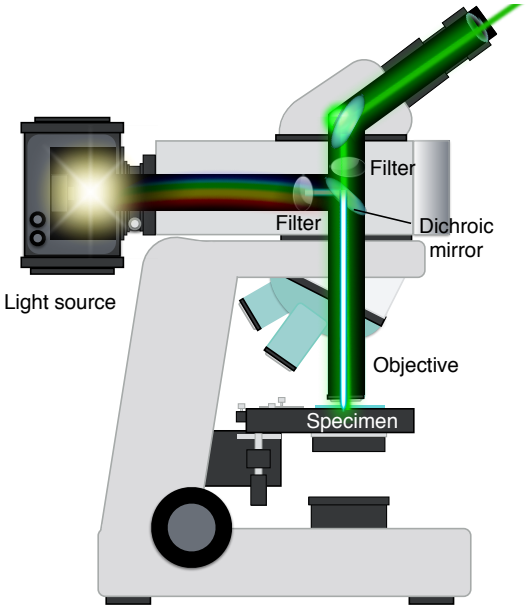

Figure 3.5: Fluorescence microscopy. Light pathways for typical upright fluorescence microscopes.

When we use a fluorescence microscopy, we need to aware of its disadvantage. The microscopes has excitation light that can be much brighter than the emission light, sometimes by the order of a hundred thousand times. This means that the excitation light may interfere with the emission light when the fluorescent specimen are located at extremely dark background, thus our observation of the sample objects will be affected. Additionally, the strong excitation light may cause photobleaching, which is defined as the irreversible decomposition of the fluorescent molecules due to their interaction with molecular oxygen before emission [75]. To minimize these disadvantages, we need to check the power of the incident light or adjust exposure time length before we image our samples.

3.7 Confocal microscopy

Confocal microscopy is based on the principle that all light has to pass through a pinhole before it reaches the detector. The idea behind this obstacle in the detection path was to create a small and very well defined detection volume. Confocal microscopy, developed by Marvin Minsky in 1955, overcomes some of the limitations that fluorescence microscopy has. The important advantages of this type of microscopy are the elimination of out-of-focus point illumination, and the ability to create observations from thick specimens. The confocal microscopy images are very high quality, fine detail, and more contrast than in regular microscope methods. Also, confocal microscopy can be used for in vivo imaging, and the images can be reconstructed to a virtual 3D image of the specimen [76]. The principal light pathway applied in most modern confocal microscopes used for fluorescence imaging is presented in Figure 3.6. The green lines represent the light path of the excitation light emitted by a laser excitation source. After passing through the pinhole aperture, the excitation ray is reflected by the dichroic mirror and then it is focused though the microscope objective at the desired focal plane (gray lines) in the specimen. The emission light represented by the red lines is collected by the same objective lens, and then go through the second pinhole aperture. The second pinhole allows only for the emission light from the desired focal point. In fluorescence microscopy, an emission area from the specimen is illuminated, which means there are no guaranteed that only the region of interest is focus when you image [77]. For instance, fluorescence microscopy can cause problems in the analysis of specimens that have a thickness about 2 μm or more [78]. The confocal microscopy provides a solution to this issue by excluding the out-of-focus emission light that exists in fluorescently labeled thick samples. A laser beam is focused by the objective lens to produce a spot on the sample and create the images. The images produced from scanning the specimen with a focused beam of light are called optical sections. Using this technique provides that the microscope can collect more images such as images of living specimens with 3D data. The image data demonstrates the huge advantages for living tissues or any biological specimens.

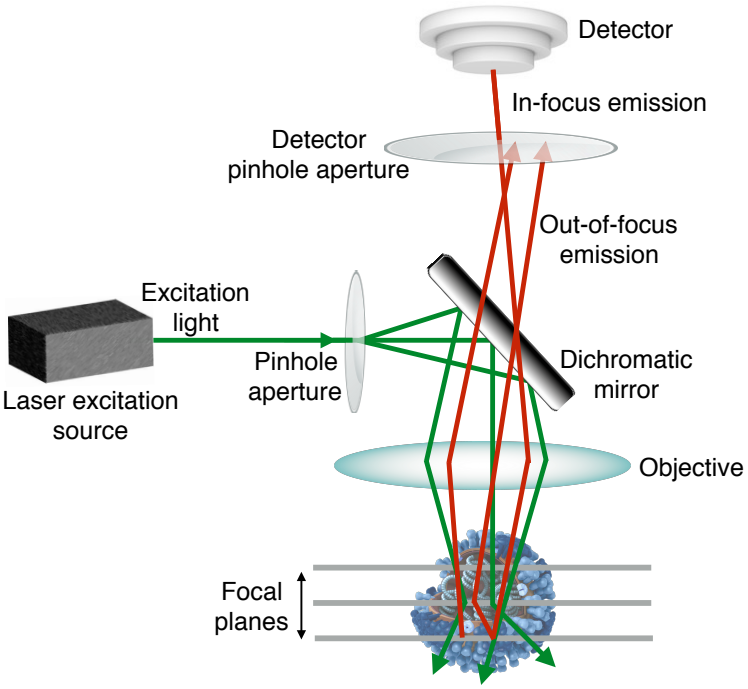

Figure 3.6: Principal light pathways in confocal microscopy.

3.8 Fluorescent molecules and quantum dots

Fluorescent molecules, such as fluorophores or dyes, have distinct excitation, absorption, and emission spectra [79]. Absorption spectra indicate the amount of absorption of incident light as a function of wavelength while emission spectra represents the fluorescence intensity measured as a function of wavelength. Excitation spectrum is the fluorescence detection wavelength. A fluorescent molecule can exist in a variety of energetic states, which are determined by its electron configurations and vibrational agitation. If a photon with sufficient energy is absorbed by a fluorescent molecule, the energy level of the molecule moves from its ground state to an excited state (Figure 3.7). Fluorescence occurs when the excited molecule returns to the ground state by releasing its energy through emission of a photon. Since some of the energy gained during excitation is converted to heat, the emitted photon has a lower energy than the absorbed one [79]. Therefore, the emission wavelength of any fluorescence molecule is longer than its excitation wavelength and, thus we can observe a different color. The difference between wavelengths of the emission and excitation is called the Stokes shift. Figure 3.8 shows the absorption and emission spectra of fluorescence dye, Lumogen F Red 300.

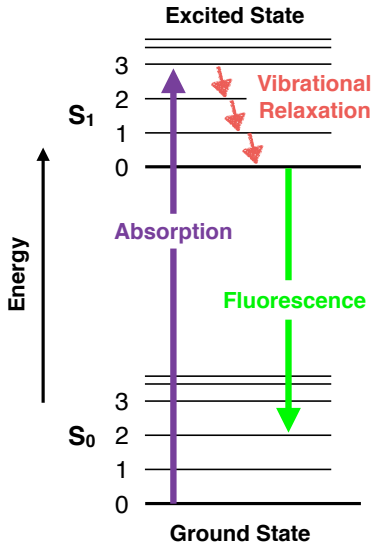

Figure 3.7: The Jabloński energy diagram of fluorescence. The diagram illustrates the photon absorption of short wavelength photons results in a longer wavelength fluorescence emission.

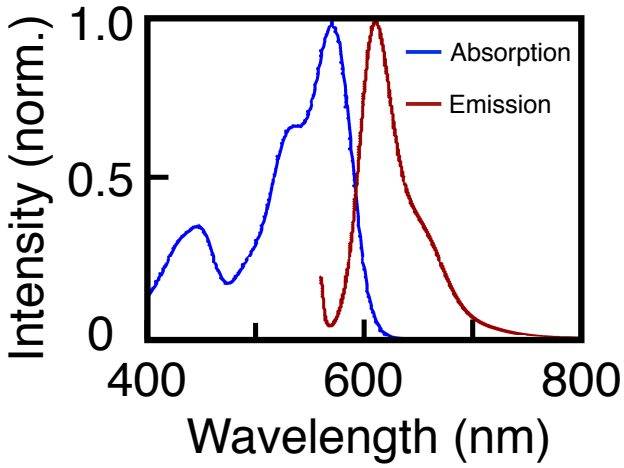

Figure 3.8: Spectral properties of the Lumen F Red 300 fluorescence dye: The absorption (blue) and emission spectra (red) of the dye. Clearly, visible is the red shifted emission peak in comparison to the excitation for each fluorophore, due to the loss of energy during internal conversion (Stokes Shift).

Emission peak is red shifted due to the loss of energy during vibrational relaxation, Stokes-Shift, makes fluorescence techniques unique, such as excitation light can be effectively suppressed since their emitted light can be separated from the excitation light by correct filters without significantly interfering with our desired emission signal. Most importantly, the property of fluorescence molecules is that these molecules are more chemically reactive in their excited state. Depending on the environmental condition, they can undergo reactions that lead to permanent damages, by which the molecules lose their capabilities to fluoresce or develop into nonabsorbent for their excitation wavelength. Precisely, fluorescence molecules in the excited state may undergo chemical reactions between fluorescent molecules and molecular oxygen, called photodynamic, permanently destroy fluorescence and yield a free radical oxygen species that can chemically modify into other molecules [80, 81]. The damages are called photobleaching, which reduce or lose the total intensity of fluorescence emission light. As a result, the observation time of a fluorescence-labeled specimen will be limited. Many factors, such as the sever molecular environment and the high intensity of excitation light cause photodynamic reaction and lead into photobleaching [82]. Figure 3.9, which illustrates a series of digital images captured at different time points for a multiply-stained C2C12 myoblasts cells and fluorescence dye, Lumogen F Red 300.

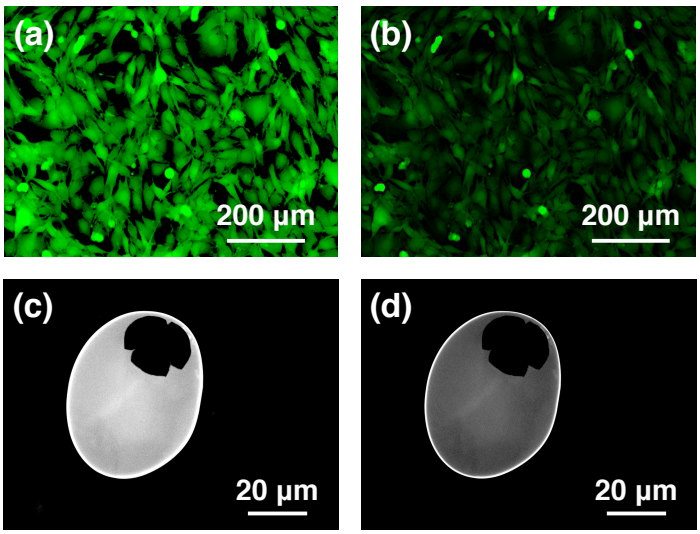

Figure 3.9: (a,b) C2C12 cells (immortalized murine myoblast cells) were fixed and labeled with green fluorescent protein (GFP). Image (a) shows the initial intensity of the fluorophore, while image (b) shows the photobleaching that occurs after 3 minutes of constant illumination. Similarly, (c,d) Lumogen F Red 300 fluorescence dye mixed with nematic liquid crystal. Image (c) illustrates the initial intensity of the dye. A photobleached image (d) was taken after 20 minutes of constant illumination.

Photobleaching can be reduced by limiting the exposure time of fluorescence molecules to illumination or by lowering the excitation energy. However, these techniques also reduce the measurable fluorescence signal. In many cases, solutions of fluorescence molecule or fluorophore-labeled cell suspensions can be deoxygenated, but this is not feasible for living cells [83]. Perhaps the best protection against photobleaching is to limit exposure of the fluorochrome to intense illumination, such as using neutral density filters or commercially available anti-fade reagents. Comparing with fluorophores like green fluorescent protein (GFP) or fluorescence dyes, quantum dot (QD) nanoparticles, composed of a core nanometer-sized semiconductor crystal, have excellent photo stability [84]. Their main advantages are their broader absorption and narrower emission spectra (Figure 3.10), resulting in brighter fluorescence. Figure 3.11 shows emission intensity of QDs, used a photoluminescence measurement technique, before and after applying a 532 nm Ti:Sapphire laser beam (Coherent Mira 900-D) at 1 mW on the QDs sample. The emission intensity relatively stayed the same as before 60 minutes laser beam exposure.

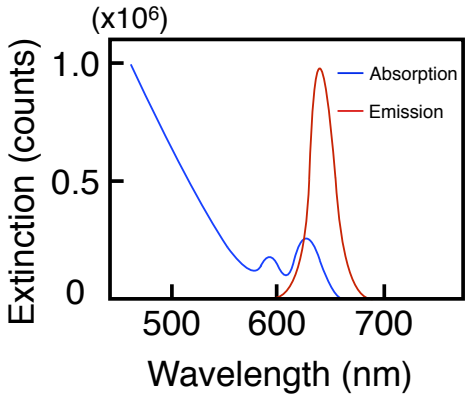

Figure 3.10: Spectral properties of CdSe ZnS QDs. The blue line represents absorption, and the red line demonstrates emission spectra.

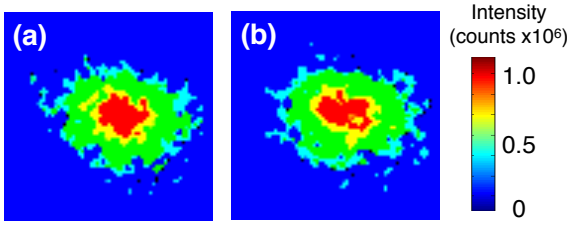

Figure 3.11: Color-maps illustrates the intensity of drop-cast QDs on the glass slide. (a) The map shows the initial intensity of the QDs emission, while the map (b) demonstrates after 60 minutes of constant illumination.

3.9 Ultraviolet-Visible spectroscopy for characterization of metal nanoparticles

Ultraviolet-Visible (UV/Visible) spectroscopy is a technique for quantifying the extinction of light, which is defined as the sum of absorbed and scattered light. Our sample was placed between a light source and a photodetector, and the intensity of incident light was measured before and after passing through the sample. Absorbance, A, is generated as a ratio of transmitted light (I_{out}) to incident light (I_{in}) by the equation:

$$A = log\frac{I_{in}}{I_{out}} \tag{3.1}$$

Therefore, the instrument must be baselined before acquisition to remove any background absorbance arising from such as an empty cuvette. Our data was plotted as extinction as a function of wavelength and the plot showed our sample's wavelength dependent characteristics based on their extinction spectrum.

NPs have optical properties that are depended on size, shape, concentration, and refractive index near the NP surface [85]. The optical properties make UV/Visible spectroscopy a useful tool for identifying and characterizing materials. In our study, we used AuNPs. AuNPs have a unique optical feature referred to as LSPR. As I mentioned in the Chapter 2, LSPR is the collective oscillation of electrons in the conduction band of AuNPs in resonance with a specific wavelength of incident light. LSPR of AuNPs results in a strong absorbance band in the visible region and the absorbance was measured by UV/Visible spectroscopy. Additionally, UV/Visible measurements were used to evaluate the functionalization of AuNPs and AuNP-LC mixture solution. Upon binding of ligands to the AuNP surface or adding AuNPs into liquid crystal solution, the LSPR spectrum red-shifted by a few nanometers. This red-shift was a result of an increase in the local refractive index.

3.10 Ultraviolet-Visible spectrophotometer for characterization of Escherichia coli suspensions

A spectrophotometer has a light source that creates specific wavelengths. The light passes through the cuvette, is absorbed by the material in the cuvette, and is read by a detector. In a bacteria suspension, the light scatters and the amount of light reached the detector is further reduced by the scattering effect (Figure 3.12). This decrease in light reaching the detector creates the illusion of an increase in sample absorbance. Generally, the wavelength of the spectrophotometer is set to the specific wavelength of sample absorbance. For instance, a bacterium usually absorbs light at a wavelength of 600 nm, and the amount of the light absorption is referred to as the optical density (OD). There are several different types of

spectrophotometers available. We used a UV/Visible spectrophotometer to measure the concentration of Escherichia coli bacteria by measuring the sample absorption of light. We selected the UV/Visible spectrophotometer method because the method is simple and fast.

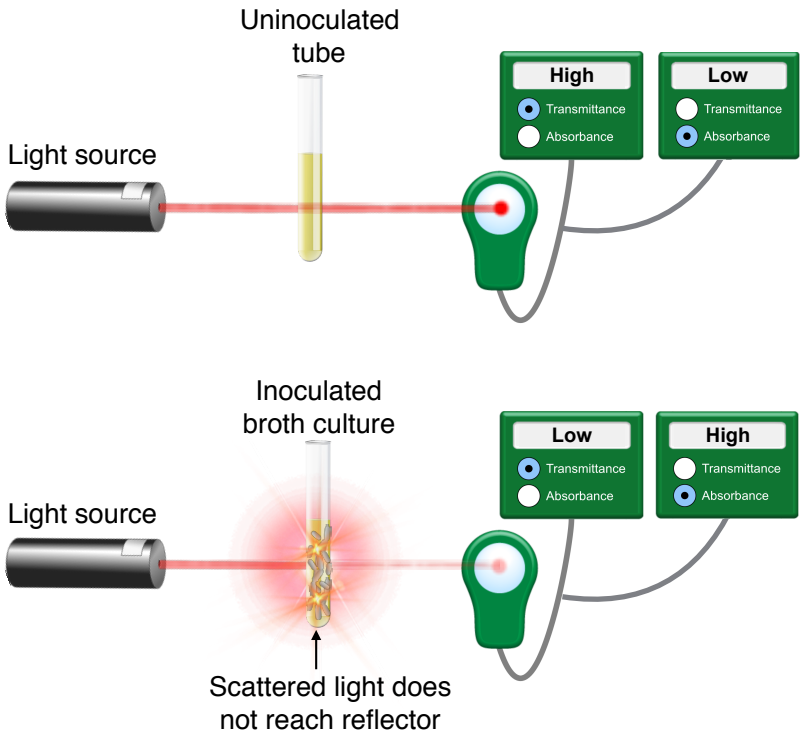

Figure 3.12: Light is scattered by bacteria in the media. A detector measures the intensity of transmitted light and the relationship between transmitted light intensity and bacteria concentration can then be illustrated.

Monitoring bacterial growth carefully and harvesting a culture at the right moment is the most important step for this experiment. Bacterial growth can be described in four stages (Figure 3.13). The first phase is lag phase, which begins when the bacteria is added into the host media. During this phase, the population growth rate of the bacteria is slow as the bacteria acclimate to the new environment. The second phase is the exponential (log) phase. During the exponential phase, bacteria are reproducing at their maximum rate. The third phase is the saturation or stationary phase. The growth rate of the bacteria slows down significantly during this phase due to the depletion of nutrients and the accumulation of waste products. The final phase is the decline phase. In this phase, the nutrients run out and the bacteria die. Hence, the amount of light absorbed by the bacterial culture behaves differently at each phase. We used SpectraMax Plus UV/Visible spectrophotometer

(Molecular Devices) at wavelength of 600 nm for measuring bacterial concentration at lag and exponential phases. The harvesting of all our cultures was during the early log phase of cell growth and these cultures were introduced in the new host media just before our measurements. We harvested the bacteria during the exponential phase since the bacteria were at their peak rate of growth.

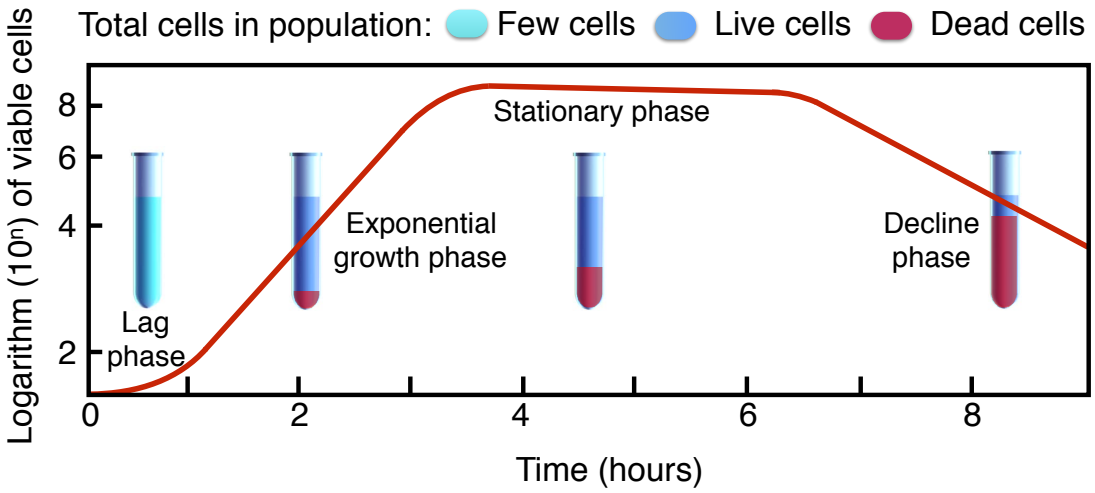

Figure 3.13: Bacterial growth curve. When bacteria are grown in a closed system, the population of cells exhibits the growth dynamics; cells initially adjust to the new medium, (1) lag phase, until they can start dividing regularly by the process of binary fission, (2) exponential phase. When their growth becomes limited, the cells stop dividing, (3) stationary phase, until eventually they show loss of viability, (4) decline phase.

3.11 Small angle X-ray scattering

X-rays are electromagnetic radiation, and they have a wavelength range from 0.01 to 10 nm. The wavelength of X-rays are comparable to the size of nanoparticles, thus they can be useful for probing structural arrangement of nanoparticles [86]. X-rays mainly interact with electrons in nanoparticles. When X-rays collide with electrons, some of the photons from the incident beam bounce away from their original light traveling pathway. If the wavelength of these scattered X-rays does not change during this collision process, elastic scattering, momentum is only transferred (not energy transferred) to the system, is created. These are the X-rays measured in our small angle X-ray scattering measurement, as the scattered X-rays transferred the information about the electron distribution in our material. If the nanoparticles are arranged in order periodically, the scattered wave then shows sharp

interface peaks with the some symmetry. Oppositely, if the nanoparticles are arranged randomly, the scattered wave produces broad symmetrical peaks as in the distribution of nanoparticles. Hence, measuring the scattering pattern helps us to understand the distribution of the nanoparticle arrangements in our material. X-ray scattered from nanoparticles creates a diffracted beam, and the beam behavior can be explained by using the Bragg equation that defines the angle of diffraction θ of radiation of wavelength λ for a separation of particle distance d:

$$m\lambda = 2d\sin\theta \tag{3.2}$$

where m is the order of diffraction, λ represents the wavelength of X-ray, and θ signifies the X-ray scattering angle. Similarly, the behavior of the scattered wave can be explained as following. If a nanoparticle at a position vector $\vec{R}$ the wave is scattered in the direction of wave vector. In addition, $\vec{k_s}$ is phase shifted by $\vec{q} \cdot \vec{R}$ with respect to the incident wave (figure 3.14). In this case, $\vec{q}$ is the scattering vector and related to the scattering angle 2 θ via

$$\vec{q} = \vec{k_s} - \vec{k_o} \tag{3.3}$$

and the magnitude of $\vec{q}$ is given by the cosine rule:

$$\vec{q}^{\,2} = \vec{k_o}^{\,2} - \vec{k_s}^{\,2} - 2\vec{k_o} \cdot \vec{k_s}\cos\theta \tag{3.4}$$

where $\vec{k_o}$ is the wave vector of magnitude $\frac{2\pi}{\lambda}$. For coherent elastic scattering condition,

$$|\vec{k_o}| = |\vec{k_s}| = \frac{2\pi n}{\lambda} \tag{3.5}$$

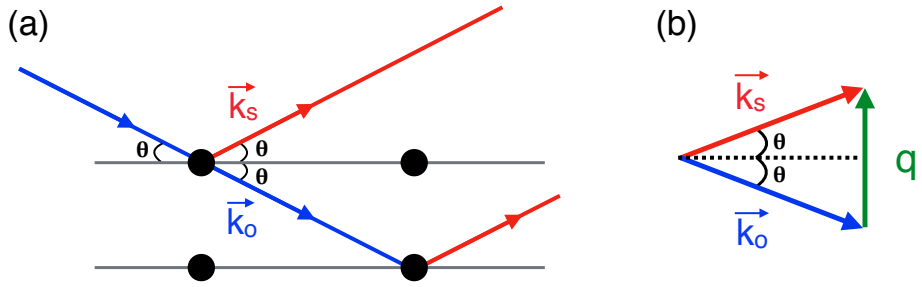

Figure 3.14: Geometrical relationship in small angle x-ray scattering. (a) The incident and scattered radiation have wave vector $\vec{k_o}$ and $\vec{k_s}$ respectively. (b) Determination of the scattering vector $\vec{q}$ = $\vec{k_o}$ - $\vec{k_s}$.

where n is the refractive index of the medium, which for our case is $n \approx 1$. Thus, $|\overrightarrow{q}|$ can be expressed by geometry as

$$|\overrightarrow{q}| = q = 2|\overrightarrow{k_o}| \sin\theta = \frac{4\pi \sin\theta}{\lambda} \tag{3.6}$$

By using equation 3.5 and 3.6, average particle-particle distance is expressed as

$$d = \frac{2\pi}{q} \tag{3.7}$$

Small angle x-ray scattering (SAXS) measurements were performed at the Stanford Synchrotron Radiation Lightsource, beamline 4 – 2. The instrument was operated at 11 keV for 1 second per exposure at three spatially different points on each 1 mm quartz capillary with a beam size of 0.3×0.1 mm at the sample.

3.12 Field emission scanning electron microscopy (FE-SEM)

In FE-SEM, high quality, low voltage images are obtained with negligible electrical charging of samples and minimized sample damages. Generally, FE-SEM is 3 to 6 times better than conventional SEM. FE-SEM, Zeiss Gemini SEM 500, is used to characterize our microstructures and surface morphology. Our microstructures are extracted from the liquid crystal host and re-dispersed in chloroform. The microstructures were pipetted on indium tin oxide (ITO) glass slides and dried the sample at 80 ^{0}C environment for 5 hours. After determining chloroform solvent is completely evaporated, SEM analysis was done at the operating voltage of 3 kV and 10kV and working distance of 5.5 mm for validating morphology of our microstructures and arrangement of the individual NPs in the microstructures. SEM images depicted in this work are acquired using the "in-lens" detector. To enhance image visibility minor brightness and contrast adjustments were performed by using Zeiss Gemini SEM software.

3.13 Cell counting

There are several techniques which can be utilized in order to measure cell growth. The first technique involves using a hemocytometer. A hemocytometer is used to count the number of cells in a given volume. Added 1 mL of 0.05 $\%$ trypsin and 0.53 mM EDTA solution (Thermo fisher scientific) to each cell-cultured well plate, and observed the cells under an optical microscopy (Nikon) until cell aspect changed to round. Aspirated the majority of the trypsin-EDTA solution and let stand for an additional 1-2 minutes, then pipetted 10

μL of the cell suspension to hemocytometer. Our hemocytometers consist of 2 chambers, each of which is divided into 9 squares with the dimension of 1 x 1 mm. A cover glass is supported 0.1 mm over these squares so that the total volume over each square is 1.0 mm^2 x 0.1 mm or 0.1 mm^3, or 10^{-4} cm^3. Since 1 cm^3 is equivalent to 1 mL, the cell concentration per mL will be the average count per square multiplied by 10^{-4}. Therefore, the cell density of our culture can be easily calculated knowing the dilution factor used to get the culture at an appropriate density for counting. Often an exclusion dye such as trypan blue or calcein-AM is used such that live cells can be differentiated from dead cells and the cell count reflects only viable cells.

3.14 Discrete dipole approximation/discrete dipole scattering simulation

In the discrete-dipole approximation (DDA), each particle is modeled as an assembly of finite cubic elements. Each of these elements is considered the sizes smaller than or comparable to the wavelength of the incident radiation. Thus, we need to evaluate only dipole interactions with the incident electric field and the induced fields in neighboring elements. These two conditions reduces the solution of the Maxwell equations to an algebraic calculation of many coupled dipole problems [87]. Each continuous assembly of the dipoles obtains a dipole moment in response to both the external electric field and the electric fields from neighboring dipoles. The electric field of an individual dipole can be expressed as [88, 89]:

$$\overrightarrow{E}_{dipole} = \frac{e^{\frac{i\omega d}{c}}}{4\pi\varepsilon_0}\Big[\frac{\omega^2}{c^2 d}(\hat{r}\times\overrightarrow{p})\times\hat{r} + (\frac{1}{d^3} - \frac{i^2\omega}{cd^2})[3(\hat{r}\cdot\overrightarrow{p})\hat{r} - \overrightarrow{p}]\Big] \tag{3.8}$$

where $\hat{r}$ is a unit vector associated with a vector $\overrightarrow{r}$ represented from the dipole to the location at which the electric field is sampled. In addition, d is the distance to the sample location, $\overrightarrow{p}$ is the vector associated with the induced dipole moment, and ω is the angular frequency of the scattered radiation. Moreover, c is the speed of light and ε_0 is the permittivity of free space. When we solve for the scattering characteristics of the continuous assembly system, each dipole has an induced dipole moment, $\overrightarrow{D}_i$, which can be illustrated as

$$\overrightarrow{D}_i = \alpha_i \overrightarrow{E_S} \tag{3.9}$$

In this case, α_i is the polarizability of the material associated with the dipole element, and $\overrightarrow{E_S}$ is the electric field at $\overrightarrow{r_i}$ that associated with the incident electric field, $\overrightarrow{E}_{incident,i}$. $\overrightarrow{E_S}$ can be expressed as a equation by using the relationship with $\overrightarrow{E}_{incident,i}$ and $\overrightarrow{E_j}$, where the electric field comes from the other dipole.

$$\overrightarrow{E_S} = \overrightarrow{E}_{incident,i} + \sum_{i=j,i\neq j} \overrightarrow{E_j} \tag{3.10}$$

$\overrightarrow{E_j}$ also can be written by using interaction matrix, M, such as

$$\overrightarrow{E_S} = \overrightarrow{E}_{incident,i} - \sum_{i=j,i\neq j}^{N} M_{ij}\overrightarrow{p_j} \tag{3.11}$$

where

$$\begin{aligned} M_{ij}\overrightarrow{p_j} = k^2 e^{ikr_{ij}} \left(\frac{\hat{p_j}\left(\overrightarrow{r_{ij}} \times (\overrightarrow{r_{ij}} \times \overrightarrow{p_j})\right)}{r_{ij}^3} \right) ... \\ ... + e^{ikr_{ij}}(1 - ikr_{ij}) \left(\frac{r_{ij}^2 \overrightarrow{p_j} - 3\hat{p_j}\left(\overrightarrow{r_{ij}}(\overrightarrow{r_{ij}} \cdot \overrightarrow{p_j})\right)}{r_{ij}^5} \right) \end{aligned} \tag{3.12}$$

where $i = 1, 2....N$, $j = 1, 2....N$ and $i \neq j$. In the equation 3.12, $\overrightarrow{r_{ij}}$ and $\overrightarrow{p_j}$ represent the positions and induced dipole moments of each element, and $\hat{p_j}$ describes the projection along the unit vector of the dipole moment $\overrightarrow{D_j}$. After the scattered electric field associated with the collection of dipoles is determined, the scattering efficiency Q_{sca} can be calculated by applying the equation:

$$Q_{sca} = \frac{\sigma_{sca}}{\pi a^2} \tag{3.13}$$

where

$$\sigma_{sca} = \frac{k}{|\overrightarrow{E}_{incident,i}|^2} \int_{dS} |\overrightarrow{E}_{scattered}(\overrightarrow{r}')\hat{r}|^2 dS \tag{3.14}$$

DDSCAT is a open-source Fortran-based software package applying the discrete dipole approximation (DDA) to calculate scattering and absorption of electromagnetic waves by metallic and dielectric nanostractures.

3.15 Finite-difference time-domain

Finite-difference time-domain (FDTD) computations involve discretization of time and space, such as all spatial and temporal derivatives in the Maxwell curl equations

$$\overrightarrow{\nabla} \times \overrightarrow{H}(\overrightarrow{r}, t) = \varepsilon(\overrightarrow{r}) \frac{\partial \overrightarrow{E}(\overrightarrow{r}, t)}{\partial t} \tag{3.15}$$

and

$$\overrightarrow{\nabla} \times \overrightarrow{E}(\overrightarrow{r}, t) = -\mu(\overrightarrow{r}) \frac{\partial \overrightarrow{H}(\overrightarrow{r}, t)}{\partial t} \tag{3.16}$$

are replaced by finite difference quotients. The quantities $\overrightarrow{r}$, t, $\overrightarrow{E}$, $\overrightarrow{H}$, $\varepsilon(\overrightarrow{r})$, and $\mu(\overrightarrow{r})$, $\overrightarrow{D}$, $\overrightarrow{B}$, are the position vector, time, electric field, magnetic field, permittivity, permeability, electric flux densities, and magnetic flux densities respectively. The FDTD approach is to introduce a plane wave at some initial time and find new field components by calculating different field components that applied during the previous time interval. For example, vector components of the electric field in the volume element are found at a given time, then the vector components of the magnetic field in the same volume element are solved at the next time interval. This process is kept going until the transient solution for the fields has computed to a steady state solution. Since the FDTD method is solved in the time domain, dispersion information must be specified more details about frequency ranges not just the range of interest. For instance, we need to use a frequency dependent permittivity model to approximate the permittivity of metallic structures, thus we can specify the frequency range for our simulation. FDTD simulation use the equation [90]:

$$\varepsilon(\omega) = \varepsilon_{\infty} - \frac{\omega_d^2}{\omega(\omega + i\gamma_d)} - \frac{\triangle\epsilon\Omega_l^2}{(\omega^2 - \Omega_l^2) + i\Gamma_l\omega} \tag{3.17}$$

to represent permittivity values, $\varepsilon(\omega)$ is the angular frequency of the incident radiation. Parameters; ε_{∞} ω_d, γ_d, $\triangle\epsilon$, Ω_l, and Γ_l are all constants [91]. By using FDTD method, we also can obtain the information of optical response in the frequency domain is determined by taking a Fourier transform of the time domain signal associated with the scattered electric field distributions. Moreover, FDTD methods have advantages such as providing both the near-field and far-field results from a single run.

Chapter 4

Optical switching of nematic liquid crystal films driven by localized surface plasmons

In this chapter, I present an all-optical technique to control the in-plane and out-of-plane spatial orientation of nematic liquid crystal (NLC) molecules by leveraging the highly localized electric fields ("hot spots") produced in the near-field regime of spacial arrangement of spherical gold nanoparticles (AuNPs). A NLC film, 2 to 3 micron thick, is deposited on a densely packed drop-cast AuNP layer, excited with tunable optical sources and the transmission of white light through it analyzed using polarization optics as a function of incident light wavelength, excitation power and sample temperature. Our findings, supported by simulations using discrete-dipole approximations, establish the optical switching effect to be repeatable, reversible, spectrally-selective, operational over a broad temperature range, including room temperature, and requiring very small on-resonance excitation power (0.7 μW). We have additionally demonstrated that controlling the incident excitation polarization can continuously change the orientation of the NLC molecules, allowing for grayscale transmission.

4.1 Introduction

Nanoparticles (NPs) exhibit unique electronic, magnetic and optical properties arising from quantum confinement that distinguish them from the constituent bulk materials [92]. These properties, coupled with a wide range of composition and morphology, have made NPs some of the most widely used materials in a variety of applications, which include optoelectronics, biomedicine, food processing, and renewable energy [93, 94]. A relatively new development is the use of NPs to create adaptive, or "smart," materials that allow re-

configuration of shape and functionality on demand. Such achievements are rooted in the material synthesis process where the end product needs to be robust, yet be capable of responding to external stimuli in a controllable manner. One particular thrust in this regard is the design and fabrication of smart materials where optical or electrical excitations are used as the primary means of external control. Another approach is combining anisotropic soft materials with metallic nanoparticles. Electrical conductivity of this hybrid material can be externally controlled, thus the material is useful for optoelectronic applications.

Liquid crystals (LC) are an ideal class of materials to serve as the anisotropic soft materials. They shows fluidity like a liquid, but it also demonstrates optical anisotropy like a crystal. LC exhibit high electro-optic and thermo-optic effects based on high birefringence and large dielectric anisotropy [95]. Additionally, LC can be controlled to exhibit phases of interest by adjusting temperature, therefore producing material mixture with LC relatively simple. To this end, there is a large body of work utilizing metallic nanoparticles dispersed in LC materials. The initial metallic nanoparticle solubility studies and dispersions in LC materials were conducted using AuNPs [96–99] and while these have now broadened in scope to include other types of NPs [100, 101], the study of AuNPs in LC continue to unearth exciting phenomena. These include the formation of LC phase transition driven ordered assemblies of AuNPs [102, 103] and stripe formation in nematic LC doped with chiral ligand-capped AuNPs [104].

From a functional perspective, LCs are a compatible and unique host for AuNPs, since the refractive index of the electro-optically active LC host can be controllably altered by many external parameters, such as temperature, light, and electric field to tune the localized surface plasmon resonance (LSPR) of the AuNPs dispersed within. This aspect has made LCs the ideal materials for designing novel active smart plasmonic devices that are easily reconfigurable in situ, where typically an external electric field is used to drive the LC orientational changes, which, in turn, tune the LSPR [105–108]. LSPRs are the localized versions of surface plasmon polaritons (SPPs). While SPP are propagating oscillations of the conduction electrons at a metal film-dielectric interface, LSPRs are observed in metallic NPs. At specific frequencies of an incident time-varying electric field, NPs exhibit resonantly-enhanced scattering and absorption in the near-field regime. The resonance condition is set by a specific relation between the frequency-dependent NP permittivity and the dielectric constant of the surrounding medium, known as Frohlich's condition [109]. In an ensemble of densely packed NPs, in the limit $d \ll \lambda$, where d is the interparticle separation and λ the wavelength of the incident field, the NPs act like interacting dipoles and far-field scattering is strongly suppressed. The results are highly localized scattered fields in the space between the NPs, creating what are popularly known as "hot spots." This phenomenon is widely exploited in well-known optical detention techniques such as SERS (Surface Enhanced Raman Scattering) [110] and MEF (Metal Enhanced Fluorescence) [104].

When the NPs are dispersed in LC medium, altering the LC molecules spatial orien-

tation using applied electric fields [104–107], thermal gradients [111–113] or optical excitations [114, 115] change the birefringence of the host, which in turn vary the medium permittivity. This provides a straightforward means of changing the Fröhlich's condition to tune the localized surface plasmon frequency of the NPs. Among these, the use of optical excitation as the controlling parameter offers several advantages, such as simpler device design without the need for specialized conducting substrates or wiring, spectral selectivity based on the size, shape and composition of the NPs, high spatial resolution. However, in order to control LC orientation using light, the usual approach is to include either a photo-responsive LC host, one that severely narrows the range of usable materials, or include a separate photo-active dye or polymer layer, again complicating the device design. In these proceedings, we will describe our work in designing an all-optical method for LC re-orientation that overcomes all the limitations mentioned above.

Our approach differs from the work on active plasmonics mentioned earlier as we leverage the plasmon response to optical excitation to control LC orientation, instead of the other way around. Our samples consist of a layer of closely-packed 30 nm AuNPs, with a 2-3 μm NLC film deposited on it. When these are excited with light resonant with the LSPR frequency of the AuNP ensemble, the electric field generated in the near-field of the AuNPs bring about a re-orientation of the NLC molecules in their immediate vicinity from the homeotropic to the planar state. This effect rapidly transmits through the entire NLC film, switching the bulk directionality. As expected, this effect is spectrally selective, responding to light of wavelengths within the LSPR absorption band. It operates over a wide temperature range starting at room temperature down to several degrees below the nematic-isotropic transition point. With low threshold power, is robust and stable. Additionally, by controlling the polarization of the incident driving excitation, we can extend this driving mechanism for in-plane switching as well.

4.2 Sample design and experimental set-up

Our device consists of a clover slip with the drop cast layer [116]. 10 μL of citrate-ligated 30 nm AuNPs (Sigma Aldrich) is deposited onto the surface of the uncoated glass slides. The solvent is allowed to evaporate for 10 h to form an AuNP layer, after which 5 μL of liquid crystal, 4-cyano-4'-pentylbiphenyl (5CB, Sigma Aldrich), in the isotropic phase is deposited onto a clean standard glass slide and covered with the AuNP layered cover slip. The LC between the glass slides is rapidly cooled from isotropic to nematic phase. As a result, a 2-3 μm thick NLC film is produced. No additional alignment layer is included to orient the 5CB molecules as the AuNPs are expected to promote a homeotropic alignment. As prepared, the NLC molecules show, on average, homeotropic alignment, orienting perpendicular to the surfaces. Extinction spectra for our samples are taken using a PerkinElmer UV/VIS spectrophotometer. This sample is placed between crossed polarizers of a Leica

DM2500P upright polarized optical microscope (POM) for collecting transmission images as shown in Figure 4.1. The broadband white light is incident from the bottom while the optical driving excitation (shown as a green beam) is focused from the top. This green excitation has a spectral range covering 520-550 nm.

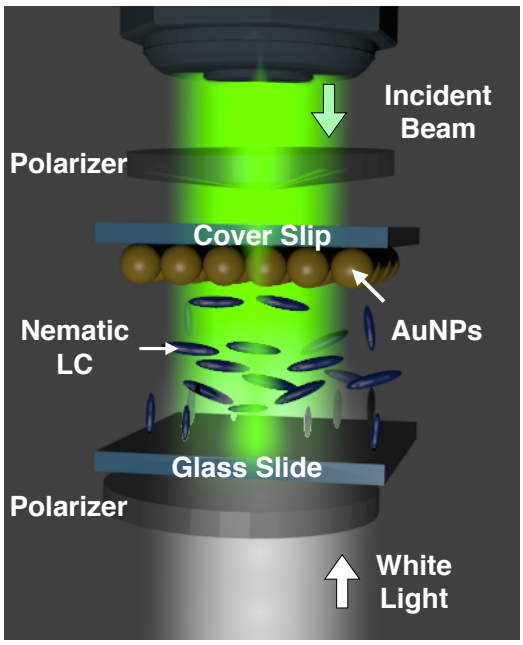

Figure 4.1: Device geometry. The white light beam is used to investigate the transmission through the sample, while he green incident beam is the optical driving excitation. In this schematic the NLC molecules do not demonstrate any overall alignment. (Reproduced by permission of ©2015 the Society of Photo-Optical Instrumentation Engineers.)

For quantitative measurements such as additional temperature, power and wavelength dependence of the switching effect, we use custom-designed optical set-up as shown in Figure 4.2 with two excitation sources: a continuous wave diode laser tuned to 532 nm (Verdi V6, Coherent Inc.) and a tunable (700-1000 nm) Ti:Sapphire laser (MIRA 900, Coherent inc.). A tungsten halogen lamp (HL-2000, Ocean Optics) is used as the broadband white light detection source. The excitation and white light beams are focused onto the sample, which is mounted on a heating stage (Instec Inc.) attached to a 3D mechanized scanning stage. Crossed polarizers, half wave-plates and silicon amplified photo detectors are incorporated in the path for transmission and in-plane rotation measurements. The two linear polarizers here mimic the cross polarization configuration of the POM (Figure 4.2). The white light first goes through a neutral density filter, one of the linear polarizers and a 50/50 beam splitter before passing through the sample. Following that, it is analyzed through the

second linear polarizer and the transmitted intensity is measured by the photo diode at the end. The drive incident beam at 532 nm is from a diode laser and joins the white light through the 50/50 beam splitter from the side, going through the sample and then a band stop filter to ensure it does not contribute to the final transmission signal (Figure 4.2). For control measurements with off-resonant excitation we use a Ti:Sapphire laser with a tuning range of 700-970 nm. In later stages for in-plane switching, additional polarization optics are introduced in the incident beam path, and these will be discussed later in Figure 4.9.

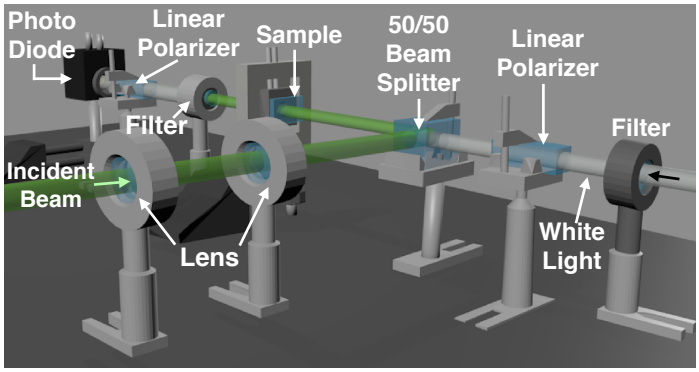

Figure 4.2: Schematic of optical set-up. (Reproduced by permission of ©2015 the Society of Photo-Optical Instrumentation Engineers.)

4.3 Results

Figure 4.3 summarizes our results demonstrating the out-of-plane switching. The AuNP layer promotes homeotropic surface anchoring and therefore 5CB molecules orient perpendicular to the glass slides as shown in the schematic in Figure 4.3 (a). Under crossed polarizers in the POM, the transmission image taken with only the white light appears dark (Figure 4.3 (c, left)) and we denote this as the "Off " state. When the sample is illuminated with an additional beam of wavelength in 520-550 nm range, as shown in Figure 4.3 (b), the transmission of white light is now much higher. The corresponding image (Figure 4.3 (c, center)) is bright over large regions, indicating that the LC molecules have re-oriented in the plane of the sample. This is designated as the "On" state. This spectral band is chosen as it is inclusive of the LSPR peak for 30 nm AuNP, verified in Figure 4.3 (a). As soon as the second excitation is turned off, the transmission reverts back to the initial dark image (Figure 4.3 (c, right)) and the sample is again in the "Off " state. The results so far clearly demonstrate a switching effect driven by the excitation light. We turn our attention next to understanding and quantifying this effect in order to optimize it and apply it to boarder scenarios.

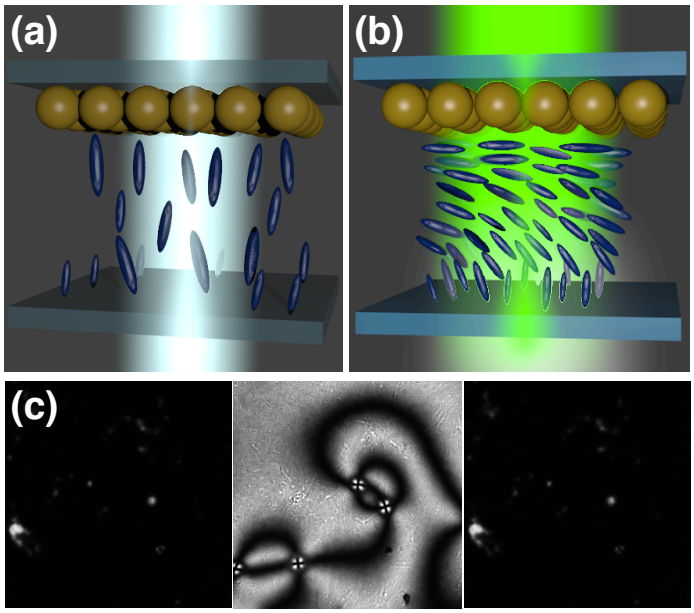

Figure 4.3: Schematic of experimental set-up demonstrating (a) "Off " configuration with only white light beam, and (b) "On" configuration with white light and resonant excitation beam. (c) Series of POM images of LC sample at 30 ^{0}C starting with resonant beam off, then turned on and then off again. (Reproduced by permission of ©2015 The Optical Society of America.)

Figure 4.4 (a) compares the extinction (scattering and absorption) spectra of our AuNPs when suspended in the citrate buffer (blue) and in 5CB (red). Typically, 30 nm AuNPs show an LSPR peak centered around 525 nm, but in the presence of the NLC material, the peak red-shifts to 532 nm, as is expected from the Frohlich's condition that increase in surrounding refractive index (permittivity) causes the resonance to move to longer wavelengths. Figure 4.4 (b) is a plot of the variation of white light transmission voltage with time, as measured by a photo-detector when excitations are turned on and off (dashed lines). For excitation (left axis) with 10 μW of λ = 532 nm light, the transmission goes from zero to a few volts on the photodiode when the light is turned on and then reverts to zero when turned off. In comparison, the use of 750 nm drive excitation does not result in any such change in transmission, confirming the spectral-selectivity of our method. This data makes an additional point, which is that for the on-resonance excitation of 532 nm, as long as the light is incident and the sample is in the "ON" state, the transmission is quite invariant with time, demonstrating stability of the re-oriented state. We have increased this time period up to 30 minutes and not observed any instabilities. We have confirmed this result using POM images over a period of many minutes.

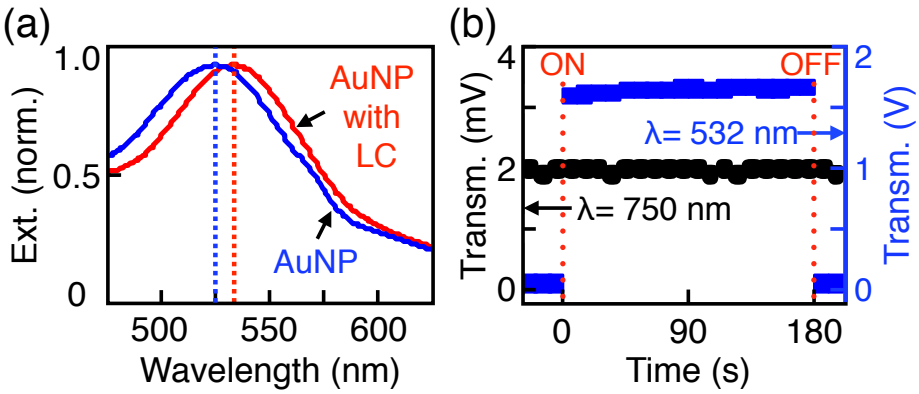

Figure 4.4: (a) Extinction spectra of 30 nm AuNPs suspended in its buffer solvent (blue) and in 5CB (red). (b) Transmission of white light as measured by photo-detector for resonant (blue squares) and non-resonant (black circles) excitation. Dashed line indicates when the excitation light is turned on and off. (Reproduced by permission of ©2015 The Optical Society of America.)

Based on this result, it is clear that an excitation in the green visible spectrum will result in strong near-field amplification, and this effect is seen in simulation in Figure 4.5 (a). It is a 5×3 array of 30 nm AuNPs arranged in hexagonal close-packed configuration in the x-z plane. The light of wavelength λ = 532 nm is incident normal to the plane and linearly polarized along the z-axis. The simulation uses a discrete dipole approximation package (nanoDDSCAT) [117] to calculate the near field scattering intensity and a normalized plot of the outcome shows the development of "hot-spots" in the interstitial regions between the AuNPs.

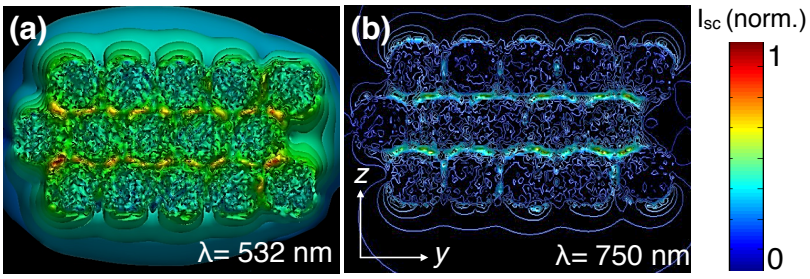

Figure 4.5: Near-field simulations of scattered electric field intensity when incident excitation is (a) resonant (532 nm) and (b) non-resonant (750 nm) with the AuNP extinction peak in Figure 4.4 (a). The incident light is incident along the y-axis and polarized along the z-axis. (Reproduced by permission of ©2015 The Optical Society of America.)

By comparison, scattering is strongly suppressed when this ensemble is excited with λ = 750 nm light (Figure 4.5 (b)) at the same average power and the lack of this resonant scattering results in no transmission change in Figure 4.4 (b). Establishing the wavelength selectivity of LC re-orientation is an important component, as it confirms that the origin of the observed switching is not associated with purely thermal effects of optical excitation. However, to further investigate the possibility of heating, we map the transmission in the "on" state with incident power and sample temperature in Figure 4.6 (a) for λ = 532 nm excitation.

Temperature is varied from 27 ^{0}C to 31 ^{0}C, to ensure 5CB is in the nematic state (N - I transition occurs at 35 ^{0}C) and incident power is varied from 0.7-86 μW at each temperature.

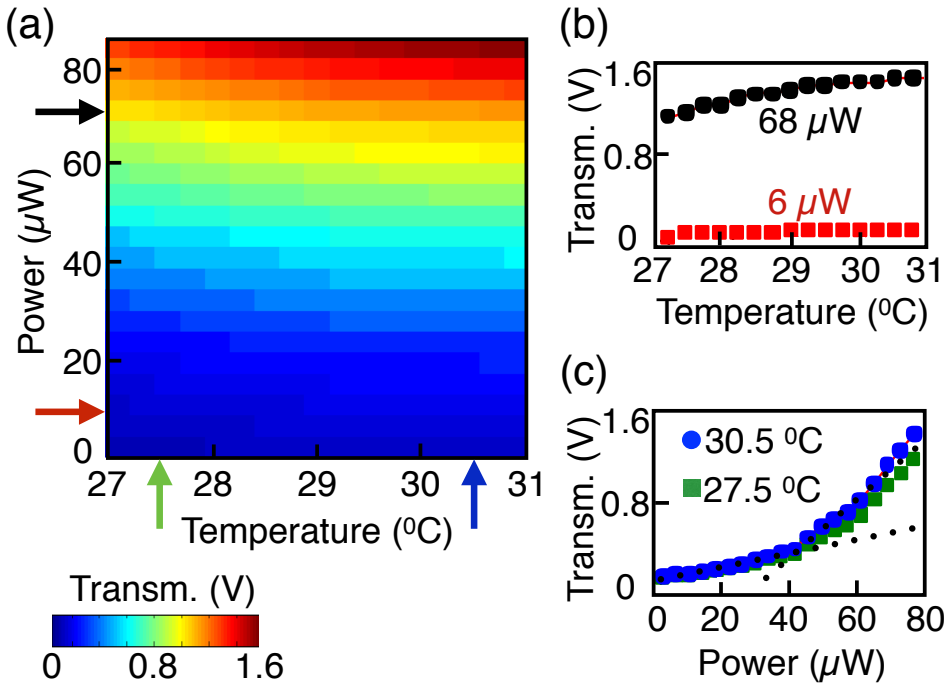

Figure 4.6: (a) Transmission in "on" mode mapped out as functions of resonant excitation intensity and sample temperature. (b) Transmission varying with temperature for two different excitation intensities, derived from line cuts along arrows shown in (a), (c) transmission changing with intensity at two different temperatures. Arrows in (a) show positions of line-cuts. Dashed lines in (c) indicate intensity where linear behaviour is disrupted. (Reproduced by permission of ©2015 The Optical Society of America.)

At first glance, it seems as if the total transmission intensity increases strongly with incident power, but is actually independent of temperature. Line cuts along fixed power in Figure 4.6 (b) confirms that while at low powers transmission is truly temperature independent at higher powers there is an increase in transmission intensity by $\sim 28\%$ over the measured temperature range. Similar data at 27.5 ^{0}C and 30.5^{0}C in Figure 4.6 (c) show that the power dependence of transmission intensity demonstrates linear behavior up to $\sim$ 50 μW, followed by a steep three-fold increase at higher powers for both temperatures. This indicates that incident power greater than 50 μW does cause local perturbations, most likely associated with heating.

This trend is further verified in Figure 4.7, where we plot transmission and associated switching time-scales with a variety of experimental conditions.

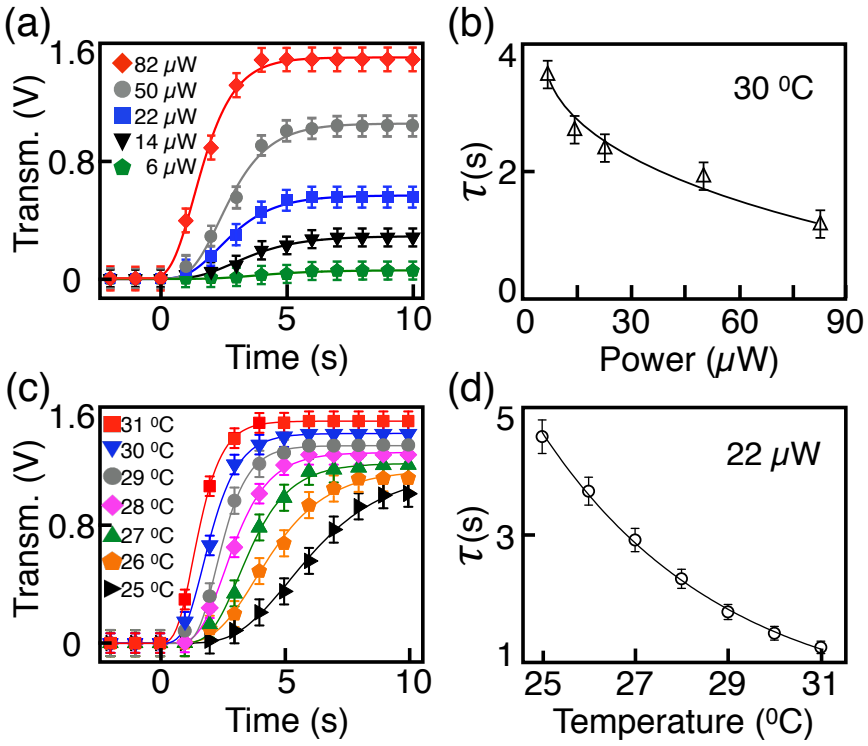

Figure 4.7: (a) Transmission measured as a function of time at different incident power and (b) Rise times extracted from fits to curves in (a) as a function of power. (c) Sample transmission measured at different temperatures and (d) the associated rise times. The AuNPs are drop-casted on only the cover slip. Time = 0 s denotes when resonant excitation is switched on. (Reproduced by permission of ©2015 The Optical Society of America and Society of Photo-Optical Instrumentation Engineers.)

In Figure 4.7 (c) we measure the transmissions at different temperatures with a constant on-resonance incident excitation power of 22 μW. The excitation is switched on at "0 s" and the change in transmission monitored continuously. All measurements are restricted to temperatures well below the nematic-isotropic transition of 35^0C. As the temperature is increased, we see both a faster switching and a higher transmission after switching, indicating higher spatial uniformity of NLC molecules post-realignment. However, the total variation of final transmission values is only 20 $\%$ over the entire temperature range, which leads us to conclude that thermal fluctuations do not play a dominant role in this process. Incident excitation power has a different effect, as seen in Figure 4.7 (a), with the transmission changing almost linearly with power up to 22 μW, and then increasing much more sharply. This non-linearity is undoubtedly a result of plasmonic heating due to high intensity of the excitation, a common consequence in metallic NPs. Figure 4.7 (b) and (d) are the characteristic rise times, τ, extracted from fits to the curves in Figure 4.7 (a) and (c).

As expected, the times get shorter and switching gets more rapid with increasing temperature and power. Yet even the fastest τ is much slower than the typical switching times achieved in NLC, which are in the millisecond range [118, 119]. However, our samples exhibit slightly longer times, between 1.5-3 s. This slow response is not entirely unexpected, given the geometry of our samples, where there is a large contrast between the thicknesses of the AuNP layer and the LC film. The AuNPs typically form a monolayer, though AFM measurements have shown occasional formation of up to four multilayers in certain regions, which account for the non-uniformity observed in Figure 4.3 (c). The plasmonic field generated by these AuNPs falls of exponentially over a depth of few tens of nm, which means only a few layers of LC molecules are under the direct influence of the scattered electric field. The time τ we measure and plot in Figure 4.7 is therefore the time for the elastic deformation of those few LC molecules to propagate through the remaining 2-3 μm thick LC film. As temperature or power increases, additional thermal fluctuations decrease the total time for the entire sample to re-orient by weakening anchoring conditions. These response times can be significantly increased by the use of thinner LC films, different LC materials optimized for display applications and AuNPs with morphologies tailored for plasmonic applications, such as nanorods, nanoprisms and bow-tie structures.

To mitigate this effect, we re-designed our sample with AuNPs deposited on both the cover slip and the glass slide. The results of switching speeds from those are shown in Figure 4.8. We label these the "double-sided" samples and notice right away that the transmission is higher and faster. The switching persists down to room temperature and fits from the curves in Figure 4.8 (a), resulting in switching times that are as fast as hundreds of milliseconds at higher temperatures (Figure 4.8 (b)). While still slower than typical timescales, this is an encouraging sign that tweaking the sample design can potentially improve this parameter vastly.

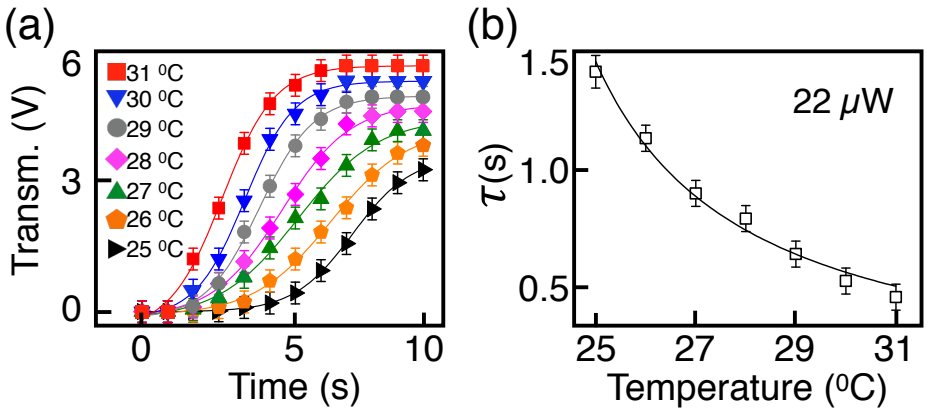

Figure 4.8: (a) Sample transmission measured at different temperatures for the re-designed samples. (b) Rise times extracted from fits to curves in (b) as a function of temperature. The AuNPs are drop-casted on both the cover slip and the glass slide. Time = 0 s denotes when resonant excitation is switched on. (Reproduced by permission of ©2015 The Optical Society of America.)

The dipole-like behavior of metallic NPs under plasmonic excitation implies that the ensemble has the usual anisotropic pattern of the near-field electric field commonly associated with dipole scattering and this directionality is determined by the incident field. We apply this to design an in-plane re-orientation platform. In-plane switching is an important functionality for LC molecules, especially in the context of pixel design because instead of a black-or-white output, this mode allows for gray scale control [120].

In our in-plane LC re-orientation platform, following the coordinates in Figure 4.9, $\theta = 0^0$ excitation creates hot spots only in the vertical interstitial regions but when the polarization is rotated by 45^0 there will be highly localized high intensity regions in the lateral inter-particle gaps as well. The two cases thus result in different orientation of the LC molecules in the plane of the sample. We leverage this effect to control the in-plane LC directionality in addition to switching from homeotropic to planar.

Figure 4.9 is a schematic of the optical set-up designed to continuously vary the linear polarization of the resonant excitation. Incident along the z-axis, the light first passes through a linear polarizer followed by a half wave plate and a liquid crystal variable wave plate. These last two polarization optics allow us to control the polarization of the light passing through them by externally controlling the birefringence of the variable wave plate. The transmission intensity detected by the photo detector beyond the sample is that of white light that passes through two crossed-polarizers (aligned along $\theta = 0^0$ and 90^0).

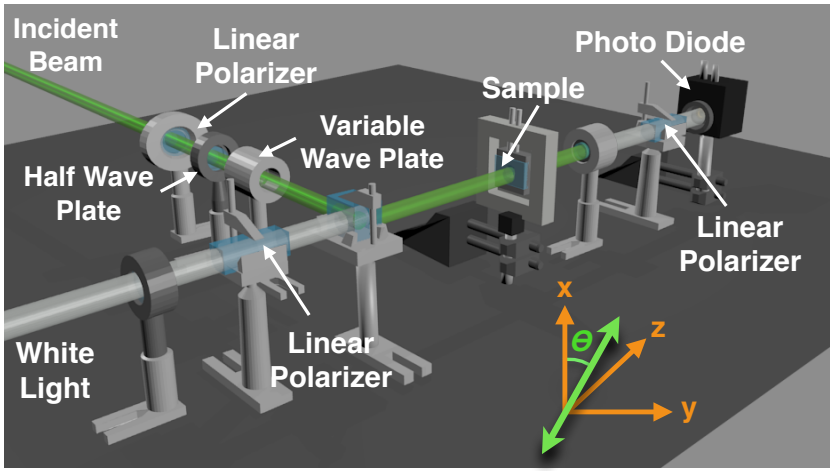

Figure 4.9: Optical set-up for rotating incident electric field polarization. Resonant excitation is incident to the sample along the z-axis and the sample is mounted in the x-y plane. (Reproduced by permission of ©2015 The Optical Society of America.)

In this arrangement, an applied AC voltage to a suitable calibrated variable wave plate allows us to continuously vary the angle of the incident linear polarization in the x-y plane. We denote this angle θ as measured from the vertically aligned x-axis in the schematic. We note that the white light used to measure the transmission is not subjected to this, and the crossed polarizers are also not altered. The measurement progresses in exactly the same manner as earlier.

Figure 4.10 shows simulations that depict our hypothesis for in-plane switching.

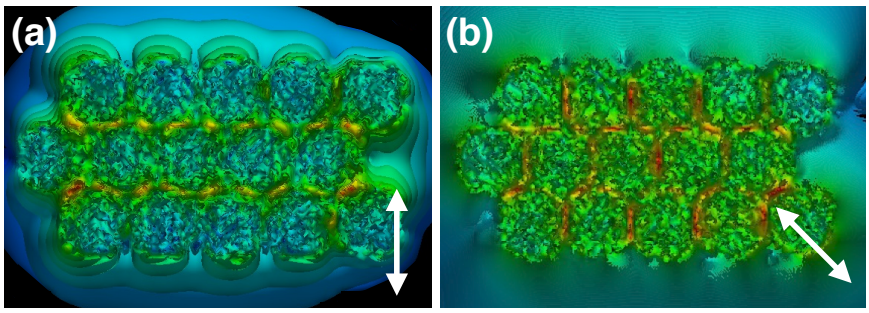

Figure 4.10: Simulations of the near-field plasmonic scattering when the incident polarization is (a) $\theta = 0^0$ and (b) $\theta = -45^0$. (Figures reproduced with permission from the Optical Society of America.)

Figure 4.10 (a) is a simulation of the plasmonic field under conditions identical to Figure 4.5 (a), with light incident perpendicular to the plane of the AuNP array and the white arrow designating the linear polarization. In keeping with the coordinate system in Figure 4.9, we call this θ = 0^0. Figure 4.10 (b) shows the same array, but the incident polarization is now θ = - 45^0. Comparing the two, we can clearly see a change in the pattern of the "hot-spots," and it follows that the NLC molecules would respond with altered director axis if the incident polarization is varied.

In Figure 4.11, we plot the experimental results of the measurement. At the very start of the measurement prior to any exposure to the driving excitation, the NLC molecules are homeotropically aligned. We begin with the incident light polarized at θ = 0^0, a direction which is orthogonal to one of the crossed polarizers used for analysis of the transmission. Resultantly, as the NLC molecules switch from out-of-plane to in-plane, their average orientation is also along θ = 0^0, and the transmission measured by the photodiode is nil. Next, keeping the sample planar aligned and without reversing to homeotropic, we change the polarization of the green light. As θ increases, so does the transmission, which is then maximized at θ = 45^0, falling off after that to repeat the pattern symmetrically as we tune through 180^0. We can fit the data to the well known $I = I_0 sin^2\theta$ curve. This is a significant result, as it not only validates our understanding that optically induced plasmonic fields are the controlling factors behind the re-orientation, but in-plane switching is itself a useful tool in the development of complex display platforms.

As the plot in Figure 4.11 affirms, the transmission through the sample is no longer limited to a binary state of complete darkness or brightness, but as directed by the incident

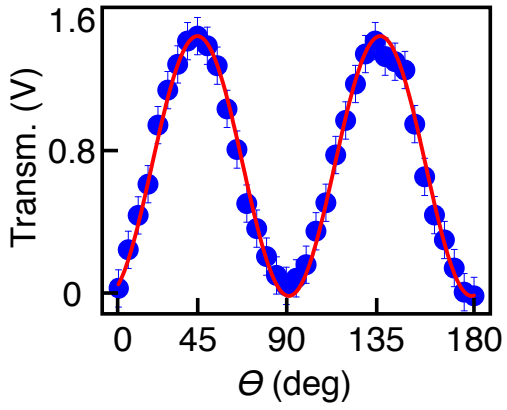

Figure 4.11: Transmission of white light from the sample measured as a function of incident polarization angle θ. The fit is $I = I_0 sin^2\theta$. (Reproduced by permission of ©2015 The Optical Society of America.)

polarization, can continuously vary between the extremes to produce a gray scale effect.

4.4 Discussion

Our results definitively demonstrate re-orientation of NLC molecules from out-of-plane (homeotropic) to in-plane (planar) alignment. In this particular case, the samples are irradiated with optical excitation with wavelength that lie in the LSPR absorption band of the AuNP layer deposited on the surfaces sandwiching the liquid crystalline film. This effect is stable and reversible. We can disregard thermal effects associated with the excitation beam itself from the results of Figure 4.4 (b) for two reasons: Firstly, if the incident light was merely heating the samples, the NLC would transition to the isotropic phase, in which case the transmission would remain dark as that does not cause an in-plane alignment; Secondly, this effect would not be spectrally selective. There is, however, another thermal mechanism that could come into play when plasmonics is involved, and that is heat generated by the NPs themselves as a result of the strong absorption at the LSPR peak [121]. This effect is spectrally-selective, falling off rapidly as the excitation moves away from the LSPR value. Additionally, at high excitation powers, simulations have shown that AuNPs can generate localized temperature gradients as large as tens of Celsius. To determine how large a role plasmonic heating plays, we estimate the maximum temperature change following formulation in reference [121] for our highest excitation intensity (86 μW) to be $\sim 0.1^0$C. This is an approximation, and our densely packed film has the possibly to develop larger thermal gradients. Such outcomes are unlikely to be large enough to be the cause of the observed re-orientation. We can therefore conclude that the main driving mechanism is the localized electric fields generated by the AuNPs that bring about the NLC switching, with some assistance from the plasmonic heating, which probably weakens the anchoring of the NLC molecules. This last part most likely is the reason behind the faster switching with increasing power observed in Figure 4.7 (b).

The homeotropic-to-planar re-orientation is a natural consequence of the polarization of the incident excitation. The driving optical beam is always polarized in the plane of the samples, and the plasmonic field follows the same directionality. As a result, the homeotropic NLC molecules right next to the AuNP layers see an electric field perpendicular to their orientation, and switch in that direction. It therefore follows from this construct that the director axis of the NLC molecules should always align with the incident polarization. We apply this to design an in-plane re-orientation platform. We have successfully demonstrated that we can direct the in-plane orientation of the LC molecules as well, by modulating the incident polarization. Figure 4.11 shows this transmission voltage as a function of the incident polarization angle θ. The variation pattern indicates the in-plane LC orientation tracks the incident polarization exactly, showing no transmission when the polarization is along the optical axis of either polarizers, and maximum transmission when

θ = 45^0 and 135^0. This is a demonstration of a new all-optical in-plane switching mode where molecular orientation can be varied continuously, and faster than the out-of-plane switching [119] as previously discussed. The last question that remains is estimating the magnitude of the electric field generated in the near-field of AuNPs. We calculate our incident electric field to be 5 mV/μm, which, subject to the enhancement factors, produces fields in the range 0.05-0.25 V/μm. These values are within the order of magnitude of threshold fields for switching of 5CB molecules in the nematic phase, and aided by localized thermal fluctuations on-resonance, is sufficient to cause the switching.

4.5 Conclusion

We have presented here a method of controlling spatial orientation of LC molecules on a macroscopic scale that exclusively utilizes optical excitation. Beginning with a simple out-of-plane to in-plane switching, we have extended this approach to include the ability to controllably vary the in-plane director orientation. This effect is initiated by the plasmonic fields that develop in the near-field regime of an underlying metallic nanoparticle layer when the NPs are excited resonantly with an incident laser, and propagates through a micron thick NLC film via elastic deformation of the bulk. The threshold excitation power required is as low as 0.7 μW and the out-of-plane switching time scale is in the range of a few seconds to hundreds of milliseconds. These metrics are obtained using a fairly simplistic sample design (Figure 4.2) and with a commonly available NLC material that is not optimal for switching speeds. The application design and results we present here are the first demonstration of all-optical control of liquid crystal re-orientation. This is a significant step in the development of "smart" materials because this can be a means of fabricating novel devices, such as electronic skins, smart cards, ultra-thin low power displays and autonomous filters.

In the near future, we plan to systematically improve the performance of LSPR-driven switching. Some of the aspects we will focus on include: first, uniform and patterned AuNP layers, which will improve the homogeneity of the realignment of the NLC director, eliminating defect textures seen in Figure 4.3 (c, center); second, investigate other AuNP morphologies, particularly nanorods. Nanorods have two advantages over the spherical NPs. They provide a strong directionality of the plasmonic scattered field as a result if their inherent anisotropy, and this would lead to uniformity in the re-alignment, provided the nanorods themselves have some overall directionality in the deposited layer; in addition, they have two LSPR peaks corresponding to the short and the long axes, and these can be leveraged to develop a two-color scheme; finally, experiment with NP surface chemistry to tune the NLC anchoring conditions for uniform and faster switching.

4.6 Acknowledgements

This work was supported by awards from the National Science Foundation DMR-1056860 and in part by the NSF nanoBIO node, ECC-1227034. Prof. Ghosh would also like to acknowledge National Science Foundation Grant No. PHYS-1066293 and the hospitality of the Aspen Center for Physics.

Chapter 5

Thermotropic liquid crystal mediates assembly of nanoparticle microcapsules

In the following chapter, I depict the formation and structural characteristics of micro-scale capsules constructed with nanoparticles. The microcapsules were composed of closely packed nanoparticles (NPs), which constructed a wall-like thin outer-layer structure, and stabilized by local crystallization of the customized mesogenic ligands. We used phase transition of a liquid crystal (LC) host media as a template for assembling NP capsules. I also introduce our mechanism and experimental observation of NP microcapsules' formation. Additionally, I discuss the average interparticle distance of quantum dot and gold nanoparticles, located on the thin outer-layer of the microcapsules, with different types of customized mesogenic ligands. Our study shows that interparticle packing space can be tuned to vary flexible attachment of alkyl chain lengths in mesogenic ligands. Moreover, our assembly method can be extended to different type of NPs, such as metallic, magnetic, semiconducting, and dielectric. This thermally and fluid-based nanoparticle-sorting process represents a versatile self-assemble method for making 3D capsule-like NP structures.

5.1 Introduction

Materials with three-dimensional (3D) structures, such as nano- or micro-lattices, are high interest research topic in modern science and engineering [122]. Materials with 3D shape may bring evolutional change for material properties and functionalities in wide variety of applications, such as biomedical devices [123], microfiltration membranes [124], microfluidic devices [125], high-capacity/quick-charging batteries [126]. Similarly, self-assembled nanoparticle or nanocrystal 3D lattice structure can be useful for optical, electrical, and catalytic properties that might have different characteristics from their respective bulk properties.

Likewise, the characteristics of 3D assemblies can be turned by varying not only the size or shape of NPs as well as the distance between them but also 3D spatial arrangement. Therefore, self-assembly of nanoparticles has been identified as an important process where nanoparticles in the system spontaneously organize into the ordered structures by thermodynamic and other constraints [127–129]. Moreover, the different phase morphologies can be self-assembled in the phase separation or phase transition processes in many composites based on nanocrystal polymer and nanoparticles [130, 131]. A fluid-based approach has better chance for manufacturing self-assembled 3D micro-structures, our work focuses on liquid crystal (LC) solution-based nanoparticle (NP) assemblies; we recently reported the use of our customized ligands to disperse semiconductor nanoparticles, quantum dots (QDs), in the nematic LC phase [132]. Our customized ligands were designed to be miscible with the host nematic LC media. The ligands were also allowed to rotate on their flexible alkyl side chains of their molecules for aligning with nematic host media surrounding the NPs. Our customized ligands attached to a NP surface and tended to align with a nematic director of a surrounding LC [132].

Using our notable mesogenic ligands, we exploited a liquid crystal droplet templated process and the phase dependent miscibility behavior of NPs in a nematic LC. We used the unique process and miscibility behavior, carried on during isotropic to nematic phase transition, to sort nanoparticles in host media and form densely-packed nanoparticle microcapsules. Our template is an excellent contribution to self-assembled 3D nanostructure stability and tenability.

5.2 Experimental methods

5.2.1 Ligand exchange synthesis

Nanoparticles (1 nmol) were dissolved in 1 mL of chloroform. A solution of the mesogenic ligands dissolved in chloroform (40 mmol) was added to the quantum dot solution, heated to 40-45 ^{0}C, and stirred for 3-5 hours. The mixture was then taken off heat and left to cool back to room temperature. 2 mL of ethyl acetate-methanol (1:1) were then added to the ligand-exchanged nanoparticle solution and centrifuged. The precipitate was washed two more times using a 1:1:2 solution of toluene, chloroform, and ethyl acetate-methanol mixture. The precipitate was finally re-suspended in 1 mL chloroform.

5.2.2 Nanoparticle-liquid crystal mixture

Mesogen functionalized semiconductor nanoparticles, 620 nm CdSe/ZnS quantum dots (NN Lab) and 5nm diameter gold nanoparticles were added to a nematic liquid crystal (NLC) 4-cyano-4'-pentylbiphenyl (5CB, Sigma Aldrich) at the required wt $\%$. The mix-

ture is heated to the isotropic phase, above 35.5 ^{0}C for 5CB, and sonicated in warm-bath for eight hours in a glass vial with the cap removed. This method allows the toluene to gradually evaporate from the liquid crystal mixture as the nanoparticle (NP) are dispersed in LC media. The complete chloroform removal was determined by measuring the nematic-to-isotropic phase transition temperature by using differential scanning calorimetry (DSC). The composite material could then be transferred to a microscope slide, a Eppendorf tube, or glass capillary. NP-LC mixture was kept above the isotropic phase transition and carefully cooled at the desired rate for imaging and X-ray diffraction experiments.

5.2.3 Polarized and fluorescence microscopy

Polarized optical microscopy (POM) was carried out using a Leica DM2500P upright microscope in transmission mode (Leica Microsystems Inc., Bannockburn, USA) with a 20x, 40x, 63x objective. Linkam temperature controlled heating/cooling stage was used for maintaining the optimal temperatures and controlling an accurate cooling/heating rate during imaging. For fluorescence imaging of the quantum dot microcapsules with a peak emission at 620 nm, a 515-560 nm band-pass filter with white-light mercury lamp illumination was used. Emission was collected using a 580 nm dichroic mirror and a 590 nm long pass filter. Our samples were mounted on standard glass slides with cover slip, homeotropic and planar liquid crystal alignment was achieved using a cetyltrimethylammonium Bromide (CTAB) and polyvinyl alcohol (PVA) surface coating respectively. For varying size of nanoparticle microcapsules, we controlled cooling rate on Linkham LTS350 cooling stage when LC-AuNP mixture was cooled into the nematic phase. For instance, the fastest cooling rate, 3 ^{0}C/s, and the slowest rate, 0.2 ^{0}C/s, were set for producing gold nanoparticle microcapsule formation. The formation process can be carried out on a microscope slide or Eppendorf tube.

5.2.4 Small angle x-ray scattering measurement

Small angle x-ray scattering (SAXS) measurements were performed at the Stanford Synchrotron Radiation Lightsource, beamline 4 – 2. Nanoparticle-liquid crystal (NP-LC) mixtures were prepared at the beamline and filled into 1 mm quartz capillaries. SAXS experiment were carried out 20 hrs after we prepared our samples. The capillaries were mounted in transmission configuration using a custom chamber. Our measurements were taken at 11 keV for 1 second per exposure at three spatially different points on each capillary with a beam size of 0.3×0.1 mm at the sample. Our data was analyzed at the beamline using the custom Sastool software program.

5.3 Results and discussion

5.3.1 Mechanism of shell formation by sorting nanoparticles

We designed and synthesized a series of customized ligands, exchanged onto the surface of CdSe/ZnS core–shell QDs and AuNPs. Our customized ligands were liquid-crystalline-like, "mesogenic", and composed of a rigid rod-like segment with flexible-arm sections. Generally, a flexible-arm with amine (-NH_2) segment, attached to the particle surface, controls ligand alignment with the surrounding host nematic phase media. We recently reported QDs with our customized mesogenic ligands showed high dispersibility or miscibility in the anisotropic LC solvent by reducing strain on the LC surrounding the particle [132]. These ligands also induced particle-particle short-range attraction [3].

NLC normally behaves like a liquid, being free to move and with no positional order, however differ in the respect that the molecules tend to align with one another. Above the nematic-to-isotropic phase transition point, the fluid behaves as a conventional liquid, called isotropic phase. When LC in isotropic phase is cooled to the nematic transition temperature, domains of nematic ordering nucleate and grow. During the phase transition, any dispersed NPs in the material will respond to the local nematic order parameter and preferentially move into the shrinking isotropic domains (Figure 5.1 (b)). This is because the dispersed NPs reciprocate to their changing local environment and move to low elastic free energy regions, whose locations usually has low orientational order conditions.

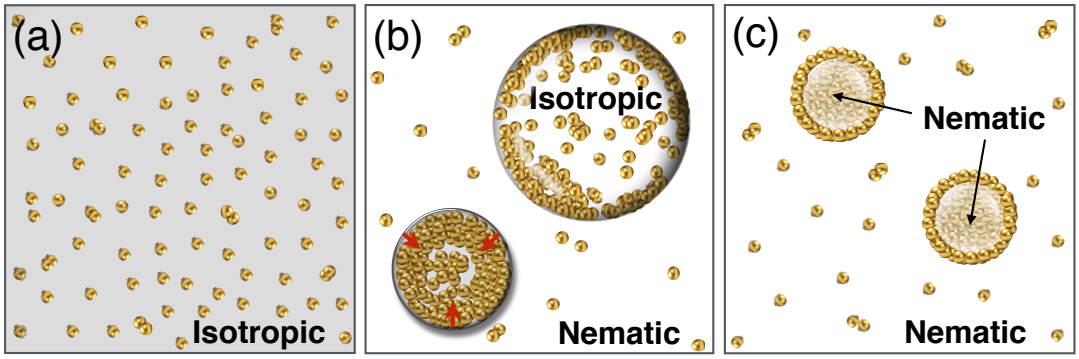

Figure 5.1: Formation mechanism for nanoparticle capsules. (a) Initially, nanoparticles (gold color) are dispersed in the isotropic phase (gray), and then (b) sorting as the nematic phase (white) nucleates and grows. During an isotropic-nematic phase transition, most nanoparticles are segregated into isotropic droplets. The shrinking phase boundary assembles our capsule formation by thickening walls of the nanoparticle capsule. (c) Schematics of the cross-section of nanoparticle capsules constructed at the end of the isotropic-nematic phase transition.

The existence of NPs in the NLC phase will cost more free energy to be in that area because the average local LC molecular orientation, called LC nematic director, deforms to accommodate the presence of small colloidal particles. To reduce the deformation, NPs that small enough to respond to Brownian motion need to re-locate in the domains of low molecular order. In our case, low elastic free energy (low-molecular-order) regions denote as at topological defects. Hence, minimizing the elastic free energy of the system, then phase separates into LC droplets with high NP concentration (isotropic domain), and with low NP concentration (nematic domain), which is shown in Figure 5.1. These effects are crucial aspects in our microcapsule-formation mechanism.

5.3.2 Assembling nanoparticle microcapsules

Our mesogenic ligands contain a varying length in the alkyl amine (-NH_2) side-arm, and the side-arm attaches to the nanoparticles' surface during ligand exchange synthesis. 0.3 wt$\%$ ligand-exchanged CdSe/ZnS quantum dots (6.2 nm core diameter, NN Labs Inc.) and 1.2 wt$\%$ AuNPs (5 nm, Nanopartz) are then dispersed into nematic liquid crystal, 5CB (Sigma Aldrich). These NP-LC mixtures were sonicated in 40-45 ^{0}C warm bath for three to five hours. In the sonication process, AuNP-LC mixture sample required more careful treatment than QD-LC. Most importantly, the effect of the ultrasonic system on the stability of AuNPs depended on the time, temperature, frequency/power of the sonicator. For example, we observed that extended sonication time caused the aggregation of AuNPs in LC solution. Additionally, higher temperature sonication of AuNP-LC mixture with existence of chloroform led AuNPs to trigger severe aggregations. Moreover, we noticed the aggregation of AuNPs in the sample solution when we used higher frequency/power of the sonicator. UV-Vis absorption spectrometer was used to investigate the particle aggregation in LC media since the pattern of absorption lines shifts to the red when AuNPs aggregated. Unfortunately, the aggregation of AuNPs were irreversible, thus creating homogeneous dispersion of AuNPs in LC media must require excessive amounts of attention.

We verified an excellent initial dispersion by using fluorescence microscopy for QD-LC mixture. After a homogeneous suspension was observed, NP microcapsule formation was initiated by cooling the NP-LC mixture. Both QD and AuNP capsules were formed by following the same procedure. As the NP composite mixture was cooled into the nematic phase by controlled cooling rate from a 40 ^{0}C at 31 ^{0}C on a Linkham LTS350 cooling stage. During the cooling process, fluorescence microscopy (Leica) was used to track QDs particle movement throughout the isotropic-nematic phase transition and therefore elucidated the microcapsule formation process by tracking fluorescence emission from QDs particles (Figure 5.2).

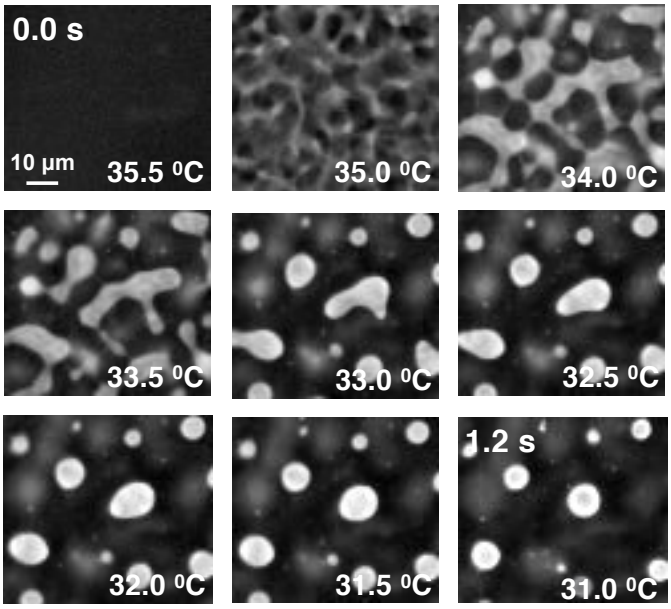

Figure 5.2: Series of images from a high speed fluorescence video illustrating the QD microcapsules formation process by visualizing QD NPs distribution over 1.2 seconds. (Reproduced from reference [3] with permission from the Royal Society of Chemistry.)

Similarly, optical cross-polarized microscopy was utilized to follow the formation of AuNP microcapsules (Figure 5.3). This is because AuNPs do not emit light like QDs. Thus, we monitor the different intensities of the transmitted light, different effective birefringence features, based on the tilt angles of the liquid crystal molecules around isotropic domains, isotropic droplets, or our NP capsules during isotropic-nematic transition. These unique birefringence features was also observed in every time when we assembled our QD microcapsules. As we discussed above, before cooling the NP-LC mixture in isotropic phase, QDs or AuNPs must be uniformly dispersed. Nematic domains started to nucleate and grow when the mixture was cooled from the isotropic to nematic phase transition temperature. The isotropic domains shrink and formed spherical shape and the shrinking isotropic regions were disappeared at the end of the phase transition (Figure 5.3). During the phase transition, QDs or AuNPs were separated from these expanding nematic regions and moved into the shrinking isotropic domains. NPs at the shrinking isotropic region were dense enough to create ligand-ligand interaction, long enough to crystallize at neighboring ligands, and large enough area to produce a multilayered densely-packed spherical capsule-wall before disappearing isotropic shrinkage droplets.This shrinking isotropic region varied the size of our microcapsules. Summarizing the above results and discussion, these series of images in Figure 5.2 show several fluorescence microscopy snapshots of the formation

process, clearly showing QDs segregation, droplet formation and wall thickening. From the series of fluorescence images, we can monitor that the isotropic to nematic phase transition templated QDs assemblies at the phase boundary.

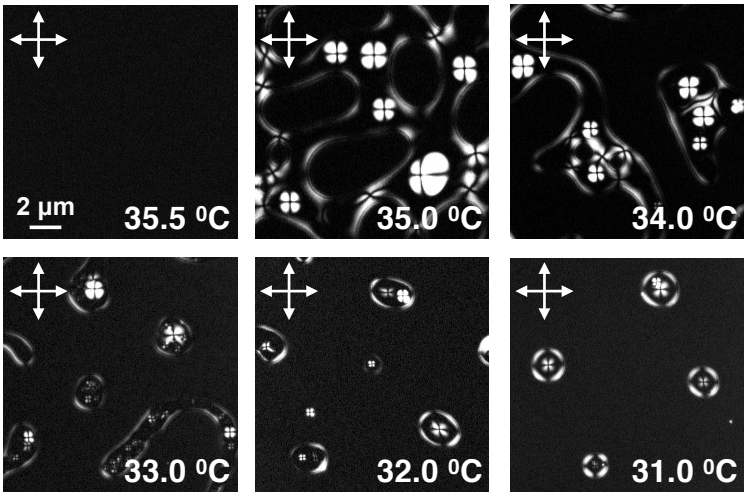

Figure 5.3: Series of images from a high speed cross-polarized video displaying the AuNP microcapsules formation process by visualizing effective birefringence features of the liquid crystal around isotropic domains, isotropic droplets, or our NP capsules. Our AuNP-LC mixture was cooled at a constant rate 1 ^{0}C/s.

Interestingly, we observed the size of NP microcapsule can be controlled by cooling rate of NP-LC mixture. In QD-LC mixture, $\sim$10 μm microcapsule (Figure 5.4 (a)) and $\sim$70 μm (Figure 5.4 (c)) were observed at faster and slower cooling rate respectively. In AuNP-LC mixture, the faster cooling (3 ^{0}C/s) resulted in the formation of AuNPs microcapsules with diameter $\sim$1 μm (Figure 5.4 (b)). The slowest cooling rate (0.2 ^{0}C/s) produced AuNPs microcapsules as large as 5 μm, which is shown in Figure 5.4 (d). These size differences between QD and AuNP capsules could be caused by the differences of the particle density. Since the velocity of the shrinking isotropic domain during the isotropic-nematic phase transition stays the same, faster particle movement, caused by lower value of the particle density, was able to create the larger size of the microcapsules.

Switching microscopy setting into the cross-polarized mode, we could monitor unique birefringence characteristics of liquid crystal in surrounding area of our microcapsules. Figure 5.4 (e) and (d) are cross-polarized image of hemeotropically aligned sample of QD and AuNP microcapsules. The host nematic liquid crystal appeared dark because the nematic director was positioned parallel with one of the crossed polarizers, indicated by the white arrows. Most importantly, a radially contrasting birefringence pattern images at the location of both a QD and a AuNP microcapsule implied that the mesogenic ligands were

aligned perpendicular to the capsule surface to produce a homeotropic surface-anchoring condition. Figure 5.4 (g) and (h) show horizontal Saturn ring (quadrupolar) defects around both QD and AuNP capsules. The quadrupolar defect pattern indicated the outer ligands were aligned parallel to the capsule surface, producing a planar surface-anchoring condition. In this image, the surrounding liquid crystal molecules were aligned using a polyvinyl alcohol (PVA) alignment layer. These topological defects were visualized with optical microscopy, providing specific information on ligand organization at the surface of nanoparticle microcapsules. Saturn ring defects generally appeared to exhibit planar surface anchoring sample and radial (hedgehog) defects showed regularly in homeotropic alignment sample. Based on these defect observations, both QD and AuNP microcapsules had very similar spherical like structures.

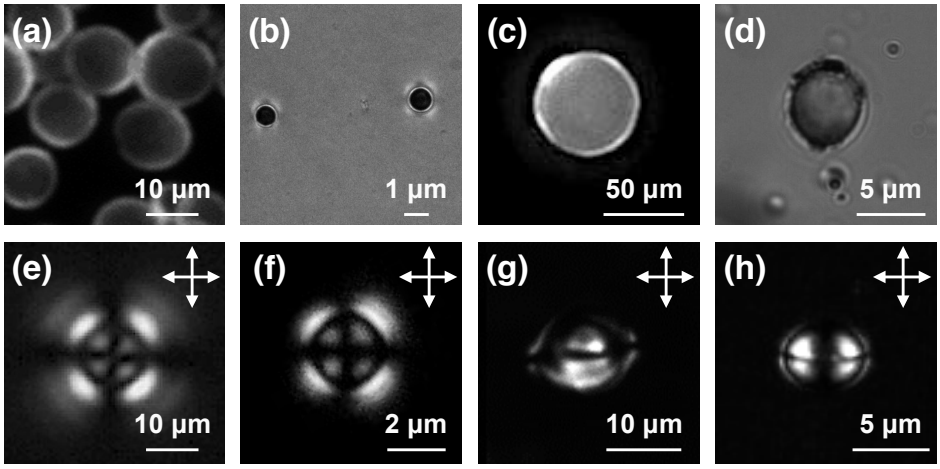

Figure 5.4: Fluorescence microscopy image of CdSe/ZnS QD microcapsules with (a) faster cooling (3 ^{0}C/s) and (c) slower cooling (0.3 ^{0}C/s). Optical microscopy image of AuNP microcapsules with (b) faster cooling (3 ^{0}C/s) and (d) the slowest cooling rate (0.2 ^{0}C/s). Cross-polarized microscopy images of (e) a QD and a AuNP microcapsule. A polarized optical microscopy image of a QD microcapsule with (e) homeotropic (g) planar cell. Images of a AuNP microcapsule taken by cross-polarized microscopy were located in (f) homeotropic and (h) planar cells. The polarizers are crossed as indicated by the white arrows. In homeotropically aligned cells, similar topological defects (radial hedgehog) were visible in the centre of the (e) QD and (f) AuNP microcapsules. Likewise, we could observe "Saturn-ring" (quadrupolar) defects in surrounding area of both (g) QD and (h) AuNP microcapsules placed in planar aligned samples. All NP microcapsules (a-h) were suspended in 5CB nematic liquid crystal at room temperature. (Figure 5.4 (a) and (g) were reproduced from reference [3] with permission from the Royal Society of Chemistry.)

5.3.3 Controlling interparticle space by varying alkyl chain lengths of mesogenic ligands

As we mentioned earlier, our customized mesogenic ligands were composed of a rigid rod-like segment with flexible-arm sections.The flexible-arm segment has two sides; with amine (-NH_2), located at the bottom-right side of the molecule, and without amine group, branched on the bottom-left side of alkyl chains (Figure 5.5 and 5.6).

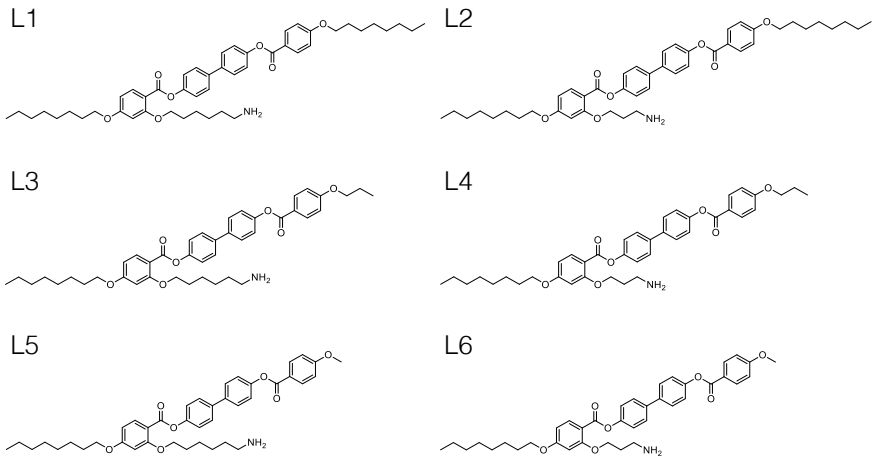

Figure 5.5: Molecular structures for L1 though L6 mesogenic ligands.

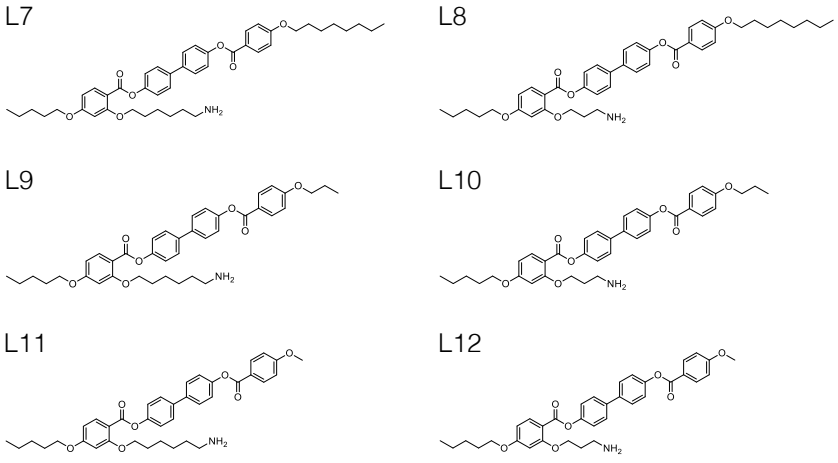

Figure 5.6: Molecular structures for L7 through L12 mesogenic ligands.

We explored nanoparticle packing structures of microcapsule wall by using small angle X-ray scattering (SAXS). Specifically, we investigated interparticle distance, varying different alkyl chain lengths of flexible segments and a rod-like rigid part in mesogenic ligands. The structures of 12 different ligands are shown in Figure 5.5 and 5.6. We plotted of the scattering intensity versus diffraction angle, extracted by the scattering patterns from SAXS measurements, offered the average interparticle space between particles. Generally, the peak at smaller scattering angles represents larger particle-particle average distance.

In Figure 5.7, the red broad peak at q= 0.0616 $\mathring{A}^{-1}$ demonstrated an interparticle distance, average spacing between quantum dots, of 10.20 nm. This number agreed the expected interparticle space of QDs surrounded by bulky mesogenic ligands, which is reported in our previous study [3]. QDs functionalized with ligand L2 had a shorter flexible alkyl chain lengths, illustrated a slight shift to the right in the red peak. This shifted blue peak value shows a QD spacing of 9.94 nm, compared to 10.20 nm for the longer chain of ligand L1.

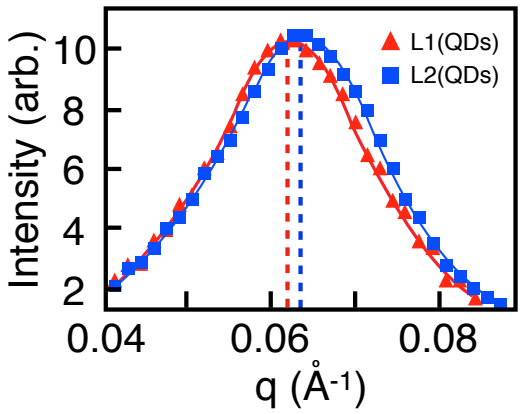

Figure 5.7: X-ray scattering data for QD microcapsules with ligand L1 and L2.

Similarly, we performed the same experiment by using AuNPs with L1 and L2 ligands. The red peak, AuNPs functionalized by L1 ligands, and the blue peak from L2 functionalized AuNPs at q= 0.0520 $\mathring{A}^{-1}$ and q= 0.0564 $\mathring{A}^{-1}$ indicated 12.08 nm and 11.14 nm average particle-particle distance respectively (Figure 5.8). Differences of average QDs' interparticle distance between L1 and L2 ligands were 0.28 nm, however average AuNP-AuNP spacing differences between L1 and L2 were 0.94 nm, which was roughly three times more than QDs values. Based on these experimental results, QDs tended to pack tighter than AuNPs in LC, 5CB, host media.

We synthesized shorter alkyl chain ligands at the end of a rigid rod-like segment, from L3 through L6 ligands in Figure 5.5, and opposite side of the amine substituent branch of flexible arm-like part, from L7 through L12 in Figure 5.6.

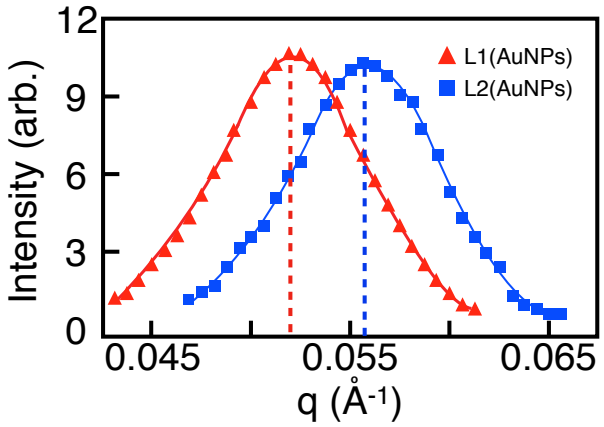

Figure 5.8: X-ray scattering data for AuNP microcapsules with ligand L1 and L2.

These synthesized ligands were used to examine the relationship between lengths of alkyl chain and interparticle spaces. L3 and L4 have 8 carbons found in the left side of the flexible-arm segments and 3 carbons located at the rigid rod-like segment (Figure 5.5). The only differences between them are the number of carbons in the right side of flexible segments. L3 has 3 more carbons than L4, which is very similar relationship between L1 and L2. The orange peak from mesogenic L3 ligands and the green peak from L4 ligands (Figure 5.9) revealed 11.98 nm and 10.97 nm average interparticle distance. That is, average AuNP-AuNP spacing differences between L3 and L4 were 1.01 nm, which was very close to the values between L1 and L2, 0.94 nm.

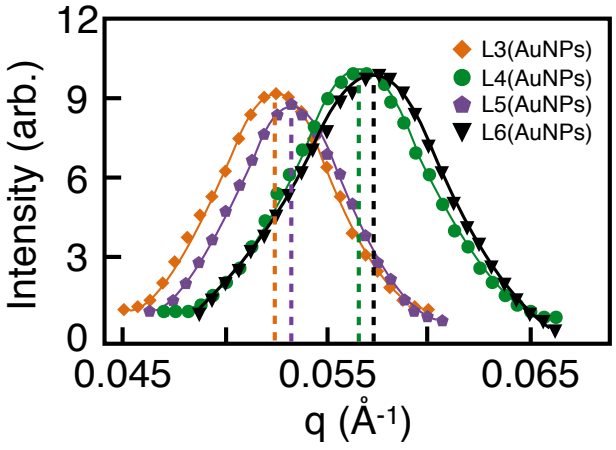

Figure 5.9: Small angle X-ray scattering (SAXS) data for AuNP microcapsules with ligand L3, L4, L5, and L6.

Ligand L1 and ligand L3 have the exact same numbers of carbons in both flexible-arm sides, 6 carbons on the right and 8 carbons on the left. Even though L1 has 5 more carbon atoms than L3 in the rigid side of the segment, there are only 0.1 nm differences in interparticle distance (Figure 5.10). Equivalently, 11.71 nm, the purple peak, from L5 ligands and 10.82 nm, the black peak, from L6 ligands were verified from the Figure 5.9 and the difference of average particle spacing from L5 and L6 was 0.89 nm.

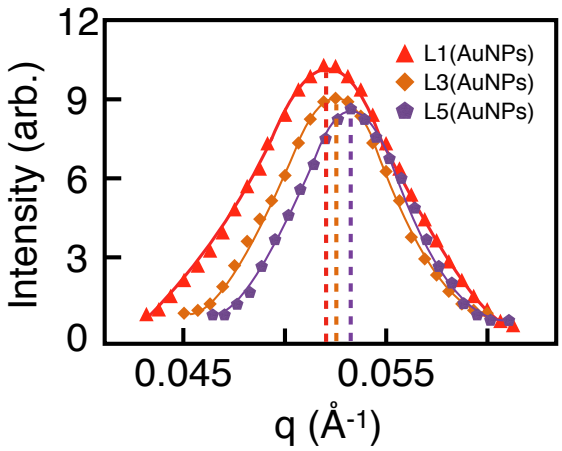

Figure 5.10: SAXS data for AuNP microcapsules with ligand L1, L3, and L5. Average interparticle distance between L1-L3, L3-L5, and L1-L5 were 0.1 nm, 0.27 nm, and 0.37 nm respectively.

Similar to ligand L1 and L3, ligand L2, L4, and L6 have the same length of alkyl chains in both side of the flexible segments. In the rod-like segment, L2 has 5 more carbons and 7 more carbons than L4 and L6 respectively. However, interparticle space difference between L2 and L4 was 0.17 nm (Figure 5.11). Additionally, Figure 5.11 indicated that 0.32 nm particle-particle space difference was created from L2 and L6. Compared with the space different between AuNPs in L1-L2 (0.94 nm), L3-L4 (1.01 nm), and L5-L6 (0.89 nm), L2-L6 had approximately three times longer alkyl (carbon) chain lengths and showed one third of their interparticle space differences. These results clarified that the alkyl chain lengths of flexible segment with amine (-NH_2) group affected particle packing structures more than a rigid rod-like segment.

Based on these results, we hypothesized a change in the length of an alkyl chain (a flexible segment) without amine group also influenced on interparticle distance of AuNPs. To investigate this hypothesis further, we carried out our SAXS experiments for determining a detailed packing structural characterization by controlling alkyl chain lengths of 6 more different ligands in our desired system (Figure 5.6). All ligands from L7 though L12 have 5 carbon-alkyl-chains in the left side of the flexible segments.

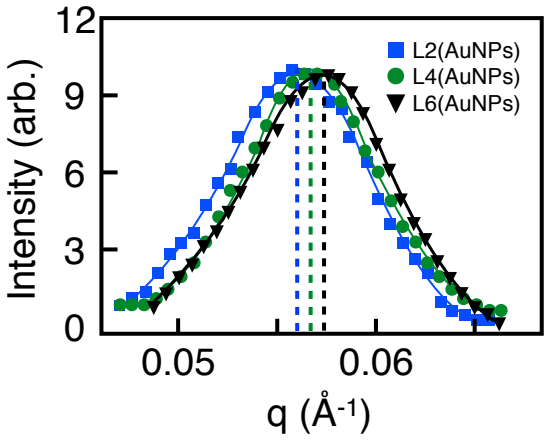

Figure 5.11: SAXS data for AuNP microcapsules with ligand L2, L4, and L6. Mean interparticle space between L2-L4, L4-L6, and L2-L6 were 0.17 nm, 0.15 nm, and 0.32 nm respectively.

The right side, having amine group, of the flexible segment has three varieties of carbon-alkyl-chains, such as 8 carbons for L7 and L8, 3 carbons for L9 and L10, and 1 carbon for L11 and L12 (Figure 5.6). Similarly, the rigid rod-like segment has also the same 3 variety of carbon-alkyl-chains, such as 8 carbons for L7 and L8, 3 carbons for L9 and L10, and 1 carbon for L11 and L12 (Figure 5.6). The pink broad peak, L7 ligands, at q= 0.0544 $\mathring{A}^{-1}$ in the Figure 5.12 illustrated 11.55 nm average spacing between AuNPs. This interparticle distance fell into between L1 and L2 values. AuNPs functionalized with ligand L8 had the shorter flexible alkyl chain lengths and produced a closer packing structure, 10.67 nm.

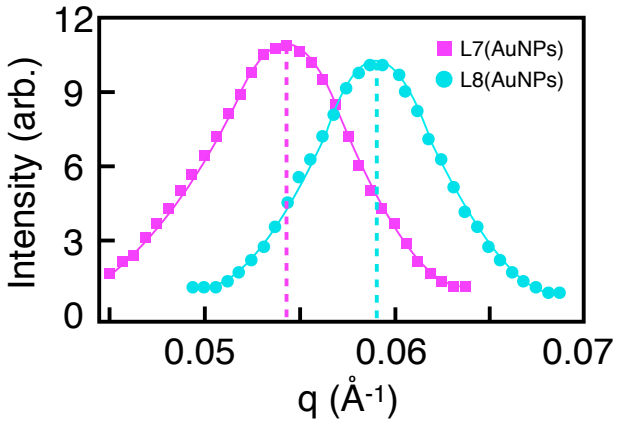

Figure 5.12: SAXS data for AuNP microcapsules with ligand L7 and L8.

When we compared the particle spacing between L1 and L7, the difference was 0.53 nm (Figure 5.13). L1 and L7 posses the same numbers of carbon chains in the right side of the flexible-arm and the rigid segment. In the left flexible segment, L7 has 3 carbons shorter chains than L1. Correlating particle-particle space displacement from L1-L7 with L1-L2 and L7-L8, where L2 and L8 showed 3 shorter alkyl chains in right flexible segment, L1-L2 and L7-L8 had roughly 0.40 nm more difference than L1-L7 (Figure 5.13). Furthermore, our experimental results of interparticle space differences between L2 and L7 demonstrated that L7 had 0.41 nm looser packing than L2 even though L2 and L7 carry the same total number of carbons in entire flexible segments (Figure 5.13). Specifically, L2 has 3 carbons in the right and 8 carbons in the left, and L7 contains 6 carbons in the right and 5 carbons in the left. Hence, the less number of carbon chains in right flexible segment leads close-packing structure of our AuNP microcapsules.

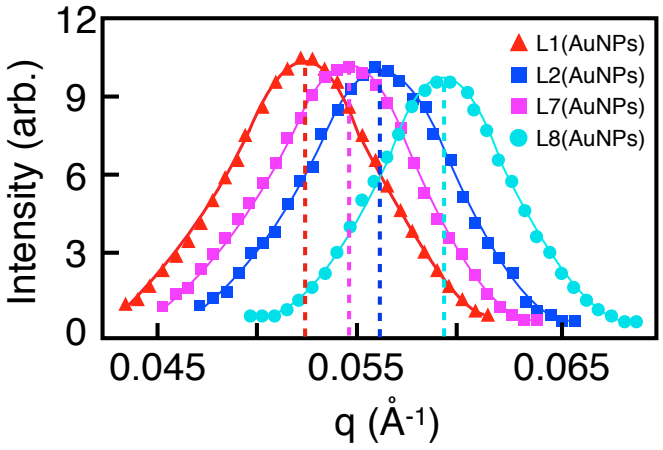

Figure 5.13: X-ray scattering data for AuNP microcapsules with ligand L1, L2, L7, and L8.

Figure 5.14 illustrated that AuNPs with L9, L10, L11 mesogenic ligands depicted 11.39 nm, 10.52 nm, 11.25 nm respectively. Additionally, the shortest lengths of alkyl chains in flexible segment with and without amine group, L12, showed the closest average interparticle distance 10.33 nm. Furthermore, comparison among L3-L4-L9-L10 (Supplementary Figure 5.17) and L5-L6-L11-L12 (Supplementary Figure 5.18) also proved the similar arguments and conclusions with L1-L2-L7-L8 cases discussed above.

These experimental results also denoted that lengths of alkyl chains in flexible segment without an amine substituent showed less effective for particle-packing condition than the segment with amine group. Hence, average interparticle spacing can be controlled by adjusting alkyl chain lengths in flexible segments with and without amine (-NH_2) substituent. Most effective alkyl chain components was the flexible segment with amine group. We

could observe that number of alkyl chains in the rigid rod-like segment slightly affect the particle packing space, however no significant test results of densely-packed nanoparticle arrangements were shown.

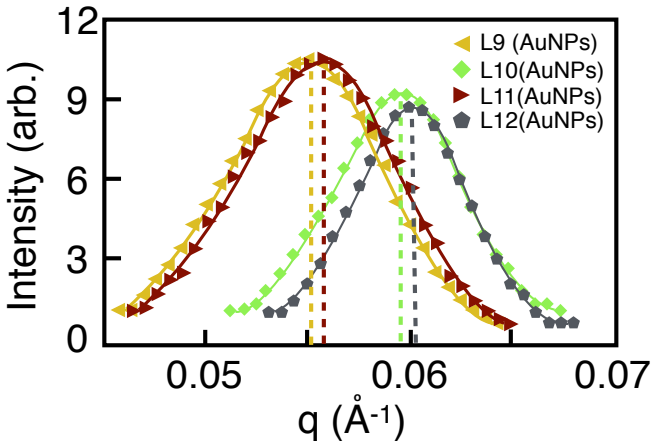

Figure 5.14: X-ray scattering data for AuNP microcapsules with ligand L9, L10, L11, and L12.

5.4 Conclusion

We discovered a new methodology for the formation of self-assembled nanoparticle microcapsules. The microcapsules, constructed on mesogen-functionalized nanoparticles, were templated at the isotropic to nematic phase boundary in a liquid crystal host media. Size control of microcapsules were carried out by changing cooling rate of NPs-LC media and tuning their packing structure was achieved by varying ligand design by modifying lengths of alkyl chain of flexible segments in mesogenic ligand structures.

Since these parameters were independent of particle type, the process could be easily adapted for use with any appropriately-sized nanoparticles, including mixtures of metallic, semiconducting and magnetic particles. This new method will open up a new door for metamaterial, photonics,and bio-engineering fields. The discovery of 3D self-assemblies microcapsules was templated by the phase separation of nanoparticles-rich and nanoparticles-poor domains in LC host media during LC isotropic-nematic phase transition. We determined spherical morphology achieved by controlling specific nanoparticle concentration and the detailed the cooling process.

Additionally, interparticle packing was tunable by varying ligand design by changing flexible attachment arm-length. These parameters did not depend on particle types, and the process could therefore be easily used for any variety of NPs, any appropriately-sized

nanoparticles, and any mixture of different NPs. Sorting NPs into micron-scale 3D structures is typically a challenge, however we are now able to introduce new template for forming microcapsules in fluid-based systems. In the next chapter, we will discuss more about our multifunctional gold nanoparticle microcapsules for controlled-release and encapsulation applications.

5.5 Supplemental figures

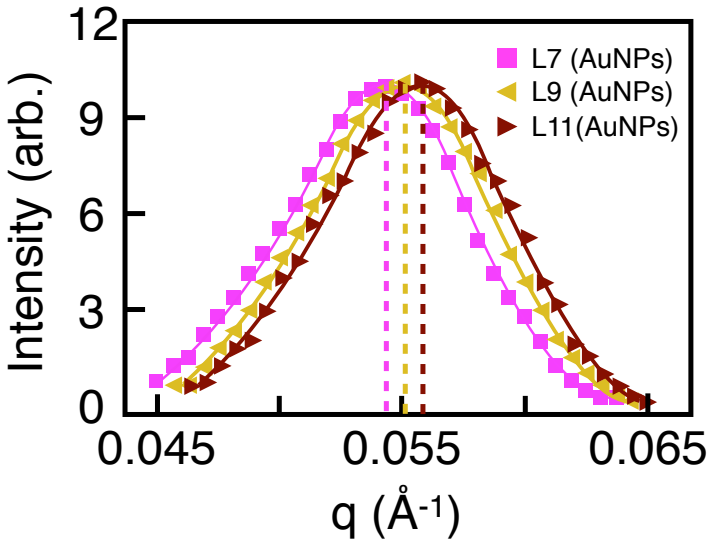

Figure 5.15: SAXS data for AuNP microcapsules with ligand L7, L9, and L11. Mean interparticle space between L7-L9, L9-L11, and L7-L11 were 0.16 nm, 0.14 nm, and 0.32 nm. These values represented varying alkyl-chain lengths of the rigid segment was less effective for controlling particle-particle distance.

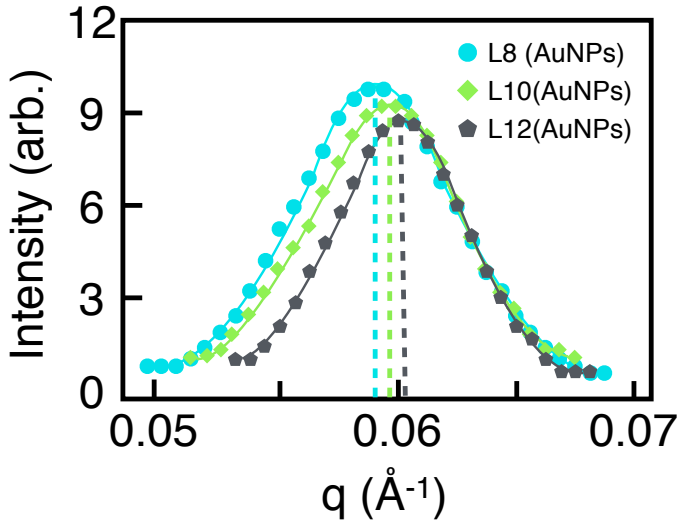

Figure 5.16: X-ray scattering data for AuNP microcapsules with ligand L8, L10, and L12. Average particle-particle displacement between L8-L10, L10-L12, and L8-L12 were 0.15 nm, 0.19 nm, and 0.34 nm respectively. The results also represented that changing number of carbon atoms in the rigid segment was less influenced for controlling nanoparticle packing than the varying the alkyl-chain lengths of flexible-arm segments

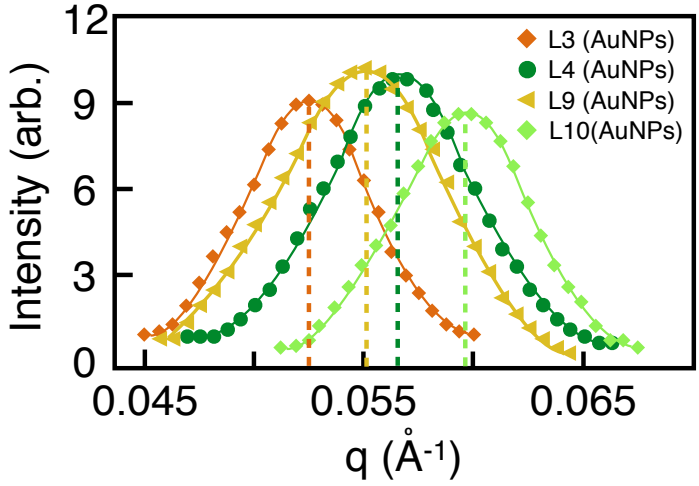

Figure 5.17: X-ray scattering data for AuNP microcapsules with ligand L3, L4, L9, and L10. Average particle-particle displacement between L3-L9 and L4-L10 were 0.59 nm and 0.45 nm respectively. The mean particle space difference between L4 and L9 was 0.42 nm. This represents mean separation between AuNPs with L9 ligands had larger separation displacement than AuNPs with ligand L4.

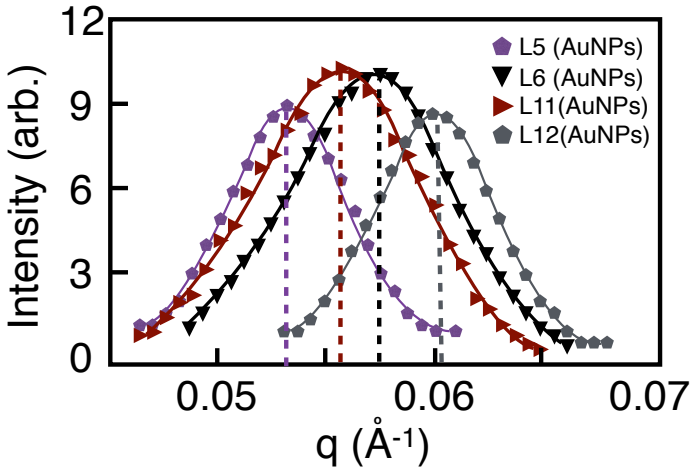

Figure 5.18: X-ray scattering data for AuNP microcapsules with ligand L5, L6, L11, and L12. Average particle-particle displacement between L5-L11 and L6-L12 were 0.46 nm and 0.49 nm respectively. The mean interparticle space difference between L6 and L11 was 0.43 nm. This represents mean separation between AuNPs with L11 ligands had larger separation displacement than AuNPs with ligand L6.

Chapter 6

Plasmon-actuated nano-assembled gold microshells

In this chapter, I present three-dimensional gold microshells formed by self-assembly of densely-packed 5 nm gold nanoparticles (AuNPs). Surface functionalization of the AuNPs with custom-designed mesogenic ligands drives the formation of a stable and rigid shell wall, and these unique structures allow encapsulation of cargo that can be contained, virtually leakage-free, over several months. Further, by leveraging the plasmonic response of AuNPs, we can rupture the microshells using optical excitation with ultralow incident power (< 2 mW), controllably and rapidly releasing the encapsulated contents under 5 seconds. The optimal AuNP packing in the wall, moderated by the custom ligands and verified using small angle x-ray spectroscopy, allows us to calculate the heat released in this process, and to simulate the temperature increase originating from the photothermal heating with great accuracy. Atypically, we find the local heating does not cause a rise in excess of 50 ^{0}C, which addresses a major shortcoming in plasmon actuated cargo delivery systems. This combination of spectral selectivity, low power requirements, low heat production, and fast release times, along with the versatility in terms of identity of the enclosed cargo, makes these hierarchical gold microshells suitable for wide-ranging applications. Most interestingly, the applicability of our gold microshells also includes biological ones.

6.1 Introduction

Research involving nanomaterials has brought to light their intriguing electronic, magnetic and optical properties, so different from the bulk counterparts [133–137]. Amongst these, metallic nanoparticles are of particular interest, given their ability to modulate light-matter interactions by manipulating electromagnetic fields through localized surface plasmon resonances (LSPR) [138]. Plasmonic phenomena have found use in numerous ap-

plications, including biochemical sensing [139, 140], biomedical diagnostics and therapy [141–143], high-resolution optical imaging [144, 145], optical switching [2], photovoltaic devices [146, 147], energy storage [148, 149] and photocatalysis [150]. Gold nanoparticles (AuNPs) have LSPR in the visible to near-infrared spectral region and is therefore the most popular candidate in typical applications, though silver, aluminum and platinum are studied as well [151–153]. In order to fully exploit plasmonics and reliably and design reliable devices with consistent performance, research efforts have been focusing on developing ordered assemblies of plasmonic nanosystems. These include both top-down and bottom-up approaches, but the latter has greater advantages in terms of versatility of geometry, architecture and functionality. Assemblies of colloidal AuNPs have achieved range from simple dimers and trimers [145] to nanoclusters [154], from one dimensional chains [155] to networks [156]. Recently, novel arrangements such as core-satellite structures have also been assembled [157, 158] and these offer the added convenience of heterogeneous formations. The process of assembly is directed via linkers with which AuNPs are functionalized, and those that have demonstrated the most success include DNA molecules [14], organic ligands [159] and linear [160] and branched polymers [145].

Moving beyond assembly, the next capability that would greatly enhance the functionality of these assemblies is responsiveness to external stimuli. Tuning the spectral position of the LSPR in situ is one approach, usually achieved by modulating the dielectric constant of the medium surrounding the AuNPs [161, 162]. The other is utilizing the photothermal effect, where resonant optical excitation is absorbed by the AuNPs, which heats the crystal lattice, in turn transferring the heat to the surrounding medium. This phenomenon has potential application in targeted drug delivery, and such systems with release mechanisms that can be remotely triggered using stimuli such as electric and magnetic fields, as well as optical excitation, have been the subject of extensive research [163–170]. In case of optical actuation, the power, wavelength, and duration of incident light required is strongly dependent on the components used for construction of the capsule. And while it is critical for the capsules to provide robust leakage-free containment, the excitation power used to trigger release must be below the American National Standards Institute (ANSI) maximum permissible exposure limit. For visible excitation at $\sim$500 nm, this limit is 2.5 mW for up to 10 min of illumination [5]. Optimizing these parameters simultaneously is challenging. One approach using silica-gold core-shell composite NPs for encapsulation and light-activated release utilizes 15-100 mW of illumination over tens of minutes [163]. AuNP-assembled nano-micelles and cross-linked nano-vesicles can release contents in under 10 min of excitation, but require higher powers (100-250 mW) [164]. With few exceptions [165], composite structures and complexes that combine AuNPs with soft materials such as polymers, gels, and liposomes have lower power requirements (10-65 mW) at the cost of longer release times (10-40 min) [166]. Other methods using AuNP-DNA complexes [167] or rare-earth NPs require power on the order of 1 W [168].

We present a liquid crystal phase-templated mechanism using AuNPs functionalized

with mesogenic (liquid crystal-like) ligands [3, 132] that produces nano-assembled microshells (NAMs) 1-5 μm in diameter with closely spaced nanoparticles constituting the shell wall, schematically represented in Figure 6.1 (a). Using plasmon actuation via shining light of wavelength close to the AuNP LSPR, we show that cargo encapsulated within the NAM can be released in a spatially controlled manner, where localized heating breaks the shell wall via the photothermal effect. In contrast to most other techniques, our mechanism does not require the fabrication of multicomponent capsules, simplifying the synthesis and cargo encapsulation processes. Moreover, the rigidity of the shell wall ensures leakage-free containment over months.

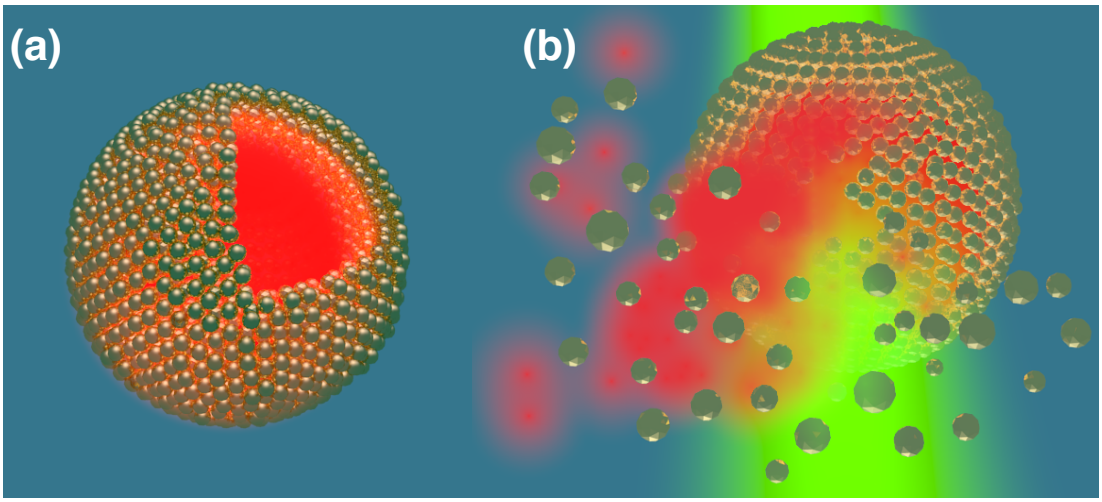

Figure 6.1: Schematic of (NAM) (a) An intact structure with sectional cut-out shows the encapsulated dye within. The wall is multiple layers thick. (b) Illumination by green light, resonant with the localized surface plasmon resonance (LSPR) of the nanoparticles in the wall, disrupts the structure due to photothermal heating, releasing the contents within. (Reprinted from reference [4] with permission from Macmillan Publishers Ltd. ©2017.)

The NAMs were robust to leakage even when the shells were extracted from the native host and re-suspended in other solvents. Our NAMs are activated using < 2 mW of incident power, and full release is obtained within 1-5 s (Figure 6.1 (b)). These data are by far the most optimized combination of power requirement and release time reported, and is made possible by the ideal packing of AuNPs achieved in the shell wall. The inter particle spacing, controlled by the length of ligands, allows the walls to have a high enough density of particles to allow low power requirements, and therefore rapid release times. However, the spacing is larger than what is needed for strong inter particle coupling, which in turn permits an accurate estimate of the temperature increase due to the photothermal effect.

Our calculations are verified by comparison with experimental quantification of bubble expansion rates, and indicate a most moderate rise of 50 ^{0}C, which is a significant step toward the realization of photothermally activated capsules with a broad range of applications in cargo encapsulation and delivery protocols.

6.2 Experimental methods

6.2.1 Ligand synthesis

Our organic ligand exhibits thermotropic liquid crystalline behavior. When heated, it transitions from a smectic to nematic, and then from a nematic to isotropic phase, as observed in Figure 6.8. Our functionalized ligands are designed to possess both rigid and flexible segments. The rigid segment, which contains a mesogenic group, contains a relatively rigid rod-like structure. The flexible segment is composed of a long alkyl chain with or without an amine group; the presence of an amine substituent on the chain allows the ligand to attach to the surface of gold nanoparticles. Hence, the flexible segment provides free rotation and fluidity that encourages a close packing of NPs, as well as structural stabilization of our NAMs (Figure 6.2). The synthesis of the ligand (S8) is modeled on prior publications [3, 132] with improvements that are explained in detail in the supplemental information. The longest linear synthetic sequence consists of five steps (Figure 6.16).

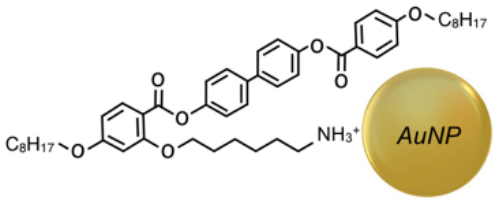

Figure 6.2: Schematic of mesogenic ligand attached to AuNP. (Reprinted from reference [4] with permission from Macmillan Publishers Ltd. ©2017.)

6.2.2 Microscopy and spectroscopic methods

Leica DM2500P microscope in the transmission mode with a Leica 63x (NA = 0.80) objective and a Q-image Retiga camera is mounted on the microscope. Polarized optical microscopy and Fluorescence microscopy (reflection) are also carried out on the same microscope. For fluorescence imaging of encapsulated dye, Lumogen F Red (BASF) with

a peak emission at 613 nm, we use a 515–560 nm band-pass filter with white-light mercury lamp illumination. Emission was detected using a 580 nm dichroic mirror and a 590 nm Long pass filter. Leica DM2500P microscope is used for bright field, cross-polarized, fluorescence images of the NAMs.

A scanning electron microscope, Zeiss Gemini SEM 500, instrument operating at 3kV and 10 kV was used to validate the size of individual NAMs or arrangement of the individual AuNPs in the shell wall. NAMs are extracted from the liquid crystal host and redispersed in chloroform after we formed shells in cooling the Liquid crystal-functionalized gold nanoparticle mixture from isotropic to nematic as described earlier. Extracted NAMs were pipetted on indium tin oxide (ITO) glass slides and dried the sample at 80 ^{0}C environment for 5 hours. The NAMs are imaged after chloroform is completely evaporated. Absorption spectral measurements for gold nanoparticles in chloroform are performed using a PerkinElmer UV/Vis spectrophotometer.

6.2.3 NAMs preparation

The mesogen-functionalized AuNPs (1.2 wt$\%$) were dispersed into nematic liquid crystal (NLC) 4-cyano-4'-pentylbiphenyl (5CB, Sigma Aldrich), which exhibits a nematic to isotropic transition at 35.5 ^{0}C. The NLC-AuNPs mixture was then sonicated in a 40 ^{0}C bath for 5 hours in an Eppendorf tube, allowing the NLC to remain in the isotropic phase while the solvent (chloroform) in which the AuNPs were suspended during functionalization gradually evaporated from the NLC. Solvent removal was verified by measuring the nematic-to-isotropic phase-transition point using a Perkin-Elmer differential scanning calorimetry, (DSC). We placed a microscope LC-AuNP mixture slide on a 40 ^{0}C maintained Linkham LTS350 hot-stage and verify the sample slide condition that has a great initial dispersion by using a Leica DM2500P upright microscope equipped with a Q-image Retiga camera. After achieving a homogeneous dispersion, the mixture was deposited onto a microscope slide mounted on a temperature-controlled Linkam LTS350 hot-stage and sandwiched with a cover slip. All slide and cover clip surfaces were pre-treated with cetyltrimetylammonium bromide (CTAB) or polyvinyl alcohol (PVA) to encourage homeotropic or planar alignment of the NLC molecules. As the NLC-AuNP mixture was cooled into the nematic phase (cooling rate 0.5 ^{0}C/s), it separated into NLC-AuNP-rich droplets and an NLC-rich phase. During this segregation, the functionalized AuNPs moved into the shrinking isotropic domains and shell formation was observed. Shell size is controlled by the cooling rate. Fast cooling (3 ^{0}C/s) resulted in the formation of shells with diameter $\sim$1 μm, while a slower rate (0.2 ^{0}C/s) produced shells as large as 5 μm.

6.2.4 Encapsulation of fluorescent dye

Lumogen F Red 300 (BASF), dissolved in toluene, was then added to the LC-AuNPs (1.2 wt$\%$) mixture to create concentrations of 2 mM composites. These mixtures are transferred into 1.5 mL Eppendorf tube and sonicated in the 40 ^{0}C bath for five hours. After verified complete evaporation of chloroform and toluene by using a DSC, we formed NAMs in the Eppendorf tube by transpiring the tube into a 30 ^{0}C maintained modular heating block (VWR). After NAMs are formed, the Eppendorf tube is centrifuged (8000 rpm for 30 min.) to concentrate at the bottom of the tube and the supernatant (LC-Lumogen F Red mixture) is discarded. Added 5CB and mixed with the precipitated NAMs in the Eppendorf tube. Repeat this process for 5 times before we image encapsulated dye in the NAMs.

6.2.5 Thermal stability experiment

Images of NAMs are carried out on Leica DM2500P microscope in transmission and fluorescent mode with a 63x (NA = 0.80) objective. Samples are placed on Linkham LTS350 hot-stage and are heated above the liquid crystal isotropic point ($\approx$ 35.5 ^{0}C) the ligand-ligand interaction continues to maintain a rigid spherical structure on slow heating (1 ^{0}C/min).

6.2.6 Disintegration and bubble expansion images of NAMs

Disintegration and bubble expansion images of NAMs are performed on a TIRF microscope built with a Ti-E Eclipse stand (Nikon Instruments). The objective used is an Apo TIRF 100X (NA = 1.49). CUBE diode 405 nm laser (Coherent), Sapphire OPSL 488 nm, 514 nm, and 561 nm lasers (Coherent), and OBIS 647 nm (Coherent) are combined into a fiber optic cable and into a TIRF illuminator (Nikon) attached to the microscope stand (Figure 6.3). Shuttering of the laser illumination is controlled by an acoustooptic tunable filter, AOTF, (AA Optoelectronics) before the fiber coupler (Figure 6.3). Disintegration images are acquired with an iXon3+ 887 EMCCD (Andor Technology) camera and bubble expansion images are taken by a high-speed camera (Fastec Imaging). Synchronization between these components was achieved using μManager [171] with a microcontroller (Arduino). We image the disintegration and bubble expansion of the NAMs by exposing sample slides to each activation (405, 488, 514, 561, 647 nm) with incident laser power at 0.5, 0.75, 1, 1.5, and 2 mW in a temperature controlled chamber (HaisonTech) at 25 ^{0}C. For bubble expansion images, the time and information of the bubble size are exported to Morphometric and Matlab program files for further data analysis and plotting purpose.

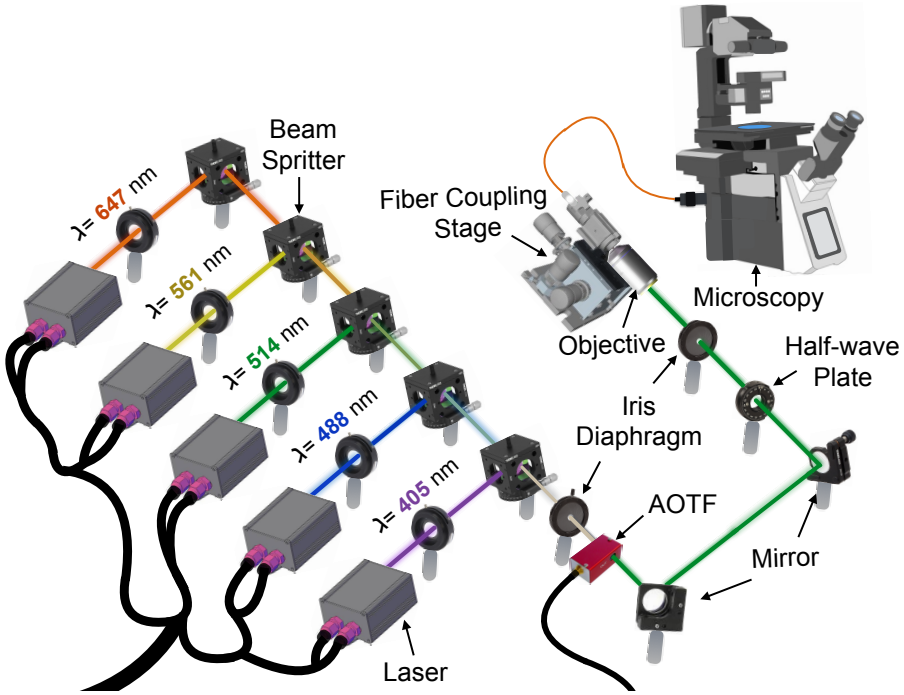

Figure 6.3: Schematic of experimental set-up.

6.2.7 Small angle X-ray scattering method

Small angle X-ray scattering (SAXS) measurements are carried out at the Stanford Synchrotron Radiation Laboratory, beamline 4 – 2. Liquid crystal-NAMs mixtures were prepared 24 hours before measurements were taken. The sample mixtures are transferred into 1.5 mm quartz X-ray capillaries at the beamline. The capillaries were mounted in transmission configuration using a custom chamber. Measurements were carried at 11 keV for 1 second per exposure. Diffraction patterns are recorded on a CCD detector, then plotted as integrated intensity as a function of q, the scattering vector using the custom Sastool analysis software at the beamline.

6.2.8 Thermal map simulation

The temperature of NAMs were analytically calculated using Matlab computing software. Nanoparticles were randomly arranged in a sphere with an average distance of 12 nm between them and the thickness of the shell being $\sim$160 nm (20 $\%$). The total change in temperature due to the ensemble can be calculated by summing $\triangle$T over all the nanoparticles. We use an intensity of 10^7J/m^2 for the incoming light assuming an average absorption of 1 $\%$, attributed to shielding of the inner layers and other losses.

6.3 Results and discussion

6.3.1 Imaging-based characterization

Careful choice of mesogenic ligand-functionalized AuNPs dispersed in an anisotropic host phase (such as a liquid crystal) provides an excellent route toward directed assembly in our approach. A rigid mesogenic segment built into a long-chain hydrocarbon molecule can align with the surrounding host phase, decreasing the free-energy cost of dispersing AuNPs in the host (Figure 6.2). The procedure of ligand synthesis and AuNP functionalization followed our prior work [3, 132]. The host phase in this case is the nematic liquid crystalline (NLC) phase, where the LC molecules possess orientational order labeled by the director axis, but not long-range positional order. We monitored shell formation as the process occurred using bright-field microscopy. Figure 6.4 (a) is a snapshot of one NAM taken as the shell formation is complete. Shell morphology and structure using polarized optical microscopy (POM) and scanning electron microscopy (SEM). The inherent anisotropy of LC molecules makes them birefringent, and under POM, the relative orientation of the director axis with respect to the crossed-polarizers in the microscope determine the intensity of the transmission images.

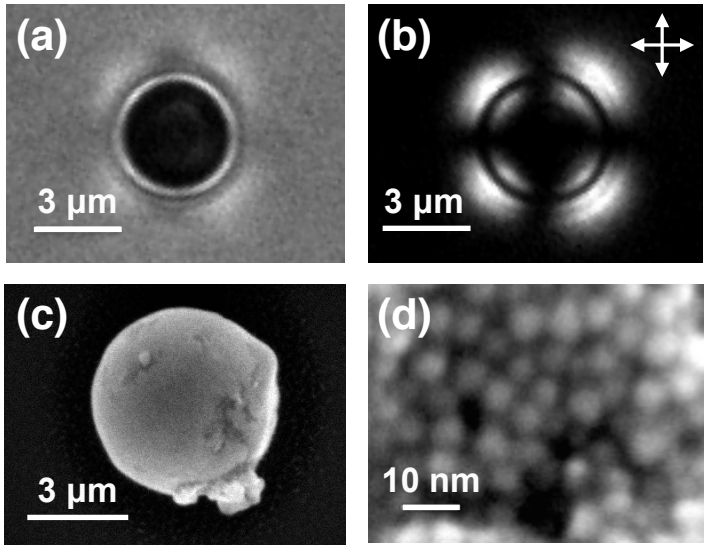

Figure 6.4: (a) Bright-field and (b) cross-polarized images of a NAM in liquid crystal medium. (c) SEM image of a NAM extracted from suspension and placed on an indium tin oxide coated glass slide. (d) Close-up of the same structure in (c), showing individual AuNPs that form the wall.(Reprinted from reference [4] with permission from Macmillan Publishers Ltd. ©2017.)

In our case, the director, was aligned perpendicular to the plane of the sample, which is known as homeotropic alignment, which should make the NLC film appear dark under POM. In Figure 6.4 (b), this is the case away from the NAM. Closer to the shell wall however, the POM images showed a radially contrasting pattern. When spherical objects such as these are dispersed in a homeotropically aligned NLC, their surfaces induce director distortions [172], and adjacent LC molecules acquire a different orientation compared with the director of the bulk of the film. The NAMs presented in this work exhibit planar surface anchoring as reported in our previous [3] and other [172] studies with local LC molecules orienting parallel to their spherical surface. As a result, the birefringence image in Figure 6.4 (b) exhibits the characteristic cross pattern between crossed polarizers and is a confirmation of the three-dimensionality of the shells. Using SEM, we observed shells post-extraction from the host NLC (Figure 6.4 (c)), which leads to a slight deformation. Higher resolution SEM showed a densely-packed arrangement of the individual AuNPs in the shell wall (Figure 6.4 (d)), and small angle X-ray scattering (SAXS) indicated that the mean inter-particle separation of the AuNPs in the wall is 12.1 nm (Figure 6.5). This configuration turns out to be optimal for our purposes as this high AuNP density is critical to allow rapid actuation via low power.

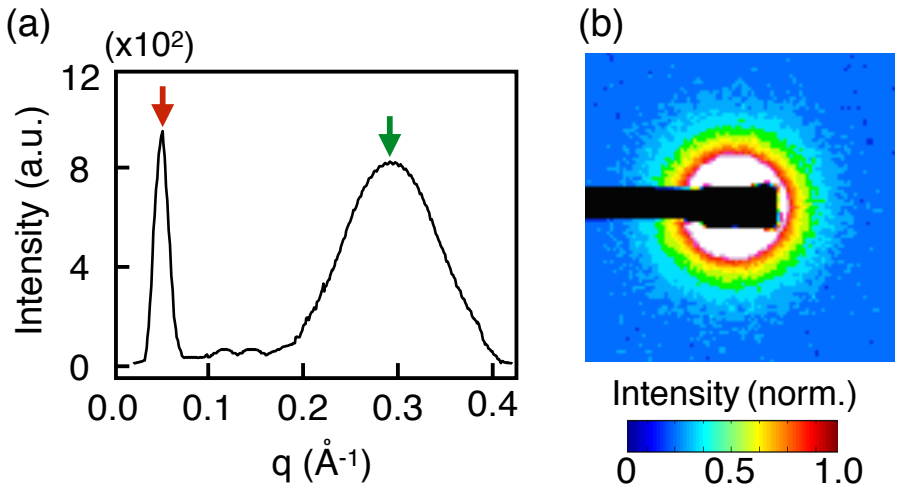

Figure 6.5: Small angle x-ray scattering (SAXS). (a) Red arrow shows the scattering peak from the functionalized AuNPs while the broader peak (green arrow) at longer scattering vector is from the 5CB molecules. The smaller q of 0.05 $\mathring{A}^{-1}$ corresponds to a separation of 12.1 nm. (b) Representative two-dimensional SAXS pattern from functionalized AuNPs. The colour scale corresponds to the normalized scattering intensity. (Reprinted from reference [4] with permission from Macmillan Publishers Ltd. ©2017.)

6.3.2 High containment capability

For encapsulation within the NAMs, we used Lumogen F Red 300 (BASF), a dye with a high quantum yield. We dissolved the dye in toluene and added the dye to the NLC-AuNP mixture. Following sonication and shell formation, we spun down the NAMs with a centrifuge (8000 rpm for 30 min), discarded the supernatant, and re-suspended the dye-containing NAMs in dye-free NLC. We repeated the process five times until we achieved a clear contrast between the shells containing Lumogen F Red and the host NLC (Figure 6.6 (a)-(c)). We imaged the sample using epifluorescence microscopy after each centrifugation step to ensure that the shells remained undamaged.

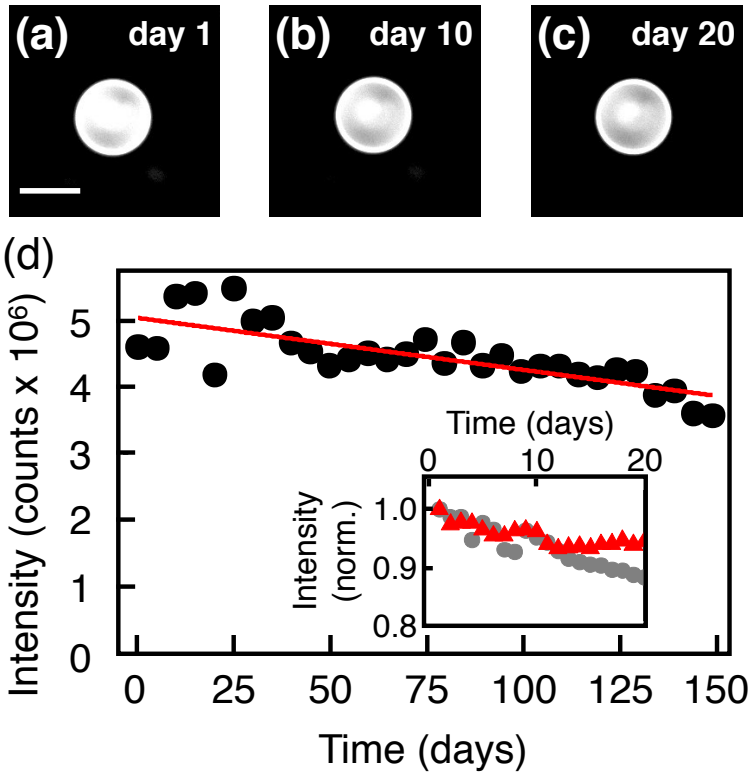

Figure 6.6: NAMs exhibit little to no leakage over many months. (a-c) Fluorescence images of Lumogen F Red encapsulated in a NAM. Scale bars: 1 μm. (d) Dye intensity measured over five months. Inset: dye intensity encapsulated in shells compared to that of dye suspended in liquid crystal alone. The quantitative agreement between the two over the first $\sim$10 days indicates that the small decrease is likely due to photo bleaching. (Reprinted from reference [4] with permission from Macmillan Publishers Ltd. ©2017.)

To quantify the stability of encapsulation in NAMs, we measured the Lumogen F Red fluorescence intensity, as a proxy for the dye concentration in the NAMs, over 5 months. At each time, we deposited the NAMs onto a glass slide, overlaid the slide with a cover slip, and sealed the edges with wax to minimize changes in the sample due to the diffusion of oxygen and water. Visually, we observed a small decrease in the emission with time, $\sim$20 $\%$ over 150 days (Figure 6.6 (a)-(c)), and the spatially integrated fluorescence intensity exhibited linear quenching (Figure 6.6 (d)). Compared with most dyes, Lumogen F Red is a highly stable emitter, although it does display a small degree of photo bleaching [173]. A control with Lumogen F Red dispersed in NLC and imaged under identical conditions for 10 days demonstrated that photobleaching is a small but significant factor in quantifying the evolution of intensity of Lumogen F Red in our experiments (Figure 6.6 (d), inset). In fact, after 10 days, encapsulation in the NAM appeared to reduce the effects of photo bleaching compared to the dye in the bulk NLC in our control. We thus conclude that Lumogen F Red remains stably encapsulated in the NAM for at least 5 months with minimal to no leakage, testifying to the high containment capability of our structures.

6.3.3 Plasmon actuation

To explore the thermal stability of the shells, we monitored the fluorescence of a shell containing Lumogen F Red while the sample was heated on a temperature-controlled Linkam stage at 1 ^{0}C/min, beginning at 25 ^{0}C, shown in Figure 6.7.

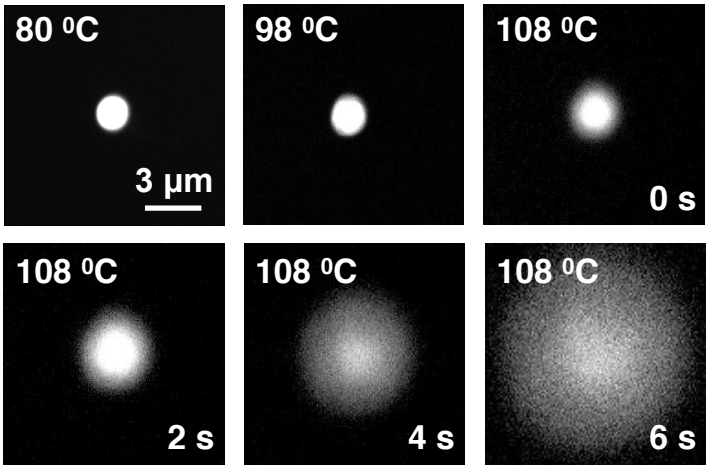

Figure 6.7: Fluorescence microscopy images of a NAM loaded with a fluorescent dye on a temperature-controlled stage. The temperature was increased from 80 to 108 ^{0}C, and the time after reaching 108 ^{0}C is given in the lower right corner. (Reprinted from reference [4] with permission from Macmillan Publishers Ltd. ©2017.)

The shell structure remained unchanged up to a temperature of 98 ^{0}C. Note that the NLC transitions to its isotropic phase at 35.5 ^{0}C, demonstrating that the shells, once assembled, can survive transitions of the host medium. At 98 ^{0}C, the shell began to deform slightly. At 108 ^{0}C, the rigid shell disintegrated and the dye leaked out, with the structure completely collapsing within 6 s. Differential scanning calorimetry (DSC) studies confirmed that the mesogenic molecules exhibit a crystalline-to-nematic transition around 76 ^{0}C and a transition to isotropic at $\sim$132 ^{0}C (Figure 6.8). We propose that this massive structural change of the shell was likely caused by weakened interactions between the ligand molecules as the ligands transitioned to the isotropic state. The lower apparent transition temperature (compared to the 132 ^{0}C measured using DSC) can be attributed to the presence of AuNPs.

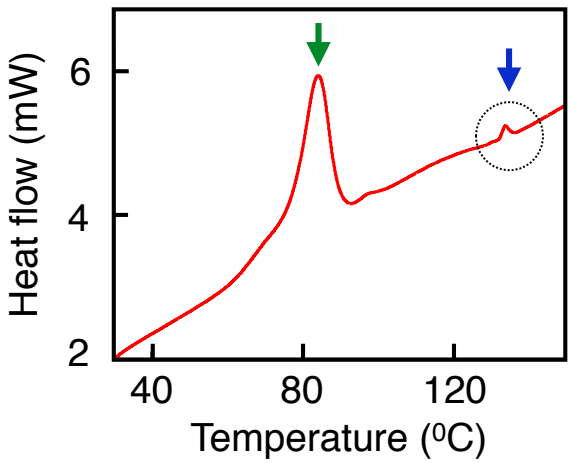

Figure 6.8: Differential scanning calorimetry (DSC). The mesogenic ligand shows two peaks in the heating cycle. The first peak at 84 ^{0}C denotes a crystalline to nematic-like phase transition, while the second peak (circled) at 134 ^{0}C is a nematic to isotropic transition. (Reprinted from reference [4] with permission from Macmillan Publishers Ltd. ©2017.)

Having confirmed that the NAMs can be destroyed through thermal perturbations and their enclosed cargo released, we sought to trigger release though LSPR-mediated stimuli. We illuminated the NAMs with a 488-nm laser at a power of 2 mW at room temperature, and acquired a series of bright-field images at an interval of 5 s to monitor the structure of the shell (Figure 6.9 (a)). After approximately 3 s of illumination, the shell began to disintegrate, and by 5 s it had collapsed completely. Simultaneous fluorescence imaging

confirmed that the encapsulated dye leaked out within 2 s of illumination (Figure 6.9 (b)), and was released entirely after 5 s.

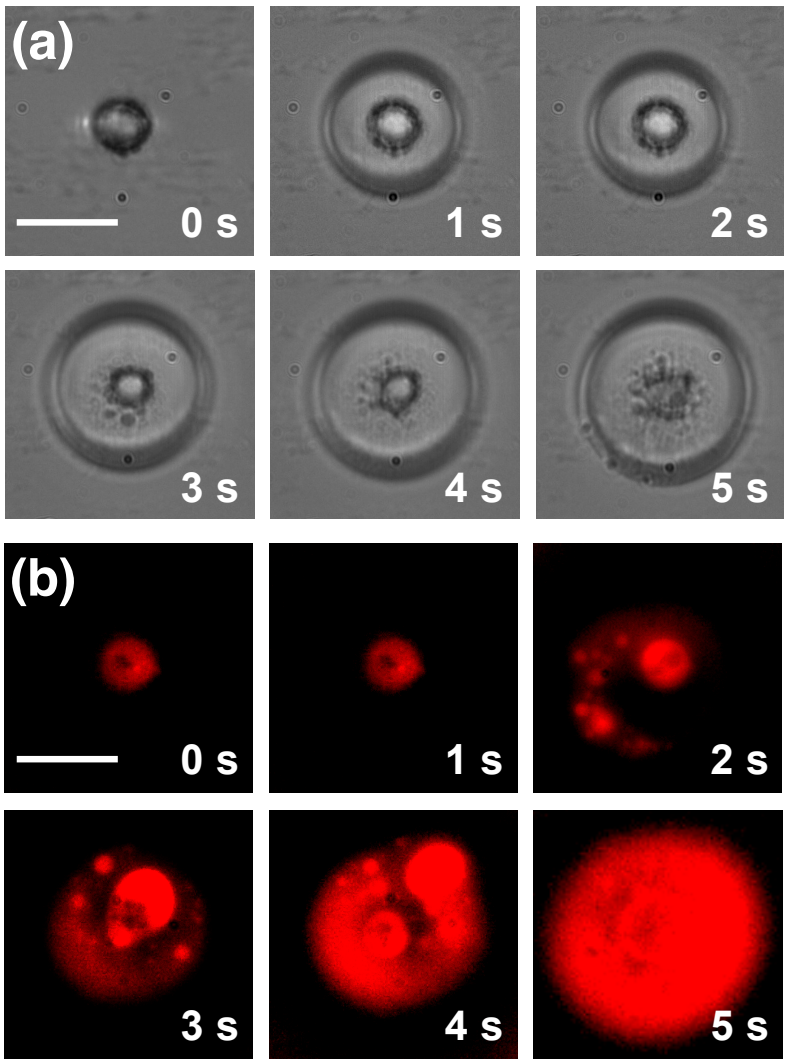

Figure 6.9: Actuation leading to release of contents from a NAM. (a) Bright-field and (b) fluorescence time-lapse images during plasmon-actuated shell disintegration. The encapsulated dye is released during 5 s of illumination with 2 mW of incident power. Scale bars: 3 μm. (Reprinted from reference [4] with permission from Macmillan Publishers Ltd. ©2017.)

We characterized the release time, τ, as a function of incident power for different excitation wavelengths (Figure 6.10 (a)). As expected, we observed the fastest response for excitation at 514 nm (Supplementary Figure 6.14), which is closest to the LSPR (520 nm). For the highest incident power (2 mW), release was extremely rapid (τ = 1.2 s). More importantly, release within 2 min was achieved with power as low as 0.5 mW. Furthermore, the NAMs responded to slightly off-resonant light (488 and 561 nm) almost as well, with τ ranging from $\sim$ 6 s to 5 min with varying incident power (Supplementary Figure 6.15), increasing the responsive spectral band to $\pm$40 nm around the LSPR. Tuning the excitation wavelength farther away failed to elicit any response even at higher powers; this spectral selectivity is attractive, as it allows targeting of specific NAMs based on the size of AuNPs constituting the shell wall.

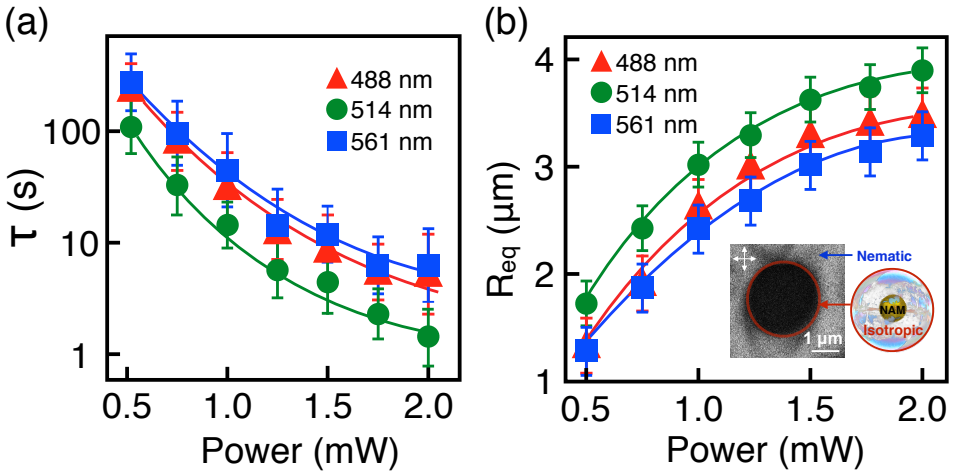

Figure 6.10: (a) The release time τ decreases with increasing power for three different excitation wavelengths; the fastest release is achieved at 514 nm, which is the wavelength closest to the LSPR (520 nm). (b) The equilibrium bubble radius R_{eq} increases with increasing power, and is largest at 514 nm. Inset: Cross-polarized image of the bubble shows isotropic phase (dark) inside and nematic phase outside. (Reprinted from reference [4] with permission from Macmillan Publishers Ltd. ©2017.)

6.3.4 Modeling the photothermal heating

We noted in our time-lapse imaging of shell disintegration (Figure 6.9 (a)) that after 1 second a bubble had formed around the shell. Bubble formation around metallic NPs due to optical excitation is a consequence of the photothermal effect, caused by the local temperature increase inducing a phase transition of the surrounding host medium [174–177].

AuNPs suspended in water are known to produce steam under laser irradiation, and even with sunlight [178]. In our case, POM images confirmed that the temperature increase on and near the shell surface drives a transition in the surrounding NLC from the nematic to isotropic phase, which is what constitutes the bubble (Figure 6.10 (b), inset). The NLC outside remains in the nematic phase, with the bubble radius demarcating the phase boundary. We sought to use the dynamics of the expanding phase boundary as it approached equilibrium to infer the heat flux that propagates through the surrounding medium [177, 179], and more importantly, estimate the resultant increase in temperature. High temperatures from the photothermal effect would suggest that the plasmon-actuated mechanism could result in damage to thermally-sensitive encapsulants or biological materials, nullifying any other benefits the platform could provide. We start by considering the conduction of heat through the liquid crystalline medium. The primary heat source is supplied by the laser incident on the NAM and is assumed to only induce plasmonic heating without affecting the surrounding liquid crystal directly. The time-dependent temperature distribution around the shell is then determined by the solution to the heat equation. For a spherical heat source of fixed radius and strength, $\dot{Q_{in}}$, the explicit time dependent solution for the temperature as a function of radial distance from the center of the shell, $T(r)$, can be expressed in terms of error functions [180], which for late times, can written to leading order in the reciprocal of time t as:

$$\frac{4\pi\kappa_{LC}(T(r)-T(\infty))}{\dot{Q_{in}}} = \frac{1}{r} - \frac{1}{\sqrt{\pi\beta t}} \tag{6.1}$$

with $\beta = \frac{\kappa_{LC}}{\rho_V C_p}$, where κ_{LC} is the thermal permeability of the liquid crystal, ρ_V is the LC density, C_p is the specific heat, and $T(\infty)$ is the ambient temperature far from the shell. Extracting $\dot{Q_{in}}$ is critical for estimating the temperature distribution near the NAM, as there is no direct route of measuring the heat supplied to each shell. Note that the steady-state solution at infinite time is given by:

$$T(r) = T(\infty) + \frac{\dot{Q_{in}}}{4\pi\kappa_{LC} r} \tag{6.2}$$

For simplicity, we ignore the small amount of latent heat associated with the phase change. The location of the phase boundary at infinite time, i.e. the equilibrium bubble radius R_{eq} is determined by the value of r at which $T(r)$ is at the nematic-isotropic critical temperature T_{NI}, and is therefore given by

$$R_{eq} = \frac{\dot{Q_{in}}}{4\pi\kappa_{LC}[T_{NI} - T(\infty)]} \tag{6.3}$$

The location of the phase boundary as a function of time is then simply determined by

$$\frac{1}{r} = \frac{1}{R_{eq}} + \frac{1}{\sqrt{\pi\beta t}} \tag{6.4}$$

We compared the model above to our experimental data acquired at the highest excitation powers of the expansion of the bubble radius $r(t)$ over the first 100 ms of excitation at 488, 514, and 561 nm (Figure 6.11) by fitting the data to Equation 6.4. These fits led to an estimate of $\dot{Q_{in}}$, R_{eq}, and β using Equation 6.2, and we compared these to experimental values for validation. An estimate of β using relevant parameters [174, 181] is 1.3×10^5 (m^2/s) while the fits return β in the range $0.5 - 0.9 \times 10^5$ (m^2/s). The fitted values of R_{eq} are 3.5 μm (488 nm), 4 μm (514 nm) and 3.4 μm (561 nm), which compare very well to our experimental R_{eq} values at 2 mW of incident power (Figure 6.10 (b)). From the Equation 6.3 above, our calculated $\dot{Q_{in}}$ in values are in the range $5 - 6 \times 10^7$ W.

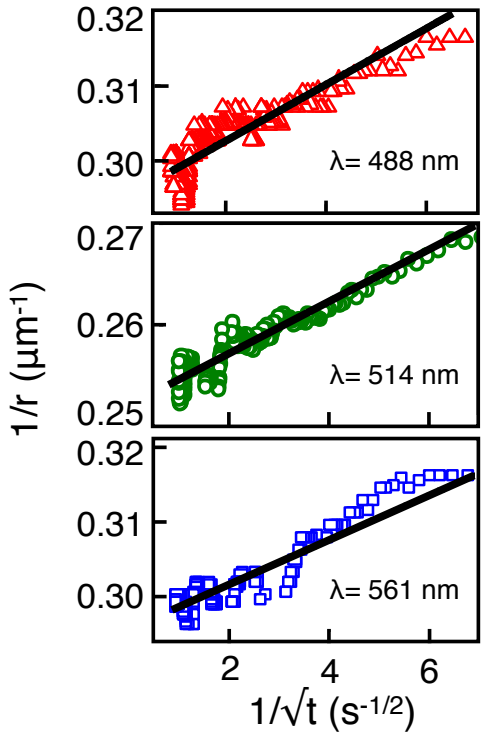

Figure 6.11: Spectral dependence of photothermal bubble formation. The bubble radius $r(t)$ increases over the first 100 ms of excitation at 488 nm (red), 514 nm (green), and 561 (blue). (Reprinted from reference [4] with permission from Macmillan Publishers Ltd. ©2017.)

As an alternate and independent measurement of the heat generated at the NAM surface, we computed the scattered electric field in the near-field regime of AuNPs in a shell wall, and examined the spatial temperature distribution. The shell was simulated by a random distribution of AuNPs in a spherical arrangement with an average distance of 12 nm

(Figure 6.5), with shell thickness $\sim$ 160 nm. Using FDTD and discrete dipole scattering (nanoDDSCAT) software [182], we found that the electric field was consistent with the superposition of fields from the AuNPs, indicating that the AuNPs do not exhibit any inter-particle coupling. We then used the simulated electric field, in combination with measurements that showed typical absorption by a NAM to be $\sim$ 2-5 $\%$ of the incident power and a depth of field of $\sim$ 400 nm, to calculate the heat from a single NAM to be $\dot{Q}_{in} = 9 \times 10^7$ W, in complete agreement with the calculated Q_{in} derived from bubble expansion data.

6.3.5 Accurate thermal mapping

Using Equation 6.2, we then computed the spatial dependence of $\triangle T \equiv T(r) - T(\infty)$ summed over all AuNPs in a shell for six excitation wavelengths (Figure 6.12). Since heat generation is directly related to the mobility of electrons in the AuNPs, $\triangle T$ is predictably maximized at excitations tuned to the plasmon resonance frequency. These maps indicate strong localization of photothermal heating, with $\triangle T$ dropping to half its maximum value within 20-25 $\%$ of the shell diameter (Figure 6.13 (b)). We determined that the maximum temperature change arising from the photothermal effect is $\triangle T_{max} = 50\ ^0$C at the shell surface for excitation at 514 nm near the LSPR, at the highest excitation powers used.

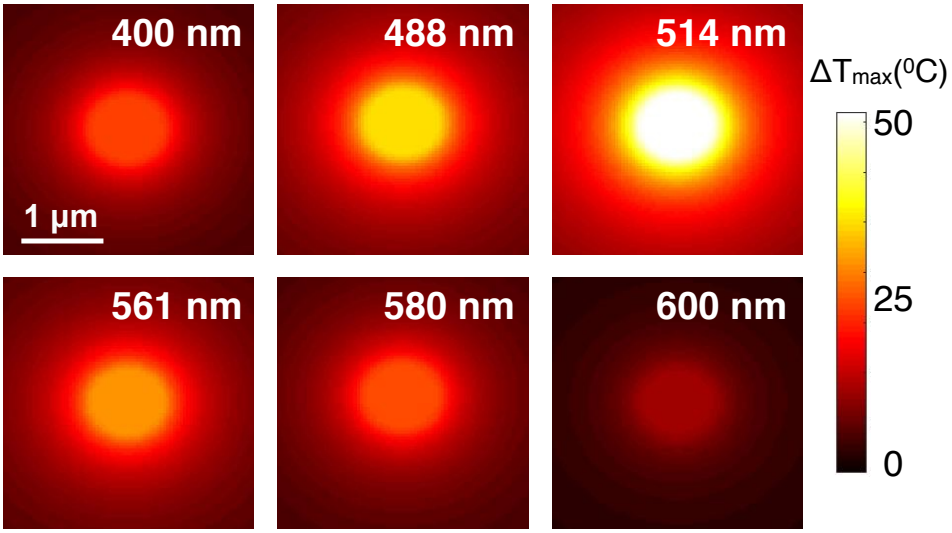

Figure 6.12: Simulated thermal maps over a range of excitation wavelengths showing that photothermal temperature changes, $\triangle$T, remain strongly localized to the surface of the NAM. (Reprinted from reference [4] with permission from Macmillan Publishers Ltd. ©2017.)

Since the samples were maintained at 25 ^{0}C, the actual temperature is 75 ^{0}C, very close to the crystal-to-nematic transition temperature of the mesogenic ligands (Figure 6.8). $\triangle T_{max}$ at different wavelengths showed high levels of agreement with the shell extinction spectrum (Figure 6.13 (a)). For biological applications, the heat shock response should enable most bacterial species to survive at higher temperatures during the short time interval required for shell disintegration [183].

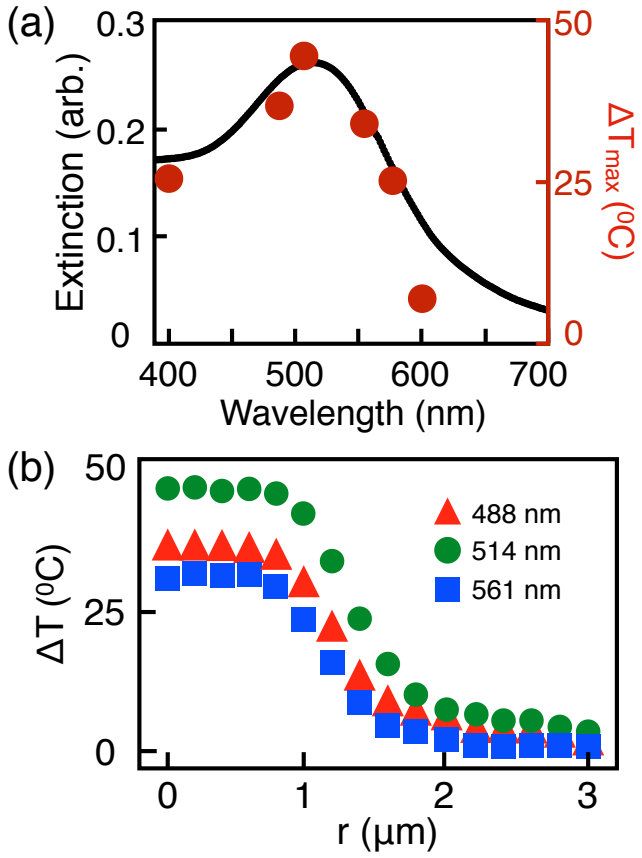

Figure 6.13: (a) The extinction spectrum of a NAM with resonance at 520 nm (curve) shows good agreement with the maximum temperature change at the shell surface (filled red circles). (b) Temperature change varying with distance r from shell center. (Reprinted from reference [4] with permission from Macmillan Publishers Ltd. ©2017.)

6.4 Conclusion

The success of a drug delivery platform depends on a variety of properties. Our nano-assembled shells provide dramatic improvements on several fronts relative to currently available systems. After encapsulation, there was no significant leakage for over five months, allowing for long-term storage. The optical intensity required for shell disintegration was much lower than that used by other methods, which we attribute to the optimal packing of AuNPs in the shell walls. Furthermore, the time required to release the contents was on the order of seconds, as fast as or faster than other methods. Two aspects of the capsules that would need to be further optimized in the future for in vivo applications are size reduction [184], and actuation by near-infrared (NIR) excitation [185] With respect to the first, the NAM size distribution is strongly influenced by the rate of cooling the LC host, with faster rates producing smaller shells. We have achieved shell structures with diameters of a few hundred nanometers, and further optimization of this process may lead to further decreases in shell size. The plasmon actuation demonstrated here is not limited by the shell diameter, although it is size dependent. The temperature at the shell surface scales with the radius, which implies smaller shells will require higher excitation power for the photothermal effect to rupture the structure. This necessity can be mitigated by redesigning the mesogenic ligand. The temperature at which shell structure is disrupted is determined by the liquid crystalline phase transitions of the ligand molecules, and therefore, structural alterations in the mesogenic portion of the ligands will allow us to tune the plasmon actuation of the shells. Because the ligand is easily tailored (see added synthetic scheme, Figure 6.16), we could increase ratio of aliphatic (sp3) to aromatic C–C bonds to minimize ordering of the ligands in the shells, which could be expected to lower the temperature at which they rupture. Another approach is to shorten the flexible portion of the ligands to allow for higher density of AuNPs, which would also compensate for the excitation power changes. The second, tuning the LSPR to longer wavelengths, is a more complex task [185, 186], and the most well suited Au nanostructures would be hollow nanoparticles where the resonance is shifted by altering shell diameter and thickness [187]. This functionality would add considerable versatility to utilizing these shells in vivo, since NIR radiation is capable of deeper tissue penetration compared to visible wavelengths.

The versatility of the shell construction process, in addition to the fact that it is a solution-based one-step synthesis with high yield, allow incorporating these variations relatively straightforward. Coupled with the accuracy of our calculations that allow us to map the temperature changes with high precision, our self-assembled plasmon actuated capsules provide a transformative platform for cargo delivery systems.

6.5 Supplemental information

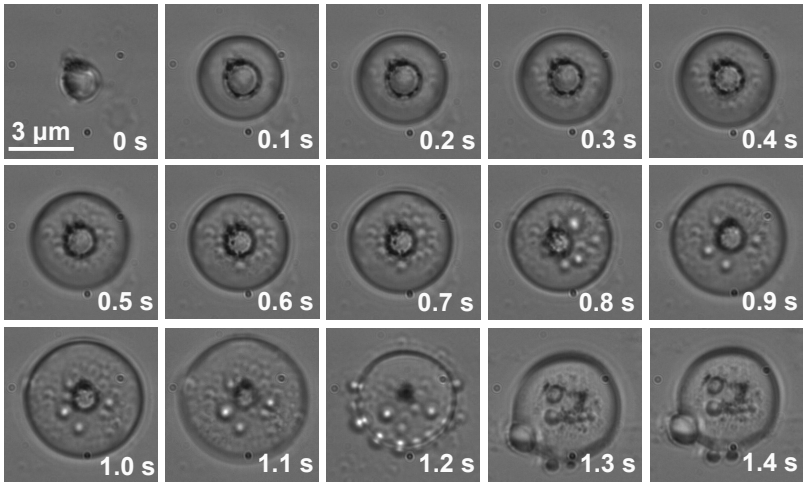

Figure 6.14: Bright field images of plasmon-actuated optically induced shell disintegration leading to encapsulated dye being released over 1.4 s of illumination at 2 mW of incident power. Excitation wavelength is 514 nm.

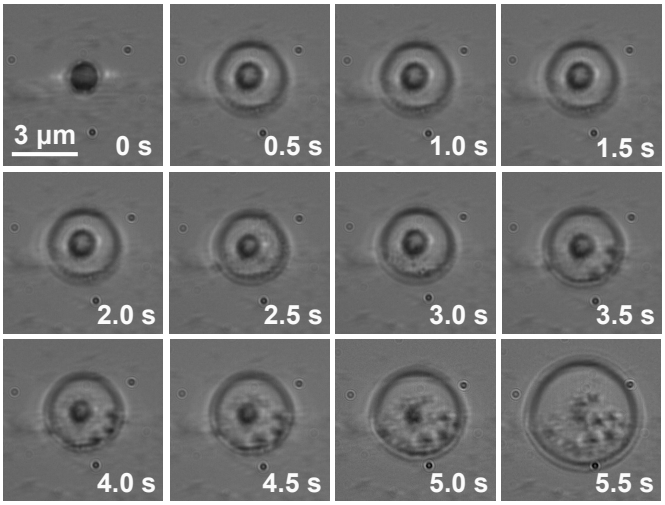

Figure 6.15: Bright field images of plasmon-actuated optically induced shell disintegration leading to encapsulated dye being released over 5.5 s of illumination at 2 mW of incident power. Excitation wavelength is 561 nm.

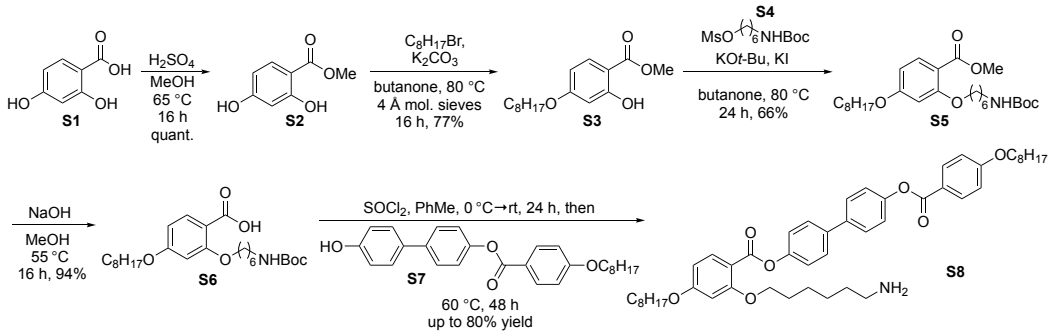

Figure 6.16: Synthesis of the mesogenic ligand. The rod-like arm S7 and the amine linker S4 are made from commercial starting materials in one step (see Figure 6.16 for details). The synthesis starts with Fischer esterification of S1 to give S2 in quantitative yield (S2 is also commercially available). S3 is prepared by selective Williamson Etherification of S2. The amine linker S4 was then attached to S3 to afford S5. Base-mediated hydrolysis of ester S5 gave carboxylic acid S6 in excellent yield. Finally, this compound was coupled to the rod-like arm S7, and the product S8 was isolated by silica gel chromatography. Yields in the final step proved unpredictable: the ester and amine functional groups tend to react, leading to decomposition.

Methyl 2-hydroxy-4-(octyloxy)benzoate (S3).^{1}H NMR (400 MHz, $CDCl_3$): δ 10.95 (s, 1H), 7.72 (d, J = 9.6 Hz, 1H), 6.43 (s, 1H), 6.43–6.40 (m, 1H), 3.96 (t, J = 6.7 Hz, 2H), 3.91 (s, 3H), 1.78 (p, J = 8.2 Hz, 2H), 1.47-1.39 (m, 2H), 1.35-1.24 (m, 8H), 0.88 (t, J = 7.0 Hz, 3H); ^{13}C NMR (100 MHz, $CDCl_3$): δ 170.4 (CO), 165.2 (C), 163.7 (C), 131.1 (CH), 107.9 (CH), 105.2 (C), 101.1 (CH), 68.3 (CH_2), 51.9 (CH_3), 31.8 (CH_2), 29.3 (CH_2), 29.2 (CH_2), 29.0 (CH_2), 25.9 (CH_2), 22.6 (CH_2), 14.1 (CH_3). ATR-FTIR (thin film): 3207, 2923, 2850, 1674, 1618, 1577, 1444, 1332, 1247, 1181 cm^{-1}.

6-((tert-butoxycarbonyl)amino)hexyl methanesulfonate (S4). ^{1}H NMR (400 MHz, $CDCl_3$): δ 4.51 (s, 1H), 4.22 (t, J = 6.5 Hz, 2H), 3.11 (q, J = 6.8 Hz, 2H), 3.00 (s, 3H), 1.75 (p, J = 6.5 Hz, 2H), 1.55-1.45 (m, 3H), 1.44 (s, 9H), 1.42-1.31 (m, 3H); ^{13}C NMR (100 MHz, $CDCl_3$): δ 156.0 (C), 79.1 (C), 69.9 (CH_2), 40.4 (CH_2), 37.4 (CH_3), 29.9 (CH_2), 29.0 (CH_2), 28.4 ($3CH_3$), 26.2 (CH_2), 25.1 (CH_2).

Methyl 2-((6-((tert-butoxycarbonyl)amino)hexyl)oxy)-4-(octyloxy) benzoate (S5). The spectral data matched those reported by Hirst and coworkers. ^{1}H NMR (400 MHz, $CDCl_3$): δ 7.82 (d, J = 8.6 Hz, 1H), 6.68-6.43 (m, 2H), 4.57 (br s, 1H), 3.98 (q, J = 6.4 Hz, 4H), 3.84 (s, 3H), 3.16-3.06 (m, 2H), 1.89-1.72 (m, 4H), 1.53-1.45 (m, 5H), 1.43 (s, 9H), 1.37-1.22 (m, 11H), 0.88 (t, J = 7.0, 3H); ^{13}C NMR (100 MHz, $CDCl_3$): δ 166.3 (C), 163.7 (C), 160.8 (C), 156.0 (C), 133.8 (CH), 112.2 (C), 105.1 (CH), 100.3 (CH), 77.2 (C), 68.7 (CH_2), 68.2 (CH_2), 51.6 (CH_3), 40.5 (CH_2), 31.8 (CH_2), 29.3 (CH_2), 29.2 (CH_2), 29.1 (CH_2), 29.0

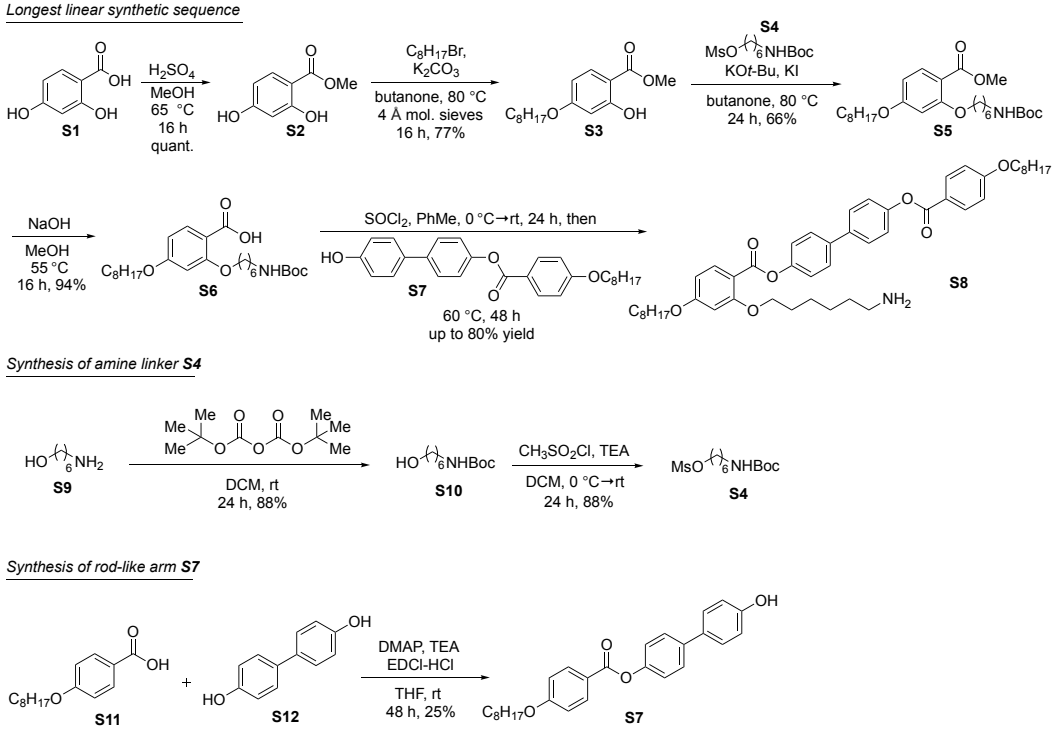

Figure 6.17: All steps involved in the synthesis of the mesogenic ligand. S2, S9, S10, S11, and S12 are commercially available from chemical suppliers.

(CH_2), 28.8 (CH_2), 28.4 ($3CH_3$), 26.4 (CH_2), 26.0 (CH_2), 25.7 (CH_2), 22.6 (CH_2), 14.1 (CH_3). ATR-FTIR (neat): 3375, 2927, 2856, 1704, 1608, 1506, 1250, 1175 cm^{-1}.

2-((6-((tert-butoxycarbonyl)amino)hexyl)oxy)-4-(octyloxy)benzoic acid (S6). ^{1}HNMR (400 MHz, $CDCl_3$): δ 10.72 (br s, 1H), 8.10 (d, J = 8.7 Hz, 1H), 6.61 (dd, J = 8.8, 2.3 Hz, 1H), 6.48 (d, J = 2.3 Hz, 1H), 4.53 (br s, 1H), 4.19 (t, J = 6.7 Hz, 2H), 4.00 (t, J = 6.7 Hz, 2H), 3.16–3.07 (m, 2H), 1.91 (p, J = 7.8 Hz, 2H), 1.79 (p, J = 8.2 Hz, 2H), 1.56-1.45 (m, 5H), 1.43 (s, 9H), 1.42-1.24 (m, 11H), 0.88 (t, J = 6.6, 3H); ^{13}C NMR (100 MHz, $CDCl_3$): δ 165.3 (C), 164.6 (C), 158.9 (C), 156.0 (C), 135.4 (CH), 110.2 (C), 107.1 (CH), 99.8 (CH), 79.1 (C), 70.0 (CH_2), 68.6 (CH_2), 40.3 (CH_2), 31.8 (CH_2), 29.9 (CH_2), 29.3 (CH_2), 29.2 (CH_2), 29.0 (CH_2), 28.8 (CH_2), 28.4 ($3CH_3$), 26.3 (CH_2), 25.9 (CH_2), 25.6 (CH_2), 22.6 (CH_2), 14.1 (CH_3). ATR-FTIR (neat): 3303, 2927, 1608, 1533, 1439, 1267, 1197, 1126 cm^{-1}. HRMS (ESI) m/z calculated for $C_{26}H_{43}NO_6$ $[M]^+$: 466.3163, found: 466.3117.

4'-Hydroxy-[1,1'-biphenyl]-4-yl 4-(octyloxy)benzoate (S7). ^{1}H NMR (400 MHz, $CDCl_3$): δ 8.16 (d, J = 8.8 Hz, 2H), 7.56 (d, J = 8.7 Hz, 2H), 7.45 (d, J = 8.7 Hz, 2H), 7.24 (d, J = 8.7 Hz, 2H), 6.98 (d, J = 8.7 Hz, 2H), 6.89 (d, J = 8.7 Hz, 2H), 4.05 (t, J = 6.8 Hz, 2H), 1.83 (p, J = 6.8 Hz, 2H), 1.48 (p, J = 6.8 Hz, 2H), 1.38-1.26 (m, 8H), 0.89 (t, J = 6.7

Hz, 3H): ^{13}C NMR (100 MHz, $CDCl_3$): δ 165.1 (C), 163.5 (C), 155.1 (C), 150.0 (C), 138.4 (C), 133.2 (C), 132.3 (2CH), 128.4 (2CH), 127.7 (2CH), 122.0 (2CH), 121.5 (C), 115.6 (2CH), 114.3 (2CH), 68.3 (CH_2), 31.8 (CH_2), 29.3 (CH_2), 29.2 (CH_2), 29.1 (CH_2), 26.0 (CH_2), 22.6 (CH_2), 14.1 (CH_3). ATR-FTIR (neat): 3458, 2920, 2853, 1748, 1606, 1497, 1254, 1166 cm^{-1}.

4'-((4-(Octyloxy)benzoyl)oxy) -[1,1'-biphenyl]-4-yl 2-((6-aminohexyl)oxy) -4-(octyloxy)benzoate (S8). ^{1}H NMR (400 MHz, $CDCl_3$): δ 8.16 (d, J = 8.8 Hz, 2H), 8.05 (d, J = 9.1 Hz, 1H), 7.61 (d, J = 8.6 Hz, 2H), 7.60 (d, J = 8.4 Hz, 2H), 7.27 (d, J = 8.6 Hz, 2H), 7.26 (d, J = 8.4 Hz, 2H), 6.98 (d, J = 8.7 Hz, 2H), 6.53 (dd, J = 9.0, 6.5 Hz, 1H), 6.49 (d, J = 2.5 Hz, 1H), 4.05 (t, J = 6.5 Hz, 2H), 4.02 (t, J = 6.5 Hz, 2H), 4.01 (t, J = 6.5 Hz, 2H), 2.81 (br s, 2H), 2.67 (t, J = 6.4 Hz, 2H), 1.91–1.77 (m, 6H), 1.57-1.43 (m, 9H), 1.41-1.26 (m, 17H), 0.91 (t, J = 6.5 Hz, 3H), 0.90 (t, J = 6.5 Hz, 3H); ^{13}C NMR (125 MHz, $CDCl_3$): δ 167.9 (C), 167.3 (C), 166.8 (C), 166.3 (C), 164.5 (C), 153.2 (C), 153.1 (C), 140.7 (C), 140.3 (C), 137.1 (CH), 135.0 (2CH), 130.9 (4CH), 125.0 (2CH), 124.8 (2CH), 124.0 (C), 117.0 (2CH), 113.3 (C), 108.2 (CH), 102.8 (CH), 71.4 (CH_2), 71.0 ($2CH_2$), 42.6 (CH_2), 34.5 (CH_2), 32.0 ($2CH_2$), 31.9 ($2CH_2$), 31.8 (CH_2), 31.7 (CH_2), 31.3 (CH_2), 29.7 (CH_2), 28.7 ($2CH_2$), 28.6 (CH_2), 28.0 (CH_2), 26.8 (CH_2), 25.3 ($2CH_2$), 16.8 ($2CH_3$). ATR-FTIR (neat): 2923, 2854, 1726, 1605, 1251, 1196, 1162 cm^{-1}. HRMS (ESI) m/z calculated for $C_{48}H_{63}NO_7$ $[M]^+$: 766.4677, found: 766.4659.

6.6 Acknowledgments

This research was supported by funds from UCMEXUS-CONACYT, National Science Foundation grants CAREER DMR-105680 to Prof. Ghosh, CBET-1507551 to Prof. Ghosh and Prof. Hirst, CAREER MCB-1149328 to Prof. Huang, EF-1038697 to Prof. Huang and Prof. Gopinathan, DMS-1616926 to Prof. Gopinathan, a James S. McDonnell Foundation Award to Prof. Gopinathan, and in part by the NSF nanoBIO node (ECC-1227034) and the NSF-CREST: Center for Cellular and Bio-molecular Machines (CCBM) at UC Merced (HRD-1547848). Portions of this research were carried out at the Stanford Synchrotron Radiation Lightsource, a Directorate of SLAC National Accelerator Laboratory and an Office of Science User Facility operated for the U.S. Department of Energy Office of Science by Stanford University.

Chapter 7

Nano-assembled gold microcapsules in nanobiotechnology applications

In the following chapter, I introduce the potential directions for the future development of our research. I describe the potential to direct further the nano-assembled gold microshells (AuNAMs) into a new type of engineering platform that harnesses microscale control-release biocapsule delivery technologies. The primary application of our biocapsule unique design is to engineer a new type of delivery system. These capsules can also be utilized to deliver growth factors for cells, stem cells, or prokaryotes as well could promote further chemical reagent transport and development. We are planing to exploit our AuNAMs photo-thermally activation to introduce with precision this biocapsule in the development of delivery technologies based on biologically inspired methods such as targeted drug delivery, controlled-release delivery, live-cell/microbiota delivery, and growth-factor delivery systems.

7.1 Introduction

Targeted "cargo" delivery systems with controlled release mechanisms have been the subject of extensive research. Early efforts were centered on polymer-based capsules sensitive to thermal gradients and pH [188, 189], and the latter remains the present-day release basis of orally ingested medicinal products. With advances in nanotechnology, incorporating nanomaterials of varied compositions and morphologies in polymer or gel-based matrices has led to the development of structures that offer additional advantages [163–170]. One such advantage is the ability to remotely control the release process using stimuli such as electric and magnetic fields, as well as optical excitation. Another advantage is multifunctionality, wherein the nanocomposites combine drug delivery operations with therapeutic capabilities, such as hyperthermia for destruction of cancerous tissues and cells. Opti-

cal actuation of "cargo" delivery capsules allows rapid release at specific locations, and typically uses the photothermal effect to drive the structural changes needed to unload contents. The power, wavelength, and duration of incident light required is strongly dependent on the components used for construction of the capsules. The most popular approach involves temperature-sensitive gels and polymers with embedded semiconducting, metallic, or metal-oxide nanostructures [164–166]. Light absorbed by the structures heats the crystal lattice, which transfers the heat to the host medium and causes conformational changes that disrupt the structure of the capsule. Appropriately sized metallic nanoparticles are particularly efficient absorbers of incident radiation since they support plasmon resonances. Gold nanoparticles (AuNPs) are ideal candidates, with the localized surface plasmon resonance (LSPR) lying in the visible and near infra-red regions of the electromagnetic spectrum [26]. The efficacy of stimulated drug delivery systems depends strongly on robust leakage-free containment.

Recently, we developed our successful application, a microscale cargo delivery system. Our application is constructed from gold nanoparticles (AuNPs) that are processed to form a microshell cavity. These gold microshells can encapsulate organic material, and the material does not interact with external substances outside of the shells. Captured material can later be controllably released with a low-power resonant light. An application of our microshells unique design could be to engineer a new type of "cargo" delivery system, or biocapsules system, that is photo-thermally controlled. This will help localize and control the release of not only medicines and therapies but also living cells into specific tissues in a host. Our most recent experimental results have shown that microorganism, Escherichia coli, can remain inside of our microshells for several hours without noticeable viability damage. This platform can greatly enhance the process of controlling cell differentiation and growth rates by encapsulation of stem cells or microorganism in our microshells and can be utilized to controllably activate cell-cell interactions by releasing captured live cells into new biological environment.

7.2 Experimental methods

7.2.1 Encapsulation of fluorescent microbeads

This project used 0.2 μm fluorescent microbeads (Thermo Fisher Scientific), carboxylate coupling to the surface of the micro-spheres, with emission of 515 nm, were used. The fluorescent micro-spheres were diluted in deionized water (1:1000), then added to a LC-AuNP mixture to obtain a composite with a dilution of 1:5000. Following the sonication and shell formation procedure outlined in the Chapter 5, encapsulated fluorescent micro-spheres AuNAMs were formed (Figure 7.1). The resulting micro-capsules were spun down with a centrifuge (5000 rpm for 10 min), the supernatant discarded, and the AuNAMs were

re-suspended in fluorescent-free LC (5CB). Repeat this process for several times, then the sample was imaged using epifluorescence microscopy (Nikon) after each centrifugation step to ensure that the shells remained undamaged.

7.2.2 Bacteria cultures

Green fluorescent protein (GFP) labeled or non-GPF-labeled Escherichia coli (E. coli) on Lysogeny broth (LB) agar plates were incubated overnight at 37 ^{0}C, then incubated with LB media culture at 37 ^{0}C for 24 hours in a shaking incubator. After the cultures were grown, they were subcultured (1:500) into fresh LB media, and 0.5 mL of stational or exponential-phase cultures were pelleted by centrifugation (5,000$\times$g) for 2 min at room temperature. Finally, these pellets were re-suspended in 2 mL fresh LB media.

7.2.3 Viability of Escherichia coli in liquid crystal medium

After preparing E. coli culture, the culture was diluted (1:500) into fresh LB. Adding different amount of LC in LB media, we prepared 11 different LC concentration samples. These sample solution was added into 0.2 μL LB-E. coli media and mixed them until forming homogeneous mixture solution. Concentrations of these 11 LC-LB-E.coil mixture were from 0 to 95 vol$\%$ LC. Each mixture solution was pipetted in 96-well plates and measured their optical density (OD) by using SpectraMax Plus spectrophotometer (Molecular Devices).

7.2.4 Encapsulation of Escherichia coli

After culturing E. coli and re-suspending the pellets into LB media, the E. coli pellets-LB solution (85 μL) was then added to a 5 hours sonicated LC-AuNP mixture (15 μL), and the resulting mixture was sonicated for 20 more minutes at 40 ^{0}C. Following the procedure of shell formation introduced in the Chapter 5, we captured E. coli inside of our AuNAMs. The AuNAMs with E. coli were spun down with a centrifuge (6000 rpm for 30 min), the supernatant (un-captured E. coli) was discarded. We re-suspend the AuNAMs in 100 $\%$ LB media. The process was repeated at least two times until removing all remaining LC solution in the media.

7.2.5 C2C12 cell culture

C2C12 myoblasts were seeded into 12 well rectangular plates at a density of 4×10^4 cells per well, with 1 mL of growth medium comprising Dulbecco's Modified Eagle's Med- ium (DMEM); 25 mM glucose (Invitrogen), supplemented with 10$\%$ fetal bovine serum and 1$\%$ penicillin-streptomycin. This was maintained in an incubator at 37 ^{0}C under a 5$\%$ CO_2 atmosphere. Growth media was replaced every every 24 hours.

7.2.6 Live-dead assay

The cultured C2C12 cells were incubated in phosphate buffered saline (PBS), supplemented with 1 nM calcein-AM and 6 nM ethidium homodimer, at 37 ^{0}C and 5$\%$ CO_2 for 30 minutes. Each stained cell suspension sample was transferred to a well in a 24 wells-plate and 8 random spots per well were imaged (Nikon epifluorescent microscopy). Live (green) and dead (red) cells were counted daily. For each sample, population of live cells was recorded. All measurements were subsequently corrected by setting the control environment, such as measured at the same time and the same temperature.

7.2.7 Cell counting

Added 1 mL of 0.05 $\%$ trypsin-0.53 mM EDTA solution (Thermo fisher scientific) to each well plate, and observed cells under an optical microscopy (Nikon) until cell aspect changed to round. Aspirated the majority of the trypsin-EDTA solution and let stand for an additional 1-2 minutes, then pipetted 10 μL of the C2C12 cell suspension to hemocytometer. Used an optical microscopy (Nikon) and counted the number of cells on the hemacytometer. Cell count data was representative of eight independent experiments.

7.2.8 Sterilization of AuNPs and LC

Dry AuNPs were dispersed into ethyl alcohol ($\geq$ 99.5 $\%$, Sigma Aldrich) in glass vials for 3 hours, removed the ethyl alcohol solvent by a rotary evaporator (BUCHI). The AuNPs in the glass vials are then heated in the VWR 1400E vacuum oven at 150 ^{0}C with 20 psi for 5 hours. Similarly, LC solution in the glass vials is heated up in the vacuum oven at 150 ^{0}C with 20 psi for 8 hours.

7.3 Preliminary results

7.3.1 Encapsulated micron-sized 3D objects in AuNAMs

Microencapsulation of bio-related active agents such as enzymes [190], drug [191], microorganism [192–194], and cells [195, 196] has shown potential improvement in medical, pharmaceutical, and bio-engineering fields. In previous study, we reported our AuNAMs can encapsulate organic dye molecules. Now, we plan to develop microencapsulation techniques with improved performance. We observe that these AuNAMs are capable of encapsulating 0.2 μm diameter fluorescent beads (Figure 7.1), monitored emitted light from the several microbeads by using a fluorescence microscope, and this emission proves that our micro-assemblies has high possibility to capture micron-sized 3D objects. Additionally, the AuNAMs with fluorescent microbeads can be made to disintegrate by low power light,

2 mW within several seconds. The results was pretty similar to our previous experimental results. Thus we are confident that our results exhibiting the capture and optically regulated release of encapsulated micron-scale objects. Additionally, it can be exploited to enhance a controlled releasing system of inner materials, as well as providing a method of controlled heating for specific regions within a given embedding micron-sized material.

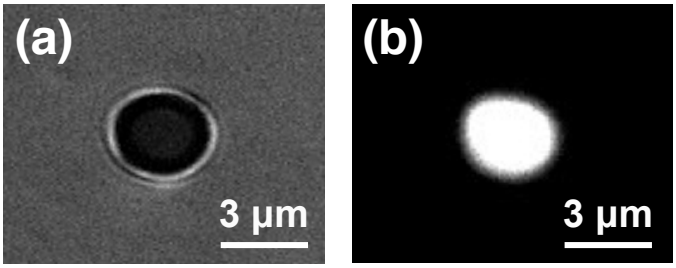

Figure 7.1: The encapsulation of 0.2 μm diameter fluorescence beads in a AuNAM. Images exhibit a optical microscopy (bright field) (a) and fluorescence microscopy image (b).

7.3.2 Biocapsules for microorganism

Robust biocapsule cargo delivery systems pose a significant design challenge. Major challenges associated with biocapsules through variety of microorganism or live cell encapsulation techniques. Forming our AuNAMs, Escherichia coli (E. coli) need to be added to the liquid crystal (LC)-gold nanoparticles (AuNPs) mixture solution, and sonicate the mixture with E. coli for at least 30 minutes. However, the toxicity level of LC and sonication on E. coli cells are still lacked solid supporting evidence. Thus, we need to investigate the effect of the ultrasonic irradiation time on the inactivation capability of E. coli and the viability of E. coli with various LC volume in LB medium before capturing microorganism within the AuNAMs. In microbiology, growth dynamics of bacterial cells is usually examined by optical density (OD) measurements using a spectrophotometer. OD is a light scattered by the bacteria suspension, and it manifests itself as absorbance. Spectra of OD correlates directly with the cell concentration [196], thus the spectra is often interpreted as a cell growth characteristics. We grew E. coli bacteria in LB media overnight at 37 ^{0}C. We also prepared 3.8 μL of 11 different vol$\%$ LC solution in LB media with 0.2 μL of 500:1 diluted LB-E. col solution. The solution was pipetted in a 96-well plate for the spectrophotometer measurement. Investigating E. coli viability, OD was monitored in 11 different wells derived from the same starting amount of E. coli population. Growth curve in Figure 7.2 conforms that viability of E. coli is truly depend on LC concentration since high concentration on LC reduces population of live E. coli, most likely associated with apototic effects or sever cell

growth inhibition. That is, damaged cells have a long lag period, since they must repair themselves before they can engage in reproduction.

Similarly, we tested E. coli viability treated with ultrasound with a fixed frequency of 40 kHz at different time duration. 0.2 μL of diluted LB-E. coli with 3.8 μL LB media was prepared in each Eppendorf tube and placed in the sonication bath. During the experiment, the temperature was controlled by a water bath and was kept constant at 37 $\pm$ 1 ^{0}C. The water bath level inside the sonicator (Branson) was 16 cm, and the tip of Eppendorf tube was positioned in the middle of the water bath. A series of experiments were performed with different ultrasonic duration between 0 and 90 minutes. Each sonicated sample was then pipetted into a 96-well plate and OD was measured by spectrophotometer over 18 hours periods.

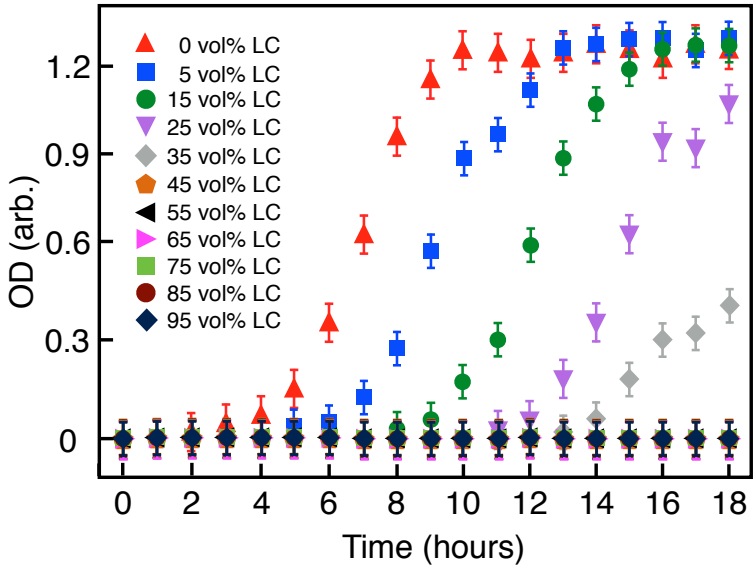

Figure 7.2: Growth curves of E. coli in LB broth in the presence of different concentrations of liquid crystal (LC). Higher concentration of LC in the sample makes longer time to enter the exponential growth phase. 0 vol% LC means E. coli bacteria are in 100 % LB media.

Figure 7.3 illustrates that as the ultrasonic duration increases, the longer time to enter the exponential growth phase due to reducing cell population caused by lysing. This is because the value of OD spectra is linearly proportional to the concentration of bacteria cell in the suspension and each E. coli bacterium has roughly a doubling time of 20 min. Thus, longer response time for entering exponential phase, which means staying low OD intensity for longer duration, represents smaller number of E. coli cells survived in higher LC concentration or longer ultrasonic irradiation time environment. Collectively, these results indicate that we are still able to use LC-LB solution up to 25 vol% LC in LB media

with maximum 60 minutes ultrasonic duration for capturing E. coli in the AuNAMs. Having confirmed that the invention AuNAMs stably encapsulate a substrate for substantial periods of time, the mesogenic ligand functionalized AuNPs ability to encapsulate green fluorescent protein (GFP) labeled E. coli was investigated.

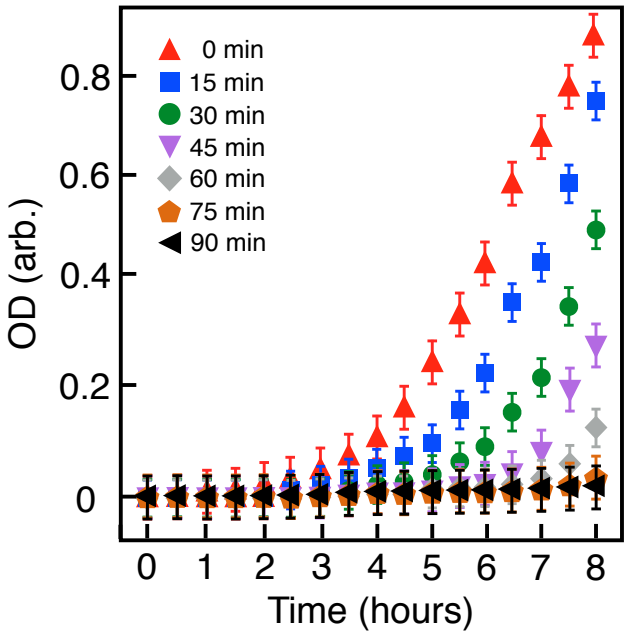

Figure 7.3: Effect of sonication time on E. coli population. Longer duration of ultrasonication causes a long lag period. This represents that the cell population was reduced by sonication and the population size became smaller when the sample was sonicated loner time.

5 nm AuNPs with mesogenic ligands in chloroform solution (1.2 wt%) were dispersed into nematic LC (5CB, Sigma Aldrich) and the LC-AuNPs mixture was then sonicated in a 40 ^{0}C bath for 5 h in an Eppendorf tube, allowing chloroform slowly to be evaporated from the LC solution. Added 15 vol% LC in LB-E. coli media to the LC-AuNPs solution and sonicated for 20 more minutes. As the mixture was cooled into the nematic phase (cooling rate 0.3 ^{0}C/s), E. coli were captured in the AuNAMs. We spun down the AuNAMs with a centrifuge (6000 rpm for 15 min), discarded the supernatant, and re-suspended the fresh LB media. We repeated the process at least two times until removing remained LC solution. We imaged the sample using optical (Figure7.4 (a)) and epifluorescence microscopy (Nikon), which is shown in Figure 7.4 (b). We observed moving AuNAMs for 4 hours under the optical microscopy. Switching the microscopy setting to fluorescence image setting, we monitored GFP emission from E. coli located in the AuNAMs and followed the movement

of the AuNAMs (Figure 7.4 (a,b)). E. coli remains stably encapsulated in the AuNAM and their motion was last at least 6 hours, evidencing to the great capability of microorganism biocapsule. GFP intensity from line cuts along single E. coli bacterium (Figure 7.4 (c)) and encapsulated E. coli (Figure 7.4 (b)) in the AuNAM is shown in Figure 7.4 (d). We approximated GFP fluorescent signals, integrated intensity, from single bacterium cell, and the integrated intensity value was defined as one E. coli population. This method allows for a quantification of bacteria population in the AuNAM. We calculated the integrated intensity from single and multiple E. coli bacteria in NAMs by using both graphs from Figure 7.4 (d). The ratio between these integrated intensity values shows roughly 3 times the single bacteria signal. We thus conclude that each AuNAM is able to capture more than one E. coli bacterium.

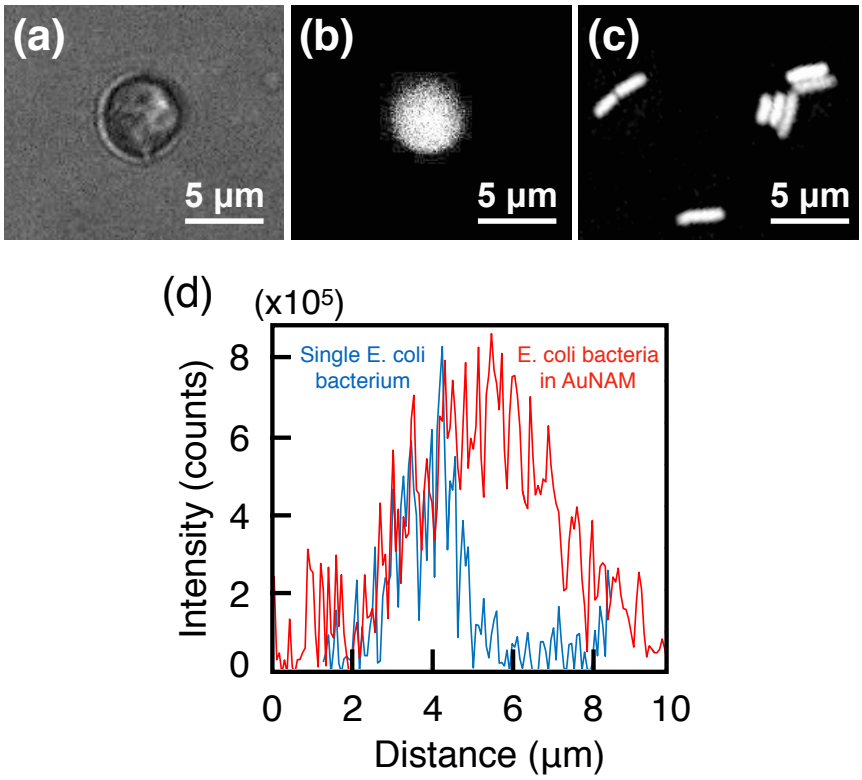

Figure 7.4: The encapsulation of E. coli in AuNAM. Image (a) exhibits a optical microscopy image. (b) A fluorescence image of GFP labeled E. coli bacteria captured (b) and un-captured (c) within AuNAM. (d) Fluorescent signal of E. coli-GFP strain. Line-cuts of the emission signal of single cell bacterium (blue) and bacteria in AuNAMs (red) are represent as their intensity values. Integrated intensity value of single bacterium was defined as one E. coli bacterium.

7.3.3 Biocapsules for stem cells

Escherichia coli bacteria were successfully captured in AuNAMs first time in the laboratory settings. Our most recent experimental results showed that live bacteria can survive inside of the AuNAMs for several hours. To test this with stem cells, we were first required to examine the viability of the stem cells when we introduced major components of our AuNAMs into their biological environment. Cell viability assays were carried out to assess the cytotoxicity of AuNPs and LC (5CB) on C2C12 mouse myoblast cell line. We used the most common viability (live/death) assay kit. The assay kit generally provides a precise time and concentration evaluation of the process of cell death following exposure to a toxic substance. The live/death assay kit, contains chemical compounds calcein-AM and ethidium homodimer (Figure 7.5 (a,b)).

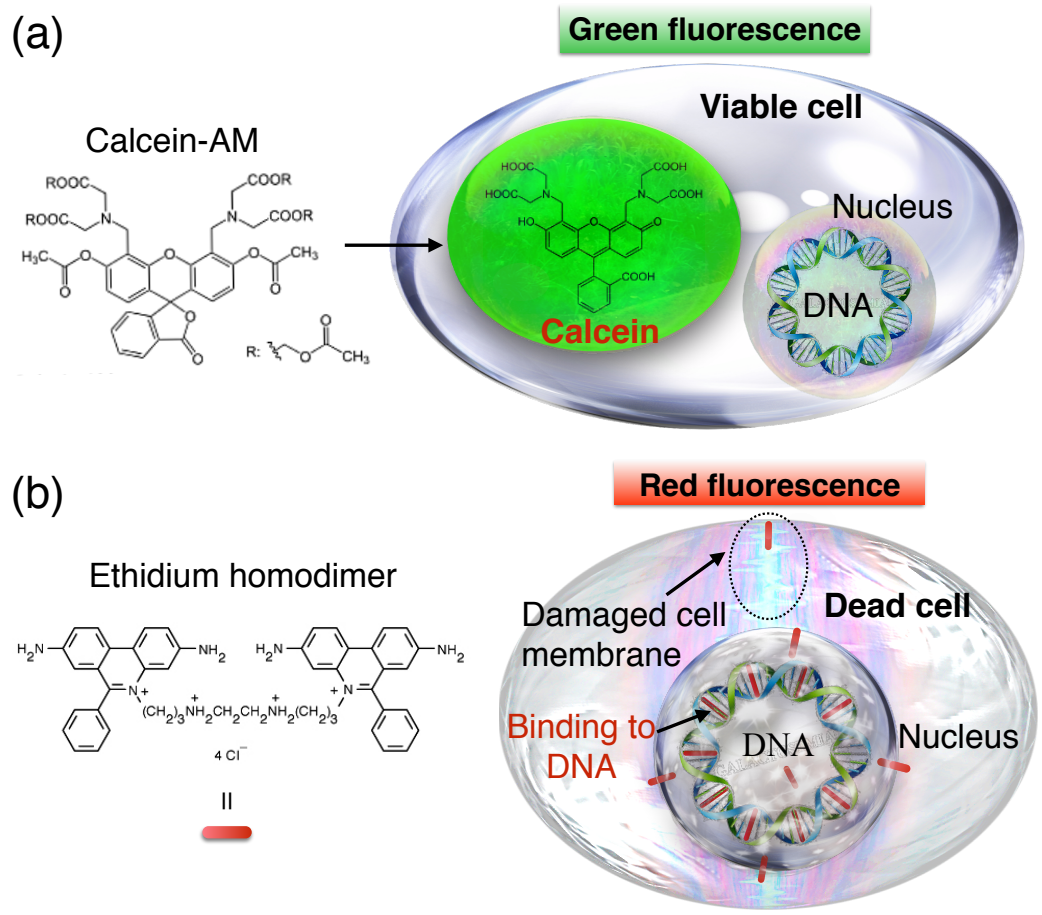

Figure 7.5: Assay system to determine viable cells (a) and dead cells (b).

Calcein-AM is converted from a non-fluorescent compound into a highly fluorescent green fluorophore. It can be transported through the cell membrane into live cells. After calcein-AM enter the cells, intracellular esterases eliminates the acetomethoxy group and produces calcein. (Figure 7.5 (a)). This calcein molecule is trapped inside the cells and emits strong green fluorescence [196]. For dead cells, there is no active esterases process [196], thus we only observe green fluorescence from live cells. On the other hand, ethidium homodimer is a membrane-impermeable fluorescent red fluorophore, which binds to DNA [197]. When cells die, the cell membrane of those cells is damaged. Thus, ethidium homodimer is able to enter those cells and bind to their DNA (Figure 7.5 (b)). Since live cells don't have a disrupted membrane, the ethidium homodimer cannot enter inside of the cells [197]. Based on above information, this method allowed us to examine which cells were alive and died simultaneously when C2C12 cells were exposed to the toxic or non-toxic substance.

The cytotoxicity of AuNPs and LC was assessed on C2C12 myoblast cells by using a live/dead assay kit (Thermo fisher scientific). C2C12 cells (4×10^4) grown in 12-well plates were treated with varying size of AuNPs, concentrations of AuNPs or amount LC in the cell media for 24, 48, 72 hours at 37 ^{0}C and 5 $\%$ CO_2 environment. Cell morphology and viability test were examined daily with a optical and fluorescence microscopy. Each sample, varying incubation periods, was collected and re-incubated in phosphate buffered saline (PBS) supplemented with 1 nM calcein-AM and 6 nM ethidium homodimer at 37 ^{0}C and 5$\%$ CO_2 for 30 minutes. Each stained cell suspension sample was washed with C2C12 media. Eight random spots per well were then imaged by acquiring two-channel settings (Nikon fluorescent microscopy), where green (515 nm) and red (635 nm) fluorescent cells indicated live and dead cells, respectively (Figure 7.5 (a,b)). After the imaging, the myotubes of stained cells were specifically detached from the surface of the well plates by mild trypsinization and it made cell aspect changed to round shape.

Based on the color differences, live cells (green) were counted on a hemocytometer.

The results of cell viability were plotted as live cell population. Figure 7.6 (d) and Figure 7.7 (d) showed that high concentration and large size of AuNPs induced the lowest live cell population. This indicated that these conditions might create minor stressful environment to the C2C12 cells, thus we observed lowering the reproductive rate than the others (Figure 7.6 (e) and Figure 7.7 (e)). Although growth inhibition was noticed at higher concentration and larger size of AuNPs, as confirmed by cell counts, our experimental results demonstrated that all test samples increase their total cell population on daily basis. (Figure 7.6 (a-e) and Figure 7.7 (a-e)). Hence, C2C12 cells in high density of gold in media eventually could complete mitosis and segregate their daughter cells normally.

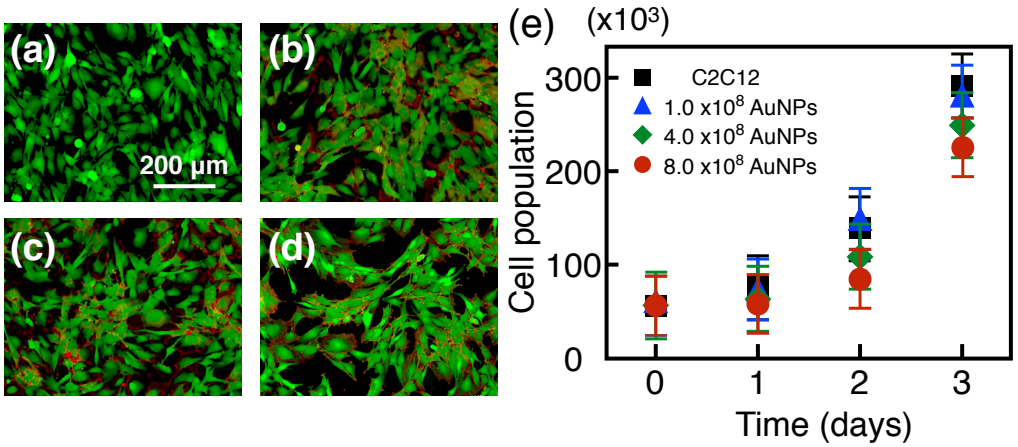

Figure 7.6: Live/dead images of cells incubated with (a) no AuNPs (b) 1×10^8 AuNPs/well, (c) 4×10^8 AuNPs/well, and (d) 8×10^8 AuNPs/well. All AuNPs are 60 nm-diameter size. (e) Live cell population curve for different number of AuNPs in well.

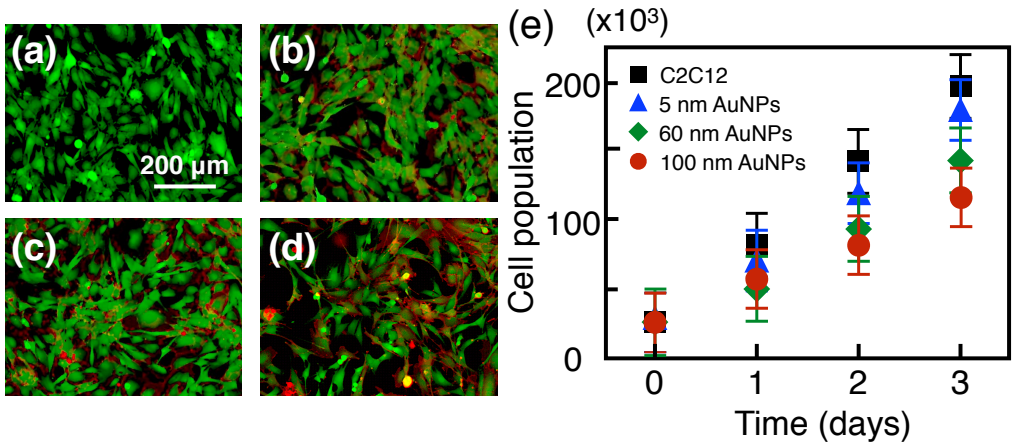

Figure 7.7: Live/dead images of cells incubated with (a) no AuNPs, (b) 5 nm diameter AuNPs, (c) 60 nm diameter AuNPs, (d) 100 nm diameter AuNPs at a density 4×10^8 AuNPs/well. (e) Live cell population curve for different size of AuNPs in well.

On the contrary, the cell viability was dramatically reduced in a dose-dependent manner in the cytotoxicity of LC (Figure 7.8). Especially, we observed at higher concentrations of LC samples. More than 0.1 vol% of LC in media caused cell death and cell growth inhibition result in large red fluorescence emission area, as shown in Figure 7.8 (c,d). Chemical

structure of LC, 5CB, contains cyano (-C≡N$^-$) group and the group might cause cell death or strongly critical cell growth inhibitions. In fact, several studies show that chemical compounds with cyano group trigger cell death or inhibit cell growth, even damage to cancerous cells [198, 199]. Even though existence of LC created severe negative impacts to cell survivability, the low LC concentration , such as 0.05 vol% LC, could sustain more than their initial cell population (Figure 7.8 (b)). This experimental result probed that we might introduce LC solution up to 0.05 vol% in the cell media without causing severe cell growth inhibition or inducing negative cell growth rate (Figure 7.8 (e)). However, additional investigations are necessary to fully define this effect.

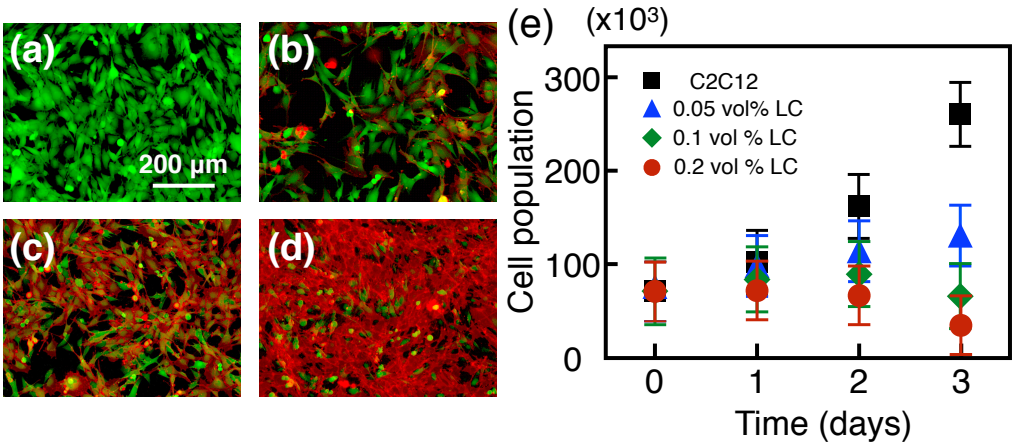

Figure 7.8: Live/dead images of cells incubated with (a) no LC (b) 0.05 vol% LC, (c) 0.1 vol% LC, and (d) 0.2 vol% LC per well. (d) Live cell population curve for different vol % LC per well.

7.4 Future directions

Our self-assembled encapsulation system and methods to control the release of encapsulated material without damaging biological systems are needed to be modified simultaneously. Our Future work will comprise three stages.

7.4.1 Material functionalization of the NAMs

To use our AuNAMs for biological applications, we need to extract and disperse the shells in an aqueous solution. AuNAMs need to retain encapsulated cells without causing any

thermal damage when we release them via light excitation and introduce the captured cells and other components into a new environment. Our current mesogen-functionalized ligands (Figure 6.2) that create the formation of the shells are hydrophobic and require a high local thermal gradient, $\triangle T \approx 50\ ^0C$, when we apply 2 mW of optical power to disintegrate them (Figure 6.9). We need to design new organic ligands, which have low melting points, but still allow them to form AuNAMs at room temperature. Additionally, the AuNAMs with new ligands disintegrate their structure around $40\ ^0C$ using low optical excitation. The hydrophobicity of our current ligands presents a significant challenge for dispersing and resuspending our biomicrocapsules. Adding polar or charge substituents such as phosphate substrates to ligand structure will give us solubility benefits for our system. Thus, modifying hydrophilic ligands with low melting temperature are essential for our application.

7.4.2 Encapsulate living organisms

The condition of encapsulated living cells is affected by a selection of appropriate preparation methods. After the material modification of the ligands, we need to investigate how our new organic ligands affect the survivability of C2C12 cells. Our most recent experimental results have shown that live bacteria can survive inside of the NAMs for several hours (Figure 7.4 (a,b)). To test this with living cells, we will use a live/dead assay kit like we did before and investigate the population of live and dead cells based on their different fluorescent colors. Our AuNAMs must sustain growth of cells, which is essential for encapsulation. We need to monitor that our AuNAMs with new ligands do not cause any major issues or deformities of the cells. If small quantities of our new ligands inhibit cell divisions, we will then seek to modify and design new non-toxic ligands.

7.4.3 Break open the NAM shell and check after condition of encapsulated material

It is very important to know how plasmonic heating affects the chemical structure of encapsulated substrates since excited gold micro-shell raises can generate high localized temperatures that eventually causes them to break. If plasmonic heating has the ability to change encapsulated chemical compounds, we will establish a new type of a chemical activation trigger system controlled by heat. We can capture an inactivated chemical compounds inside of the capsules, then utilized heat to create activated the chemicals by changing the chemical structure when the shells are arrived at targets. We will make sure that our activated chemical compounds have desired molecular geometry and structure by using Nuclear Magnetic Resonance (NMR). This inactivated-activated system will open a new door of medical procedure for chemotherapy and pain treatments and eliminate off target effects in the host. On the other hand, if heating does not affect any chemical structures of inner materials, we are successfully able to introduce our AuNAMs as a safe delivering

applications using active cargo. In both cases, we need to investigate further, specifically the magnitude of the excitation light and the amount of heat generated.

7.5 Conclusion

Micro-scale technology is a powerful tool for addressing many challenges in field of engineering. We developed layer-by-layer three-dimensional nano-assembled gold microcapsules (AuNAMs). Appreciably, we are currently optimizing to use AuNAMs for biological and chemical engineering applications. AuNAMs can capture multicellular prokaryotes, chemicals, and micron-sized abiotic 3D objects such as microspheres. Theoretically, we can use the thermal driven disassembly properties of the AuNAMs as an alternative and simple approach for controlling the release of their cargo at precise locations and desired time. AuNAMs research will open a new door for live cell encapsulation technology, such as controlling cell growth or inhibiting cell differentiation, while a cell is in the AuNAMs.

In addition, Our bio-capsules will have the potential to revolutionize targeted cancer therapy as well as pain management solutions currently in use today in medical facilities around the world. Implementing this goal is important as it fills a need in the current market for controllable drug delivery systems that are non-invasive and can easily be activated at the doctors' office or at home within a few minutes. Moreover, these systems often face difficulties for controlled release in a specific location and desired time, while minimizing damage to healthy tissues.

Our biomicrocapsules have encapsulation efficiency, controlled-release capabilities, and highly localized thermal heating in the area within microns. Therefore, our multifunctional biomicrocapsules can be useful for therapeutic or biotechnological devices such as controlled-release drug delivery, targeted medicine, heat-activated biochemical release, and live cell/microbiota encapsulation/transportation systems. Especially the microbiota encapsulation and transportation application can be implemented as an alternative to fecal bacterial transplants or may also be utilized for laboratory use in studies of bacterial interactions with both antibiotics or bacteria-bacteria interactions. We believe that this system will usher in a new era of novel treatment strategies that are targeted and tailored to the host to both the treatment facility and consumer in the future.

Bibliography

1. Quint, M. T., Delgado, S., Paredes, J. H., Hirst, L. S. & Ghosh, S. Optical switching of nematic liquid crystal film arising from induced electric field of localized surface plasmon resonance. *Proc. SPIE* **9547,** 954729 (2015).
2. Quint, M. T. *et al.* All-optical switching of nematic liquid crystal films driven by localized surface plasmons. *Opt. Express* **23,** 6888–6895 (Mar. 2015).
3. Rodarte, A. L. *et al.* Self-assembled nanoparticle micro-shells templated by liquid crystal sorting. *Soft Matter* **11,** 1701–1707 (2015).
4. Quint, M. T. *et al.* Plasmon-actuated nano-assembled microshells. *Scientific Reports* **7,** 17788 (2017).
5. Maier, S. A. *American National Standard for Safe Use of Lasers: ANSI Z136.1-2000* ISBN: 978-0912035659 (Laser Institute of America, 2007).
6. Sant, S. B. Nanoparticles: From Theory to Applications. *Materials and Manufacturing Processes* **27,** 1462–1463 (2012).
7. Kang, Y. S., Risbud, S., Rabolt, J. F. & Stroeve, P. Synthesis and Characterization of Nanometer-Size Fe3O4 and -Fe2O3 Particles. *Chemistry of Materials* **8,** 2209–2211 (1996).
8. Pankhurst, Q. A., Connolly, J., Jones, S. K. & Dobson, J. Applications of magnetic nanoparticles in biomedicine. *Journal of Physics D: Applied Physics* **36,** R167 (2003).
9. Dobson, J. Gene therapy progress and prospects: magnetic nanoparticle-based gene delivery. *Gene Therapy* **13,** 283–287 (2006).
10. Rudge, S. *et al.* Adsorption and desorption of chemotherapeutic drugs from a magnetically targeted carrier (MTC). *Journal of Controlled Release* **74.** Proceeding of the International Symposium on Tumor Targeted Delivery Systems, 335–40. ISSN: 0168-3659 (2001).
11. Geddes, C. D. & Lakowicz, J. R. *Radiative Decay Engineering. Topics in fluorescence spectroscopy.* 1st ed. ISBN: 978-0-387-22662-0 (Springer, 2005).

12. Brus, L. Electron-electron and electron-hole interactions in small semiconductor crystallites: The size dependence of the lowest excited electronic state. *The Journal of Chemical Physics* **80,** 14403–4409 (1984).

13. Bawendi, M. G., Steigerwald, M. L. & Brus, L. E. The Quantum Mechanics of Larger Semiconductor Clusters ("Quantum Dots"). *Annual Review of Physical Chemistry* **41,** 477–496 (Oct. 1990).

14. Alivisatos, A. P. Perspectives on the Physical Chemistry of Semiconductor Nanocrystals. *The Journal of Physical Chemistry* **100,** 13226–13239 (1996).

15. Ekimov, A. I., Efros, A. L. & Onushchenko, A. A. Quantum size effect in semiconductor microcrystals. *Solid State Communications* **56,** 921–924 (Dec. 1985).

16. Warnock, J. & Awschalom, D. D. Quantum size effects in simple colored glass. *Phys. Rev. B* **32,** 5529–5531 (8 Oct. 1985).

17. Borrelli, N. F., Hall, D. W., Holland, H. J. & Smith, D. W. Quantum confinement effects of semiconducting microcrystallites in glass. *Journal of Applied Physics* **61,** 5399–5409 (June 1987).

18. Talapin, D. V., Lee, J.-S., Kovalenko, M. V. & Shevchenko, E. V. Prospects of Colloidal Nanocrystals for Electronic and Optoelectronic Applications. *Chemical Reviews* **110.** PMID: 19958036, 389–458 (2010).

19. Sukhanova, A. *et al.* Biocompatible fluorescent nanocrystals for immunolabeling of membrane proteins and cells. *Analytical Biochemistry* **324,** 60–67. ISSN: 0003-2697 (2004).

20. Resch-Genger, U., Grabolle, M., Cavaliere-Jaricot, S., Nitschke, R. & Nann, T. Quantum dots versus organic dyes as fluorescent labels. *Nature methods* **5 9,** 763–75 (2008).

21. He, Y. *et al.* Photo and pH Stable, Highly-Luminescent Silicon Nanospheres and Their Bioconjugates for Immunofluorescent Cell Imaging. *Journal of the American Chemical Society* **131.** PMID: 19235931, 4434–4438 (2009).

22. Mason, J. *et al.* Novel fluorescence-based approaches for the study of biogenic amine transporter localization, activity, and regulation. *Journal of Neuroscience Methods* **143.** Studying Monoamine Transporters: Beyond Hypermonoaminaemia, 3–25. ISSN: 0165-0270 (2005).

23. Hayat M. A. (M. Arif), 1.-. *Colloidal gold : principles, methods, and applications* English. Includes bibliographical references and index. ISBN: 0123339286 (v. 2 : alk. paper) (San Diego : Academic Press, 1989).

24. Mie, G. Beiträge zur Optik trüber Medien, speziell kolloidaler Metallösungen. *Annalen der Physik* **330,** 377–445 (1908).

25. Maier, S. A. *Plasmonics: Fundamentals and applications* ISBN: ISBN 978-0-387-37825-1. doi:10.1007/0-387-37825-1. http://dx.doi.org/10.1007/0-387-37825-1 (Springer, 2007).

26. Jain, P. K., Lee, K. S., El-Sayed, I. H. & El-Sayed, M. A. Calculated Absorption and Scattering Properties of Gold Nanoparticles of Different Size, Shape, and Composition: Applications in Biological Imaging and Biomedicine. *The Journal of Physical Chemistry B* **110.** PMID: 16599493, 7238–7248 (2006).

27. Webb, J. A. *et al.* Geometry-Dependent Plasmonic Tunability and Photothermal Characteristics of Multibranched Gold Nanoantennas. *The Journal of Physical Chemistry C* **118,** 3696–3707 (2014).

28. Nehl, C. L. & Hafner, J. H. Shape-dependent plasmon resonances of gold nanoparticles. *J. Mater. Chem.* **18,** 2415–2419 (21 2008).

29. Miller, M. M. & Lazarides, A. A. Sensitivity of Metal Nanoparticle Surface Plasmon Resonance to the Dielectric Environment. *The Journal of Physical Chemistry B* **109.** PMID: 16853799, 21556–21565 (2005).

30. Haes, A. J., Hall, W. P., Chang, L., Klein, W. L. & Van Duyne, R. P. A Localized Surface Plasmon Resonance Biosensor: First Steps toward an Assay for Alzheimer's Disease. *Nano Letters* **4,** 1029–1034 (2004).

31. Garcia, M. A. Surface plasmons in metallic nanoparticles: fundamentals and applications. *Journal of Physics D: Applied Physics* **44,** 283001 (2011).

32. Kelly, K. L., Coronado, E., Zhao, L. L. & Schatz, G. C. The Optical Properties of Metal Nanoparticles: The Influence of Size, Shape, and Dielectric Environment. *The Journal of Physical Chemistry B* **107,** 668–677 (2003).

33. Chung, T., Lee, S.-Y., Song, E. Y., Chun, H. & Lee, B. Plasmonic Nanostructures for Nano-Scale Bio-Sensing. *Sensors* **11,** 10907–10929. ISSN: 1424-8220 (2011).

34. Chen, A. L. *et al.* Quantifying spectral changes experienced by plasmonic nanoparticles in a cellular environment to inform biomedical nanoparticle design. *Nano- scale Research Letters* **9,** 454. ISSN: 556-276X (2014).

35. Govorov, A. O. & Richardson, H. H. Generating heat with metal nanoparticles. *Nano Today* **2,** 30–38. ISSN: 1748-0132 (2007).

36. Kreibig, U. & Vollmer, M. *Optical properties of metal clusters* (Springer-Verlag, Berlin, Heidelberg, 1995).

37. Lin, C.-C. *et al.* Highly efficient CdS-quantum-dot-sensitized GaAs solar cells. *Opt. Express* **20,** A319–A326 (Mar. 2012).

38. Chen, K.-J. *et al.* Resonant-Enhanced Full-Color Emission of Quantum-Dot-Based Display Technology Using a Pulsed Spray Method. *Advanced Functional Materials* **22,** 5138–5143. ISSN: 1616-3028 (2012).

39. Kim, T.-H. *et al.* Full-colour quantum dot displays fabricated by transfer printing. *Nature Photonics* **5,** 176–182 (Mar. 2011).

40. Saikia, K., Deb, P. & Kalita, E. Sensitive fluorescence response of ZnSe(S) quantum dots: an efficient fluorescence probe. **87,** 065802 (June 2013).

41. Liu, S.-L. *et al.* Effectively and Efficiently Dissecting the Infection of Influenza Virus by Quantum -Dot -Based Single -Particle Tracking. *ACS Nano* **6,** 141–150 (2012).

42. Alivisatos, A. P. Semiconductor Clusters, Nanocrystals, and Quantum Dots. *Science* **271,** 933–937. ISSN: 0036-8075 (1996).

43. Murray, C., kagan, C. & Bawendi, M. Synthesis and characterization of monodisperse nanocrystals and close-packed nanocrystal assemblies. *Annual Review of Materials Science* **30,** 545–610 (2000).

44. Klimov, V. I. *Semiconductor and Metal Nanocrystals: Synthesis and Electronic and Optical Properties* (SCRC Press, 2003).

45. Marcus, R. A. Chemical and Electrochemical Electron-Transfer Theory. *Annual Review of Physical Chemistry* **15,** 155–196 (Oct. 1964).

46. Kuznetsov, A. & Ulstrup, J. *Electron transfer in chemistry and biology: An introduction to the theory* ISBN: 0471967491 (John Wiley Sons Ltd, 1999).

47. Wu, P. & Yan, X.-P. Doped quantum dots for chemo/biosensing and bioimaging. *Chem. Soc. Rev.* **42,** 5489–5521 (12 2013).

48. Gao, X. *et al.* In vivo molecular and cellular imaging with quantum dots. *Current Opinion in Biotechnology* **16.** Analytical biotechnology, 63–72. ISSN: 0958-1669 (2005).

49. Jaiswal, J. K., Mattoussi, H., Mauro, J. M. & Simon, S. M. Long-term multiple color imaging of live cells using quantum dot bioconjugates. *Nature Biotechnology* **21,** 47–51 (2003).

50. Zrazhevskiy, P. & Gao, X. Multifunctional Quantum Dots for Personalized Medicine. *Nano today* **4,** 414–428 (2009).

51. Lidke, D. S. *et al.* Quantum dot ligands provide new insights into erbB/HER receptor–mediated signal transduction. *Nature Biotechnology* **22,** 198–203 (2004).

52. Reinitzer, F. Beiträge zur kenntniss des cholesterins. *Monatsh. Chem.* **9,** 421–441 (1888).

53. Collings, P. J. *Liquid Crystals: nature delicate phase of matter* ISBN: 0691085099 (Princeton University Press, 1991).
54. Ramamoorthy, A. *Thermotropic Liquid Crystals* ISBN: 978-1-4020-5327-6 (Springer, 2007).
55. Friedel, G. Les états mésomorphes de la matière. *Ann. Phys.* **9,** 273–474 (1922).
56. Hirst, L. S. *Fundamentals of Soft Matter Science* ISBN: 9781439827758 (CRC Press, 2012).
57. Buckingham, A. D., Ceasar, G. P. & Dunn, M. B. The addition of optically active compounds to nematic liquid crystals. *Chemical Physics Letters* **3,** 540–541 (Aug. 1969).
58. Kitzerow, H. & Bahr, C. *Chirality in Liquid Crystals* ISBN: 978-0-387-98679-1 (Sprin-ger Verlag New York, 2001).
59. Tsvetkov, V. N. & Mikhailov, G. M. Acta Physicochim. *U.R.S.S.* **8** (1938).
60. Ghosh, S. K. A model for the orientational order in liquid crystals. *Il Nuovo Cimento D* **4,** 229–244 (Sept. 1984).
61. Patrick Oswald, P. P. *Nematic and Cholesteric Liquid Crystals: Concepts and Physical Properties Illustrated by Experiments* ISBN: 9780415321402 (CRC Press, Taylor Francis, 2005).
62. Adler, J. H., Emerson, D. B., Farrell, P. E. & MacLachlan, S. P. A Deflation Technique for Detecting Multiple Liquid Crystal Equilibrium States. *ArXiv e-prints.* ar -Xiv: 1601.07383 (math.NA) (Jan. 2016).
63. Yang, D. K. & Wu, S. T. *Fundamentals of Liquid crystal devices* ISBN: 978-0-470-03202-2 (John Wiley Sons, 2002).
64. DeGennes, P. G. Short Range Order Effects in the Isotropic Phase of Nematics and Cholesterics. *Molecular Crystals and Liquid Crystals* **12,** 193–214 (1971).
65. Freedericksz, V. & Zolina, V. Forces causing the orientation of an anisotropic liquid. *Trans. Faraday Soc.* **29,** 919–930 (140 1933).
66. Chigrinov, V. G. *Liquid Crystal Devices: Physics and Applications* ISBN: 0-89006-898-4 (Artech House Publisher, 1999).
67. Frisken, B. J. & Palffy-Muhoray, P. Electric-field-induced twist and bend Freedericksz transitions in nematic liquid crystals. *Phys. Rev. A* **39,** 1513–1518 (3 Feb. 1989).
68. Born, M. & Wolf, E. *Principles of Optics* ISBN: 0521642221 (Cambridge University Press, 1980).

69. Dierking, I. *Introduction, in Textures of Liquid Crystals* ISBN: 9783527307258 (Wiley -VCH, 2003).

70. Coates, D. Liquid crystal in complex geometries. Edited by G. P. Crawford and S. Zumer. *Advanced Materials* **9,** 996–997. ISSN: 1521-4095 (1997).

71. Muševič, I. Nematic colloids, topology and photonics. *Philosophical Transactions of the Royal Society of London A: Mathematical, Physical and Engineering Sciences* **371** (2013).

72. Lin, I. *et al.* Endotoxin-induced structural transformations in liquid crystalline drop -lets. *Science* **332,** 1297–1300. ISSN: 0036-8075 (June 2011).

73. Trivedi, R. P., Klevets, I. I., Senyuk, B., Lee, T. & Smalyukh, I. I. Reconfigurable interactions and three-dimensional patterning of colloidal particles and defects in lamellar soft media. *Proceedings of the National Academy of Sciences* **109,** 4744–4749 (2012).

74. Somasundaran, P. *Encyclopedia of Surface and Colloid Science* ISBN: 9781466590-458 (CRC Press, 2006).

75. Petty, H. R. Fluorescence microscopy: Established and emerging methods, experimental strategies, and applications in immunology. *Microscopy Research and Technique* **70,** 687–709. ISSN: 1097-0029 (2007).

76. Nwaneshiudu, A. *et al.* Introduction to Confocal Microscopy. *Journal of Investigative Dermatology* **132,** 1–5 (2012).

77. Booth, M. J., Débarre, D. & Jesacher, A. Adaptive Optics for Biomedical Microscopy. *Opt. Photon. News* **23,** 22–29 (Jan. 2012).

78. Paddock, S. W. *Confocal Microscopy: Methods and Protocols* ISBN: 9781466590-458 (Humana Press, 2014).

79. Fabio Cannone Giuseppe Chirico, A. D. Two-photon interactions at single fluorescent molecule level. *Journal of Biomedical Optics* **8,** 8 - 8 - 5 (2003).

80. Song, L., Varma, C. A., Verhoeven, J. W. & Tanke, H. J. Influence of the triplet excited state on the photobleaching kinetics of fluorescein in microscopy. *Biophysical Journal* **70,** 2959–2968 (2017/11/16 1996).

81. Patterson, G. H. & Piston, D. W. Photobleaching in Two Photon Excitation Microscopy. *Biophysical Journal* **78,** 2159–2162. ISSN: 0006-3495 (2000).

82. Molski, A. Statistics of the bleaching number and the bleaching time in single molecule fluorescence spectroscopy. **114,** 1142–1147 (Jan. 2001).

83. Dixit, R. & Cyr, R. Cell damage and reactive oxygen species production induced by fluorescence microscopy: effect on mitosis and guidelines for non-invasive fluorescence microscopy. *The Plant Journal* **36,** 280–290. ISSN: 1365-313X (2003).

84. Samia, A., Chen, X. & Burda, C. Semiconductor Quantum Dots for Photodynamic Therapy. *Journal of the American Chemical Society* **125,** 15736–15737. ISSN: 0002-7863 (Dec. 2003).

85. Olson, J. *et al.* Optical characterization of single plasmonic nanoparticles. *Chem. Soc. Rev.* **44,** 40–57 (1 2015).

86. Decorde, N. *et al.* Small angle X-ray scattering coupled with in situ electromechanical probing of nanoparticle-based resistive strain gauges. *Nanoscale* **6,** 15107–15116 (24 2014).

87. Draine, B. T. & Flatau, P. J. Discrete-Dipole Approximation For Scattering Calculations. *J. Opt. Soc. Am. A* **11,** 1491–1499 (Apr. 1994).

88. Jackson, J. D. *Classical Electrodynamics* ISBN: 978-0-471-30932-1 (Wiley, 1998).

89. Johnson, P. B. & Christy, R. W. *Theory of Electric Polarization* ISBN: 978-0-471-30932-1 (Elsevier, 1973).

90. Johnson, P. B. & Christy, R. W. Optical Constants of the Noble Metals. *Physical Review B* **6,** 4370–24379 (1972).

91. Vial, A., Grimault, A.-S., Macıas, D., Barchiesi, D. & de la Chapelle, M. L. Improved analytical fit of gold dispersion: Application to the modeling of extinction spectra with a finite-difference time-domain method. *Phys. Rev. B* **71,** 085416 (8 Feb. 2005).

92. Buzea, C., Pacheco, I. I. & Robbie, K. Nanomaterials and nanoparticles: Sources and toxicity. *Biointerphases* **2,** MR17–MR71. ISSN: 1559-4106 (Dec. 2007).

93. Ahmad, A. *et al.* Extracellular biosynthesis of silver nanoparticles using the fungus Fusarium oxysporum. *Colloids and Surfaces B: Biointerfaces* **28,** 313–318. ISSN: 0927-7765 (2003).

94. Klaus-Joerger, T., Joerger, R., Olsson, E. & Granqvist, C.-G. Bacteria as workers in the living factory: metal-accumulating bacteria and their potential for materials science. *Trends in Biotechnology* **19,** 15–20 (2001).

95. Shiraishi, Y. *et al.* Frequency modulation response of a liquid-crystal electro-optic device doped with nanoparticles. *Applied Physics Letters* **81,** 2845 (Oct. 2002).

96. Bitar, R., Agez, G. & Mitov, M. Cholesteric liquid crystal self-organization of gold nanoparticles. *Soft Matter* **7,** 8198–8206 (18 2011).

97. Kumar, S., Pal, S. K., Kumar, P. S. & Lakshminarayanan, V. Novel conducting nanocomposites: synthesis of triphenylene-covered gold nanoparticles and their insertion into a columnar matrix. *Soft Matter* **3,** 896–900 (7 2007).

98. Qi, H., Kinkead, B., Marx, V. M., Zhang, H. R. & Hegmann, T. Miscibility and alignment effects of mixed monolayer cyanobiphenyl liquid-crystal-capped gold nanoparticles in nematic cyanobiphenyl liquid crystal hosts. *Chemphyschem : a European journal of chemical physics and physical chemistry* **10 8,** 1211–8 (2009).

99. Demortiére, A. *et al.* Nematic-like Organization of Magnetic Mesogen-Hybridized Nanoparticles. *Small* **6,** 1341–1346. ISSN: 1613-6829 (2010).

100. Verma, Y. K. *et al.* Electrical modulation of static and dynamic spectroscopic properties of coupled nanoscale GaSe quantum dot assemblies. *Phys. Rev. B* **82,** 165428 (16 Oct. 2010).

101. Zeng, X. *et al.* 3D Ordered Gold Strings by Coating Nanoparticles with Mesogens. *Advanced Materials* **21,** 1746–1750. ISSN: 1521-4095 (2009).

102. Rodarte, A. L., Pandolfi, R. J., Ghosh, S. & Hirst, L. S. Quantum dot/liquid crystal composite materials: self-assembly driven by liquid crystal phase transition templating. *J. Mater. Chem. C* **1,** 5527–5532 (35 2013).

103. Qi, H. & Hegmann, T. Formation of periodic stripe patterns in nematic liquid crystals doped with functionalized gold nanoparticles. *J. Mater. Chem.* **16,** 4197–4205 (43 2006).

104. Dickson, W., Wurtz, G., Evans, P., Pollard, R. & Zayats, A. Electronically controlled surface plasmon dispersion and optical transmission through metallic hole arrays using liquid crystal. *Nano Letter* **8,** 281–286 (Jan. 2008).

105. Kossyrev, P. A. *et al.* Electric Field Tuning of Plasmonic Response of Nanodot Array in Liquid Crystal Matrix. *Nano Letters* **5,** 1978–1981 (Oct. 2005).

106. Buchnev, O., Ou, J. Y., Kaczmarek, M., Zheludev, N. I. & Fedotov, V. A. Electro-optical control in a plasmonic metamaterial hybridised with a liquid-crystal cell. *Opt. Express* **21,** 1633–1638 (Jan. 2013).

107. Decker, M. *et al.* Electro-optical switching by liquid-crystal controlled metasurfaces. *Opt. Express* **21,** 8879–8885 (Apr. 2013).

108. Maier, S. A. *Plasmonics: Fundamentals and Applications* ISBN: 978-0-387-33150-8 (Springer, 2007).

109. Nie, S. & Emory, S. R. Probing Single Molecules and Single Nanoparticles by Surface-Enhanced Raman Scattering. *Science* **275,** 1102–1106. ISSN: 0036-8075 (1997).

110. Pompa, P. P. *et al.* Metal-enhanced fluorescence of colloidal nanocrystals with nanoscale control. *Nature Nanotechnology* **1,** 126 EP - (Nov. 2006).

111. Chang, W. & Link, S. Enhancing the Sensitivity of Single-Particle Photothermal Imaging with Thermotropic Liquid Crystals. *The Journal of Physical Chemistry Letters.* **3,** 1393–1399 (May 2012).

112. Škarabot, M., Lokar, Z. & Muševič, I. Transport of particles by a thermally induced gradient of the order parameter in nematic liquid crystals. *Phys. Rev. E* **87,** 062501 (6 June 2013).

113. Giese, M. *et al.* Thermal switching of the reflection in chiral nematic mesoporous organosilica films infiltrated with liquid crystals. *ACS Applied Materials & Interfaces* **5,** 6854–6859 (July 2013).

114. Gilardi, G., Xiao, S., Mortensen, N. A., d'Alessandro, A. & Beccherelli, R. Plasmon resonance optical tuning based on photosensitive composite structures. *J. Opt. Soc. Am. B* **31,** 360–365 (Feb. 2014).

115. Liu, Q., Yuan, Y. & Smalyukh, I. I. Electrically and Optically Tunable Plasmonic Guest–Host Liquid Crystals with Long-Range Ordered Nanoparticles. *Nano Letters* **14.** PMID: 24884975, 4071–4077 (2014).

116. Bigioni, T. P. *et al.* Kinetically driven self assembly of highly ordered nanoparticle monolayers. *Nature Materials* **5,** 265 EP - (Mar. 2006).

117. Sobh, AbderRahman N., White, Sarah., Smith, Jeremy., Sobh, Nahil., and Jain, Prashant K. *nanoDDSCAT* `https://nanohub.org/resources/21414`. 2014.

118. Oh-e, M. & Kondo, K. Response mechanism of nematic liquid crystals using the in-plane switching mode. *Applied Physics Letters* **69,** 623–625 (July 1996).

119. Ikeda, T. & Tsutsumi, O. Optical Switching and Image Storage by Means of Azobenzene Liquid-Crystal Films. *Science* **268,** 1873–1875. ISSN: 0036-8075 (1995).

120. Xu, D., Rao, L., Tu, C.-D. & Wu, S.-T. Nematic Liquid Crystal Display With Submillisecond Grayscale Response Time. *J. Display Technol.* **9,** 67–70 (Feb. 2013).

121. Baffou, G., Quidant, R. & García de Abajo, F. J. Nanoscale Control of Optical Heating in Complex Plasmonic Systems. *ACS Nano* **4.** PMID: 20055439, 709–716 (2010).

122. Banhart, J. Manufacture, characterisation and application of cellular metals and metal foams. *Progress in Materials Science* **46,** 559–632. ISSN: 0079-6425 (2001).

123. Parthasarathy, J., Starly, B. & Raman, S. A design for the additive manufacture of functionally graded porous structures with tailored mechanical properties for biomedical applications. *Journal of Manufacturing Processes* **13,** 160–170. ISSN: 1526-6125 (2011).

124. Striemer, C. C., Gaborski, T. R., McGrath, J. L. & Fauchet, P. M. Charge- and size-based separation of macromolecules using ultrathin silicon membranes. *Nature* **445,** 749 EP - (Feb. 2007).

125. Seo, J. *et al.* Hierarchical and Multifunctional Three-Dimensional Network of Carbon Nanotubes for Microfluidic Applications. *Advanced Materials* **24,** 1975–1979. ISSN: 1521-4095 (2012).

126. Zhang, H., Yu, X. & Braun, P. V. Three-dimensional bicontinuous ultrafast-charge and -discharge bulk battery electrodes. *Nature Nanotechnology* **6,** 277 EP - (Mar. 2011).

127. Grzelczak, M., Vermant, J., Furst, E. M. & Liz-Marzán, L. M. Directed Self-Assembly of Nanoparticles. *ACS Nano* **4.** PMID: 20568710, 3591–3605 (2010).

128. B*ö*ker, A., He, J., Emrick, T. & Russell, T. P. Self-assembly of nanoparticles at interfaces. *Soft Matter* **3,** 1231–1248 (10 2007).

129. Lin, A. L., Wu, T., Chen, W. & Wee, A. T. S. Room temperature positive magnetoresistance via charge trapping in polyaniline-iron oxide nanoparticle composites. *Applied Physics Letters* **103,** 032408 (July 2013).

130. Balazs, A. C., Emrick, T. & Russell, T. P. Nanoparticle Polymer Composites: Where Two Small Worlds Meet. *Science* **314,** 1107–1110. ISSN: 0036-8075 (2006).

131. Yu, C., Fan, J., Tian, B. & Zhao, D. Morphology Development of Mesoporous Materials: a Colloidal Phase Separation Mechanism. *Chemistry of Materials* **16,** 889–898 (2004).

132. Rodarte, A. L. *et al.* Tuning Quantum Dot Organization in Liquid Crystals for Robust Photonic Applications. *ChemPhysChem* **15,** 1413–1421. ISSN: 1439-7641 (2014).

133. Yan, Y., Warren, S. C., Fuller, P. & Grzybowski, B. A. Chemoelectronic circuits based on metal nanoparticles. *Nature Nanotechnology* **11,** 603 EP - (Mar. 2016).

134. Polyak, B. *et al.* Magnetic Nanoparticle-Mediated Targeting of Cell Therapy Reduces In-Stent Stenosis in Injured Arteries. *ACS Nano* **10.** PMID: 27622988, 9559–9569 (2016).

135. Tay, A. & Di Carlo, D. Magnetic Nanoparticle-Based Mechanical Stimulation for Restoration of Mechano-Sensitive Ion Channel Equilibrium in Neural Networks. *Nano Letters* **17.** PMID: 28094958, 886–892 (2017).

136. Schein, P., O'Dell, D. & Erickson, D. Orthogonal Nanoparticle Size, Polydispersity, and Stability Characterization with Near-Field Optical Trapping and Light Scattering. *ACS Photonics* **4,** 106–113 (2017).

137. Uchida, T., Yoshikawa, T., Tamura, M., Iida, T. & Imura, K. Multiple Resonances Induced by Plasmonic Coupling between Gold Nanoparticle Trimers and Hexagonal Assembly of Gold-Coated Polystyrene Microspheres. *The Journal of Physical Chemistry Letters* **7.** PMID: 27596630, 3652–3658 (2016).

138. Hutter, E. & Fendler, J. H. Exploitation of Localized Surface Plasmon Resonance. *Advanced Materials* **16,** 1685–1706. ISSN: 1521-4095 (2004).

139. Liu, S. & Tang, Z. Nanoparticle assemblies for biological and chemical sensing. *J. Mater. Chem.* **20,** 24–35 (1 2010).

140. Daniel, M.-C. & Astruc, D. Gold Nanoparticles: Assembly, Supramolecular Chemistry, Quantum-Size-Related Properties, and Applications toward Biology, Catalysis, and Nanotechnology. *Chemical Reviews* **104.** PMID: 14719978, 293–346 (2004).

141. Bantz, K. C. *et al.* Recent progress in SERS biosensing. *Phys. Chem. Chem. Phys.* **13,** 11551–11567 (24 2011).

142. Qian, X. *et al.* In vivo tumor targeting and spectroscopic detection with surface-enhanced Raman nanoparticle tags. *Nature Biotechnology* **26,** 83 EP - (Dec. 2007).

143. Álvarez-Puebla, R. A. & Liz-Marzán, L. M. SERS-based diagnosis and biodetection. *Small* **6 5,** 604–10 (2010).

144. De, M., Ghosh, P. S. & Rotello, V. M. Applications of Nanoparticles in Biology. *Advanced Materials* **20,** 4225–4241. ISSN: 1521-4095 (2008).

145. Dey, P. *et al.* SERS-based detection of barcoded gold nanoparticle assemblies from within animal tissue. *Journal of Raman Spectroscopy* **44.** JRS-13-0179.R1, 1659–1665. ISSN: 1097-4555 (2013).

146. Atwater, H. A. & Polman, A. Plasmonics for improved photovoltaic devices. *Nature Materials* **9,** 205 EP - (Feb. 2010).

147. Mubeen, S. *et al.* On the Plasmonic Photovoltaic. *ACS Nano* **8.** PMID: 24861280, 6066–6073 (2014).

148. Cushing, S. K. & Wu, N. Progress and Perspectives of Plasmon-Enhanced Solar Energy Conversion. *The Journal of Physical Chemistry Letters* **7.** PMID: 26817500, 666–675 (2016).

149. Xu, J. *et al.* Mechanical Nanosprings: Induced Coiling and Uncoiling of Ultrathin Au Nanowires. *Journal of the American Chemical Society* **132.** PMID: 20698533, 11920–11922 (2010).

150. An, C., Peng, S. & Sun, Y. Facile Synthesis of Sunlight-Driven AgCl:Ag Plasmonic Nanophotocatalyst. *Advanced Materials* **22,** 2570–2574. ISSN: 1521-4095 (2010).

151. Zorić, I., Zäch, M., Kasemo, B. & Langhammer, C. Gold, Platinum, and Aluminum Nanodisk Plasmons: Material Independence, Subradiance, and Damping Mechanisms. *ACS Nano* **5.** PMID: 21438568, 2535–2546 (2011).

152. Zhou, L. *et al.* Aluminum Nanocrystals as a Plasmonic Photocatalyst for Hydrogen Dissociation. *Nano Letters* **16.** PMID: 26799677, 1478–1484 (2016).

153. Zhang, N. *et al.* Near-field dielectric scattering promotes optical absorption by platinum nanoparticles. *Nature Photonics* **10,** 473 EP - (May 2016).

154. Xing, H. *et al.* DNA-Directed Assembly of Asymmetric Nanoclusters Using Janus Nanoparticles. *ACS Nano* **6.** PMID: 22148462, 802–809 (2012).

155. Jia, H., Bai, X., Li, N., Yu, L. & Zheng, L. Siloxane surfactant induced self-assembly of gold nanoparticles and their application to SERS. *CrystEngComm* **13,** 6179–6184 (20 2011).

156. Srivastava, S., Frankamp, B. L. & Rotello, V. M. Controlled Plasmon Resonance of Gold Nanoparticles Self-Assembled with PAMAM Dendrimers. *Chemistry of Materials* **17,** 487–490 (2005).

157. Yoon, J. H., Lim, J. & Yoon, S. Controlled Assembly and Plasmonic Properties of Asymmetric Core–Satellite Nanoassemblies. *ACS Nano* **6.** PMID: 22827455, 7199–7208 (2012).

158. Gandra, N., Abbas, A., Tian, L. & Singamaneni, S. Plasmonic Planet–Satellite Analogues: Hierarchical Self-Assembly of Gold Nanostructures. *Nano Letters* **12.** PMID :22533719, 2645–2651 (2012).

159. Taylor, R. W. *et al.* Precise Subnanometer Plasmonic Junctions for SERS within Gold Nanoparticle Assemblies Using Cucurbit[n]uril "Glue". *ACS Nano* **5.** PMID: 21488693, 3878–3887 (2011).

160. Blakey, I., Merican, Z. & Thurecht, K. J. A Method for Controlling the Aggregation of Gold Nanoparticles: Tuning of Optical and Spectroscopic Properties. *Langmuir* **29.** PMID: 23751158, 8266–8274 (2013).

161. Dey, P., Zhu, S., Thurecht, K. J., Fredericks, P. M. & Blakey, I. Self assembly of plasmonic core-satellite nano-assemblies mediated by hyperbranched polymer linkers. *J. Mater. Chem. B* **2,** 2827–2837 (19 2014).

162. Jeon, J.-W. *et al.* Electrically Controlled Plasmonic Behavior of Gold Nanocube @ Polyaniline Nanostructures: Transparent Plasmonic Aggregates. *Chemistry of Materials* **28,** 2868–2881 (2016).

163. Croissant, J. & Zink, J. I. Nanovalve-Controlled Cargo Release Activated by Plasmonic Heating. *Journal of the American Chemical Society* **134.** PMID: 22540671, 7628–7631 (2012).

164. Niikura, K., Iyo, N., Matsuo, Y., Mitomo, H. & Ijiro, K. Sub-100 nm Gold Nanoparticle Vesicles as a Drug Delivery Carrier enabling Rapid Drug Release upon Light Irradiation. *ACS Applied Materials & Interfaces* **5.** PMID: 23566248, 3900–3907 (2013).

165. Huang, H.-L. *et al.* Fiber-optic triggered release of liposome in vivo: implication of personalized chemotherapy. *International Journal of Nanomedicine* **10,** 5171–5185 (2015).

166. Leung, S. & Romanowski, M. Light-activated content release from liposomes. *Theranostics* **2,** 1020–1036. ISSN: 1838-7640 (2012).

167. Huschka, R., Neumann, O., Barhoumi, A. & Halas, N. J. Visualizing Light-Triggered Release of Molecules Inside Living Cells. *Nano Letters* **10.** PMID: 20857946, 4117–4122 (2010).

168. Yan, B., Boyer, J.-C., Habault, D., Branda, N. R. & Zhao, Y. Near Infrared Light Triggered Release of Biomacromolecules from Hydrogels Loaded with Upconversion Nanoparticles. *Journal of the American Chemical Society* **134.** PMID: 23013429, 16558–16561 (2012).

169. Rapoport, N. Y., Kennedy, A. M., Shea, J. E., Scaife, C. L. & Nam, K.-H. Controlled and targeted tumor chemotherapy by ultrasound-activated nanoemulsions/microbubbles. *Journal of Controlled Release* **138.** Sixth International Nanomedicine and Drug Delivery Symposium, 268–276. ISSN: 0168-3659 (2009).

170. Merino, S., Martín, C., Kostarelos, K., Prato, M. & Vázquez, E. Nanocomposite Hydrogels: 3D Polymer–Nanoparticle Synergies for On-Demand Drug Delivery. *ACS Nano* **9.** PMID: 25938172, 4686–4697 (2015).

171. Edelstein, A., Amodaj, N., Hoover, K., Vale, R. & Stuurman, N. in *Current Protocols in Molecular Biology* (John Wiley Sons, Inc., 2001). ISBN: 9780471142720. doi:10.1002/0471142727.mb1420s92. http://dx.doi.org/10.1002/0471142727.mb1420s92.

172. Nych, A. *et al.* Assembly and control of 3D nematic dipolar colloidal crystals. *Nature Communications* **4,** 1489 EP - (Feb. 2013).

173. Van Sark, W. G. *et al.* Luminescent Solar Concentrators - A review of recent results. *Opt. Express* **16,** 21773–21792 (Dec. 2008).

174. Baffou, G., Polleux, J., Rigneault, H. & Monneret, S. Super-Heating and Micro-Bubble Generation around Plasmonic Nanoparticles under cw Illumination. *The Journal of Physical Chemistry C* **118,** 4890–4898 (2014).

175. Hashimoto, S., Werner, D. & Uwada, T. Studies on the interaction of pulsed lasers with plasmonic gold nanoparticles toward light manipulation, heat management, and nanofabrication. *Journal of Photochemistry and Photobiology C: Photochemistry Reviews* **13,** 28–54. ISSN: 1389-5567 (2012).

176. Heber, A., Selmke, M. & Cichos, F. Metal Nanoparticle Based All-Optical Photothermal Light Modulator. *ACS Nano* **8.** PMID: 24437364, 1893–1898 (2014).

177. Fang, Z. *et al.* Evolution of Light-Induced Vapor Generation at a Liquid-Immersed Metallic Nanoparticle. *Nano Letters* **13.** PMID: 23517407, 1736–1742 (2013).

178. Neumann, O. *et al.* Solar Vapor Generation Enabled by Nanoparticles. *ACS Nano* **7.** PMID: 23157159, 42–49 (2013).

179. Katayama, T., Setoura, K., Werner, D., Miyasaka, H. & Hashimoto, S. Picosecond-to-Nanosecond Dynamics of Plasmonic Nanobubbles from Pump–Probe Spectral Measurements of Aqueous Colloidal Gold Nanoparticles. *Langmuir* **30.** PMID: 25083945, 9504–9513 (2014).

180. Vansant, J. H. Conduction heat transfer solutions. *NASA STI/Recon Technical Report N* **81** (Mar. 1980).

181. Weiss, S. & Ahlers, G. Nematic–isotropic phase transition in turbulent thermal convection. *Journal of Fluid Mechanics* **737,** 308–328 (2013).

182. Sobh, AbderRahman N., White, Sarah., Smith, Jeremy., Sobh, Nahil., and Jain, Prashant K. *nanoDDSCAT+* `https://nanohub.org/resources/21414`. 2014.

183. Guisbert, E., Yura, T., Rhodius, V. A. & Gross, C. A. Convergence of Molecular, Modeling, and Systems Approaches for an Understanding of the Escherichia coli Heat Shock Response. *Microbiology and Molecular Biology Reviews : MMBR* **72,** 545–554 (Sept. 2008).

184. Alkilany, A. M. & Murphy, C. J. Toxicity and cellular uptake of gold nanoparticles: what we have learned so far? *Journal of Nanoparticle Research* **12,** 2313–2333 (Sept. 2010).

185. Mura, S., Nicolas, J. & Couvreur, P. Stimuli-responsive nanocarriers for drug delivery. *Nature Materials* **12,** 991 EP - (Oct. 2013).

186. Jiang, X. *et al.* Controllably tuning the near-infrared plasmonic modes of gold nanoplates for enhanced optical coherence imaging and photothermal therapy. *RSC Adv.* **5,** 80709–80718 (98 2015).

187. Adams, S. & Zhang, J. Z. Unique optical properties and applications of hollow gold nanospheres (HGNs). *Coordination Chemistry Reviews* **320-321.** SI: Functional Nanomaterials 2016, 18–37. ISSN: 0010-8545 (2016).

188. Al-Ahmady, Z. S. *et al.* Lipid–Peptide Vesicle Nanoscale Hybrids for Triggered Drug Release by Mild Hyperthermia in Vitro and in Vivo. *ACS Nano* **6.** PMID: 22857653, 9335–9346 (2012).

189. Katsuma, M. *et al.* Studies on lactulose formulations for colon-specific drug delivery. *International Journal of Pharmaceutics* **249,** 33–43. ISSN: 0378-5173 (2002).

190. Cleland, J. L., Johnson, O. L., Putney, S. & Jones, A. J. Recombinant human growth hormone poly(lactic-co-glycolic acid) microsphere formulation development. **28.** Bi- odegradable Microspheres/Therapeutic Peptide Delivery, 71–84. ISSN: 0169-409X (1997).

191. Lambert, J. M., Weinbreck, F. & Kleerebezem, M. In Vitro Analysis of Protection of the Enzyme Bile Salt Hydrolase against Enteric Conditions by Whey ProteinGum Arabic Microencapsulation. *Journal of Agricultural and Food Chemistry* **56.** PMID: 18729459, 8360–8364 (2008).

192. Orive, G. *et al.* Cell encapsulation: Promise and progress. *Nature Medicine* **9,** 104 EP - (Jan. 2003).

193. Boag, A. H. & Sefton, M. V. Microencapsulation of human fibroblasts in a water-insoluble polyacrylate. *Biotechnology and Bioengineering* **30,** 954–962. ISSN: 1097-0290 (1987).

194. McGuigan, A. P., Bruzewicz, D. A., Glavan, A., Butte, M. J. & Whitesides, G. M. Correction: Cell Encapsulation in Sub-mm Sized Gel Modules Using Replica Molding. *PLOS ONE* **3.** doi:10.1371/annotation/0a0b70a9-a6e0-4e60-b6bd-8ef894ed22cd. https://doi.org/10.1371/annotation/0a0b70a9-a6e0-4e60-b6bd-8ef894ed22cd (July 2008).

195. Hasse, C., Klöck, G., Schlosser, A., Zimmermann, U. & Rothmund, M. Parathyroid allotransplantation without immunosuppression. *The Lancet* **350,** 1296–1297 (1997).

196. Shao, J., Xiang, J., Axner, O. & Ying, C. Wavelength-modulated tunable diode-laser absorption spectrometry for real-time monitoring of microbial growth. *Appl. Opt.* **55,** 2339–2345 (Mar. 2016).

197. Laing, J. M. *et al.* Intranasal Administration of the Growth-Compromised HSV-2 Vector ΔRR Prevents Kainate-Induced Seizures and Neuronal Loss in Rats and Mice. *Molecular Therapy* **13,** 870–881 (2006).

198. Bratosin, D., Mitrofan, L., Palii, C., Estaquier, J. & Montreuil, J. Novel fluorescence assay using calcein-AM for the determination of human erythrocyte viability and aging. *Cytometry Part A* **66A,** 78–84. ISSN: 1552-4930 (2005).

199. Chintharlapalli, S. *et al.* 2-Cyano-3,12-dioxoolean-1,9-dien-28-oic Acid and Related Compounds Inhibit Growth of Colon Cancer Cells through Peroxisome Proliferator-Activated Receptor -Dependent and -Independent Pathways. *Molecular Pharmacology* **68,** 119–128. ISSN: 0026-895X (2005).